School of Science
Department of Physics & Astronomy

Ionospheric modeling for low frequency radioastronomy

Balwinder Singh Amrit Singh Arora

This thesis is presented for the Degree of
Doctor of Philosophy
of
Curtin University

March 2016

Declaration:

To the best of my knowledge and belief this thesis contains no material previously published by any other person except where due acknowledgement has been made.

This thesis contains no material which has been accepted for the award of any other degree or diploma in any university.

Balwinder Singh Arora
31st August, 2017

Dedicated to my parents

Acknowledgements

During my years of study, for my degree of Masters, in University of Pune, India, we were mentored to dedicate our future towards higher research and development. It is the envision that was imparted on us that brings me to submit my research work today in the form of a thesis. My research career started with utilising the data from the Global Positioning System, for applications in meteorology, geodesy, and the current endeavour, astronomy. Like every child, I was always fascinated by astronomy, and would always find an opportunity to learn more about this discipline. To work towards a degree of Doctor of Philosophy, as exciting and inspiring as this, was to realise a dream. Here, I extend my sincere gratitude to the people who have made my dream come true, and have played an important part during this journey.

I thank my supervisors, Steven Tingay, Stephen Ord and John Morgan, for their guidance and technical discussions. Being an amateur in radio astronomy, with limited prior knowledge of the field, I thank you for your kind patience and support that you bestowed upon me throughout my thesis and mentored me in this discipline. I especially thank Steven Tingay for believing in me and providing with me an opportunity for my Ph.D., and for securing the ICRAR postgraduate scholarship. I will be always thankful for the guidance and support that I recieved from Steven Tingay throughout my studies, it motivated me to work harder during many a testing times. I thank Stephen Ord for his immense support through out this thesis, both academic and non-academic, you came across to me as approachable and an understanding person, a chat with you always helped me troubleshoot the problems that came my way. With John Morgan, I had a chance to collaborate closely during the later stage (however

the most crucial stage) of my Ph.D., it has helped me shape my research, and I derive great motivation and cherish the discussions we have had.

I have enjoyed and learnt at the same time, from the discussions, with opportunities that came by for collaboration with other researchers. I really appreciate the technical discussions I have had with Anthony (Tony) Willis, National Research Council of Canada, Emil Lenc, Sydney Institute for Astronomy and Gianni Bernardi, Square Kilometre Array South Africa. With our personal meetings at conferences, I had the opportunity to talk on various topics with Tony Willis and Emil Lenc, which have a lasting impression on me. My discussions with Shyeh Tjing (Cleo) Loi, University of Cambridge on ionospheric studies were greatly beneficial, I really enjoyed participating, as well as reading, the contributions that you have made towards ionospheric studies with the MWA.

During my research with the GPS and GLONASS, I made use of Geoscience Australia (GA) network data. My discussions with Ryan Ruddick, GNSS Network Manager, GA were very fruitful, and helped me sort out the issues with GA data for newly installed station MRO1 (Murchison).

The Space Weather Services (SWS), earlier known as Ionospheric Prediction Service (IPS), have number of ionospheric products ad services which were timely used during my research. I thank Michael Terkildsen, Matthew Francis, Kehe Wang and other IPS/SWS personnel for their prompt help in resolving the issues regarding ionospheric data access.

The administrative and technical staff in CIRA have been of immense help at numerous occasions during these years of my Ph.D. I would like to thank Tina Salisbury, Angela Dunleavy, Roselina Stone, Evelyn Clune, David Emrich, David Kenney, Jonathan Tickner, Luke Horsley, and the many temporary members of the administrative staff for their kind help and support.

To my parents, my mom an dad, who gave me the freedom to choose the subjects which interest me, right from an early age, and believed in me that I was going to make it right. My mom, Avinash Kaur, who believed in me and supported me unconditionally, and dad, Amrit Singh, who imbibed in me the critical thinking skills, which contributed to where I stand today. Hope with this effort of mine I have made you both proud.

The person in my life, who has lived my Ph.D. experience, more closely than any one else, my wife Lavanya Arora. I thank you for your support through out

this thesis, it was during the toughest of times that you helped me sail through it. Our little bundle of joy, Ayushman, some of the memorable moments of my Ph.D. life are the times when I reach home in the evening and see him. Even the most strenuous of the days ended with the most beautiful evenings with my family.

I thank and acknowledge the International Centre for Radio Astronomy Research for providing me with financial support through their postgraduate research scholarship. During my research for this thesis, I have made use of the data from the MWA, the MWA observations conducted during the GaLactic and Extragalactic All-sky MWA survey were used to derive the ionospheric effects. The GPS and GLONASS data, available through the Geoscience Australia's public archive, for stations close to the MRO, were used in this thesis to generate the ionospheric model.

I take this opportunity to thank people who conducted the MWA observations on my behalf, for the GaLactic and Extragalactic All-sky MWA survey. This thesis benefited from the services of the iVEC, a jointly operated venture between CSIRO, and various Western Australian universities, including Curtin University.

Abstract

In this thesis, we study the ionosphere effects on the Murchison Widefield Array (MWA), the refraction, which causes displacement in the source positions from its true celestial coordinates. The refraction due to the ionosphere causes a delay in the phase of the interferometer, a 1 rad change in the phase would see a ∼0.02 TECU change in the ionosphere at MWA frequencies. Hence while ionosphere corrections are generated for low frequency interferometers, they should be ∼0.02 TECU or better.

The Global Positioning System (GPS) transmits signals on atleast two frequencies and has been used to study and model the ionosphere. The GPS observables, namely the phase observable, has a precision of ∼0.01 TECU (at MWA frequencies) and is used in this study along with the GLONASS (Russian global positioning system) to model the ionosphere.

Ionosphere and other biases, namely the Differential Code Biases (DCB), are modelled by global GPS data processing centers, namely Center for Orbit determination in Europe (CODE). However the spatial and temporal resolution of the ionosphere is coarse and not suited to our study. Also the DCBs are only available for the GPS receivers that are used to generate the global ionosphere model.

In our study, we make use of the GPS and GLONASS data from Geoscience Australia (GA) permanent network near Murchsion Radio-astronomy Observatory (MRO), to model the ionosphere by a single layer ionosphere model assumption, while the ionosphere is assumed to be concentrated in a single layer. The ionosphere as well as other unknowns, the DCBs, in the GPS and GLONASS

observation model are estimated using a Kalman Filter approach for the selected GA stations. The GPS and GLONASS data integrity algorithms are developed, which detect and repair the uncertainties in the observation data, such as the cycle-slips.

Even though, the ionospheric effects are derived from the MWA, 128 tile configuration and compared with the GNSS, the future upgrades to the MWA (256 tile configuration) and the developments with the upcoming low frequency interferometer arrays like the SKA would need an external source of ionospheric corrections for calibration. We make use of the ionospheric information derived from the MWA, 128 tile as a reference value and improve upon our methodology to estimate the ionospheric effects from GPS and GLONASS observations.

The ionosphere effects derived from the GPS and GLONASS (together refereed to as Global Navigation Satellite System or GNSS), and the MWA are decomposed into the East-West and North-South components for comparisons. The ionospheric modelling using GPS and GLONASS is performed using a single layer approximation, using a second order Taylor series polynomial expansion, utilising the data from publicly available GA permanent network in the vicinity of MRO. Initial results using single-station approach, fixed ionospheric height, show good agreements in the ionospheric trends between the GPS and the MWA. The ionospheric modelling is improved using multi-station approach, a combined GPS and GLONASS observation model, with the variable height of the ionosphere. The ionospheric trends from the GPS and GLONASS replicate very well with the MWA trends. However, the current installations of GNSS network around MRO are too sparse to capture the same variation in the ionosphere as seen by the MWA.

The precision of the ionospheric corrections required for low frequency interferometers can be met with the GNSS. The current available GNSS, namely the GPS and GLONASS, though are limited by the sparse infrastructure, have proved generate ionospheric corrections having high correlation wit the MWA derived ionospheric trends. The future GNSS, namely the Galileo (European Union) and BeiDou (China) are expected to be operational around 2025. In view of having an alternate source of ionospheric corrections, from GNSS, for calibration of the future low frequency arrays, improving the density of the current GNSS infrastructure around MRO is needed.

Abbreviations, acronyms and symbols

A. List of abbreviations and acronyms

Acronym	*Definition*	*Page no*
GPS	Global Positioning System	p.1
GLONASS	Russian global positioning system	p.1
WSRT	Westerbork Synthesis Radio Telescope	p.2
VLBI	Very Long Baseline Interferometry	p.2
VTEC	Vertical Total Electron Content	p.2
CODE	Center for Orbit Determination in Europe	p.2
TECU	Total Electron Content Unit	p.3
HI	neutral hydrogen	p.3
GMRT	Giant Metrewave Radio Telescope	p.3
LOFAR	Low-Frequency Array	p.3
PAPER	Precision Array for Probing the Epoch of Reionization	p.3
LWA	Long Wavelength Array	p.4
MWA	Murchison Widefield Array	p.4
SKA	Square Kilometer Array	p.4
SKA-low	Low frequency component of the Square Kilometer Array	p.4
SWS	Space Weather Service	p.5
EM	Electromagnetic (waves, radiation)	p.6
TID	Travelling Ionospheric Disturbances	p.7
SCTID	Small Scale Travelling Ionospheric Disturbances	p.7

Acronym	*Definition*	*Page no*
MSTID	Medium Scale Travelling Ionospheric Disturbances	p.7
LSTID	Large Scale Travelling Ionospheric Disturbances	p.7
VLA	Very Large Array	p.7
EIA	Equatorial Ionisation anomaly	p.8
MRO	Murchison Radioastronomy Observatory	p.8
FoV	Field-of-View	p.10
TEC	Total Electron Content	p.14
AIUB	Astronomical Institute at the University of Bern	p.15
JPL	Jet Propulsion Laboratory	p.15
MIT	Massachusetts Institute of Technology	p.15
ROB	Royal Observatory of Belgium	p.17
Galileo	European Union's global positioning system	p.17
BeiDou	China's global positioning system	p.17
GNSS	Global Navigation Satellite Systems	p.17
GA	Geoscience Australia	p.17
GLEAM	the GaLactic and Extragalactic All-sky MWA survey	p.17
EoR	Epoch of Reionisation	p.19
HF	High Frequency (communiactions)	p.24
RHCP	Right Hand Circularly Polarised	p.26
LHCP	Left Hand Circularly Polarised	p.26
STEC	Slant Total Electron Content	p.26
FWHM	Full width at half maximum	p.30
FDMA	Frequency Division Multiple Access	p.35
PRN	Pseudo Random Noise	p.36
DCB	Differential Code Bias	p.38
GF	Geometry-Free (GNSS observable model)	p.38
UTC	Coordinated Universal Time	p.38
UT1	Universal Time	p.38
IGS	International GNSS Service	p.38
RINEX	Receiver INdependent EXchange (format)	p.39
MRO1	Murchison GNSS station	p.41
MTMA	Mount Magnet GNSS station	p.41

Acronym	*Definition*	*Page no*
YAR3	Yarragadee GNSS station	p.41
WILU	Wiluna GNSS station	p.41
BERNESE	University of Bern's GNSS software	p.44
IPP	Ionosphere Pierce Point	p.46
LT	Local solar time	p.47
DOY	Day of Year	p.50
NGDC	National Geophysical Data Center	p.53
NOAA	National Oceanic and Atmospheric Administration	p.53
SPWC	Space Weather Prediction Center	p.53
IONEX	IONosphere Map EXchange Format	p.55
MSLM	Modified Single Layer Model	p.55
ESM	Extended Slab Model	p.55
RMS	Root Mean Square error	p.56
EW	East-West (direction-vector component, gradient-polynomial component)	p.60
NS	North-South (direction-vector component, gradient-polynomial component)	p.60
PPP	Precise Point Positioning	p.68
EOP	Earth Orientation Parameters	p.68
IONOLAB-BIAS	IONOsphere research LABoratories single-station receiver BIAS estimation algorithm	p.69
IRI-PLAS	Extension of IRI model to plasma-sphere	p.83

B. List of Symbols

Symbol	*Definition*	*Units*
f_j	GPS frequencies, $j = 1, 2, 5$	Hz
Lj	GPS carrier on frequency f_j, $j = 1, 2, 5$	
f_{j0}	GLONASS centre frequencies, $j = 1, 2$	Hz
f_0	Observing frequency	Hz
e	Electron charge	$1.602 \times 10^{-19}\,\mathrm{A\,s}$
m_e	Mass of the electron	$9.107 \times 10^{-31}\,\mathrm{kg}$
ω_p	Angular frequency of the electron	$\mathrm{rad\,s^{-1}}$
f_p	Plasma frequency	$\mathrm{s^{-1}}$

Symbol	*Definition*	*Units*
N_e	Electron density	$\mathrm{electron/m^3}$
ε_0	Dielectric constant	$8.854 \times 10^{-12}\,\mathrm{s^4\,A^2\,m^{-3}\,kg^{-1}}$
A_p	Plasma frequency constant	$80.6\,\mathrm{m^3\,s^{-2}}$
f	Frequency of the EM wave	$\mathrm{s^{-1}}$
f_c	Critical frequency	$\mathrm{s^{-1}}$
f_g	Gyro frequency	$\mathrm{s^{-1}}$
ω_g	Angular gyro frequency	$\mathrm{rad\,s^{-1}}$
$\mathbf{B}$	Magnetic Field	nT
$n_{\pm}^2$	Ionospheric phase refractive index	
θ_m	Angle between EM wave and magnetic field	rad
X	Normalised plasma frequency	
Y	Modulus of normalised gyro frequency	
n_g	Ionospheric group refractive index	
I_1	First order phase refractive index	
I_2	Second order phase refractive index	
$I_{g,1}$	First order group refractive index	
$I_{g,2}$	Second order group refractive index	
r	Receiver	
s	Satellite	
l	Path length	m
ρ_{ion}	Measured ionospheric range	m
$\rho_{ion,0}$	True ionospheric range	m
ΔI	Phase delay due to the ionosphere	m
ΔI_g	Group delay due to the ionosphere	m
ΔI_1	First order phase delay	m
ΔI_2	Second order phase delay	m
$\Delta I_{g,1}$	First order group delay	m
$\Delta I_{g,2}$	Second order group delay	m
d	diameter of the telescope dish or maximum element separation for a tile	m
$\overrightarrow{D}$	Interferometer antenna element separation (baseline vector)	m

Symbol	*Definition*	*Units*
df	Degrees of freedom of a mathematical model	
I_p	Isoplanatic patch size	
ϕ	Phase of the interferometer	rad
ω	angular frequency	$\mathrm{rad\,s^{-1}}$
τ_{geo}	Geometrical delay	s
λ_0	Observing wavelength	m
λ_F	(Fresnel's) Scale size of irregularities	m
r_F	Fresnel's radius	m
r	Altitude of the ionosphere above Earth's surface	m
D	Component of the baseline	m
θ	Arrival angle for the source	rad
$d\phi$	Change in the phase	rad
$d\theta$	Change in the arrival angle	rad
$E(\cdot)$	Expectation operator	
$D(\cdot)$	Dispersion operator	
$\Phi^s_{r,j}$	Phase observables	m
$P^s_{r,j}$	Code observables	m
$\overline{\rho}^s_r$	'Geometry' parameters, $\rho^s_r + \tau^s_r + c{\cdot}dt^s_r$	m
ρ^s_r	Receiver-Satellite range	m
τ^s_r	Tropospheric path length	m
$c \cdot dt^s_r$	Receiver and satellite clock errors	m
$\iota^s_{r,j}$	Receiver-Satellite ionospheric delay	m
$\mu_j = 1/f_j^2$	Inverse of frequency square	
$M^s_{r,j}$	Non-integer phase ambiguity	cycles
$N^s_{r,j}$	Integer phase ambiguity	cycles
$\phi_{r,j}(t_0)$	Initial receiver phase offset	cycles
$\phi^s_{,j}(t_0)$	Initial satellite phase offset	cycles
λ_j	wavelength at frequency j	m
$c \cdot d^s_{,j}$	Code satellite instrument delay	m
$c \cdot d_{r,j}$	Code receiver instrument delay	m
$c \cdot \delta^s_{,j}$	Phase satellite instrument delay	m

Symbol	*Definition*	*Units*
$c \cdot \delta_{r,j}$	Phase receiver instrument delay	m
$\Phi^s_{r,21}$	Frequency-difference of phase observables	m
$P^s_{r,21}$	Frequency-difference of code observables	m
$\iota^s_{r,21}$	Frequency-difference of ionospheric delay	m
C^s_r	Constant term over each satellite arc	m
$d_{r,21}$	Receiver DCB	s
$d^s_{,21}$	Satellite DCB	s
$STEC$	Slant Total Electron Content	TECU
z	Zenith angle of satellite	rad
z'	Zenith angle at IPP	rad
R_e	Radius of Earth	m
H_{ion}	Height of the ionospheric layer (fixed)	m
F^s	Mapping function	
$\mu_{21} = \mu_1 - \mu_2$	Frequency-difference of μ_j	
$VTEC$	Vertical Total Electron Content	TECU
φ_g	Geomagnetic latitude at IPP	rad
s	Sun-fixed longitude at IPP	rad
λ_g	Geomagnetic longitude at IPP	rad
$VTEC_0$	$VTEC$ at receiver location	TECU
φ_{g_0}	Latitude at receiver location	rad
s_0	Sun-fixed longitude at receiver location	rad
f'	First order derivative	
f''	Second order derivative	
$\widetilde{DCB^s}$	Receiver DCBs lumped with satellite DCBs($= (d_{r,21} - d^s_{,21})$)	s
el	Elevation angle of satellite	rad
t	Time step	
t_{max}	Maximum number of time steps	
$\hat{\boldsymbol{x}}_{\mathbf{0|0}}$	Initial estimate of unknowns	
$\mathbf{P}_{\hat{\mathbf{x}}_{\mathbf{0|0}}}$	Variance matrix of $\hat{x}_{0\|0}$	
$\mathbf{A}^{\boldsymbol{T}}_{\mathbf{0|0}}$	Design matrix	

Symbol	*Definition*	*Units*
$\mathbf{Q_y}$	Stochastic model of observations	
$\boldsymbol{y_{0\|0}}$	Observation vector	
$\boldsymbol{\Phi_{t\|t-1}}$	Transition matrix	
$\boldsymbol{\hat{x}_{t\|t-1}}$	Predicted unknowns	
$\boldsymbol{\hat{x}_{t-1\|t-1}}$	Unknowns from previous time step	
$\mathbf{S_t}$	Variance matrix of the system noise	
$\boldsymbol{v_t}$	Predicted residuals	
$\mathbf{Q_{v_t}}$	Variance matrix of predicted residual	
$\mathbf{K_t}$	Kalman gain matrix	
$\boldsymbol{\hat{x}_{t\|t}}$	Updated unknowns	
$\mathbf{P}_{\hat{\mathbf{x}}_{\mathbf{t\|t}}}$	Variance matrix of $\boldsymbol{\hat{x}_{t\|t}}$	
H_{eff}	Effective height of the single layer model	m
$hmF2$	Height of the peak electron density for F2 layer	m

Contents

Acknowledgements vii

Abstract xi

Abbreviations, acronyms and symbols xv

List of Figures xxix

List of Tables xxxv

1 Introduction 1

1.1 Motivation . . . 1

1.1.1 The Developments in Radio Astronomy . . . 1

1.1.2 The Earth's Ionosphere . . . 4

1.1.3 Ionospheric Isoplanatic Patch . . . 11

1.1.4 Ionospheric Effects on Low Frequency Arrays . . . 12

1.1.5 Need for an Alternate Source of Ionospheric Corrections . 15

1.1.6 On Using GPS and GLONASS to Derive Ionospheric Information . . . 16

1.2 Scope of Thesis . . . 19

1.3 Thesis Outline . . . 20

1.4 Statement of Originality . . . 21

1.5 Contributions by Others . . . 22

2 MWA, GNSS and the Ionosphere 25

2.1 Physics of the Ionosphere . . . 25

2.1.1 Interaction of Plasma and Magnetic Field 26
2.1.2 Refraction of EM Waves Through Ionosphere 27
2.2 The Ionospheric Delay 29
2.3 Low Frequency Interferometers and the Ionosphere 31
2.3.1 Ionospheric Effects on MWA 33
2.4 The GNSS Observables and the Ionospheric Delay 37
2.5 The GPS Observables 38
2.5.1 The GPS Observation Equation 38
2.6 The GLONASS Observables 40
2.6.1 GPS and GLONASS Observation Model 41
2.7 Summary 42

3 Comparison of First Order Ionospheric Effects Obtained Using Single-Station GPS Models and MWA Observations 43
3.1 Introduction 43
3.1.1 GPS Studies of the Ionosphere 44
3.1.2 MRO Studies of the Ionosphere 45
3.1.3 The Need for Better Resolution 46
3.2 Estimation of the Ionosphere Using GPS Observations 47
3.2.1 Ionospheric Modelling Using GPS 47
3.2.2 Ionosphere Model Coefficients 49
3.2.3 VTEC Determination Through Kalman Filtering 50
3.3 GPS Data Preparation 53
3.3.1 GNSS Data Pre-Processing 53
3.3.2 CODE IONEX Maps 58
3.4 Measurement of the Ionosphere Using MWA Observations 60
3.4.1 MWA Observations 60
3.4.2 MWA Ionospheric Modelling 61
3.5 Results and Discussion 62
3.5.1 Comparison of VTEC With CODE IONEX 62
3.5.2 Comparison of Receiver DCBs 70
3.5.3 Comparison of GPS Ionospheric Gradients With the MWA Observed Gradients 71
3.6 Summary 74

4 Comparison of First Order Ionospheric Effects Obtained Using Multi-Station GPS Models and MWA Observations **79**
4.1 Introduction . . . 79
4.2 Ionospheric Modelling Using GPS and GLONASS . . . 81
4.2.1 GPS and GLONASS Observation Model . . . 81
4.2.2 Single-Station versus Multi-Station Approach . . . 82
4.2.3 Effective Height of the Ionosphere Layer . . . 85
4.2.4 GNSS Multi-Station Modelling Using Retrieved STEC . . . 88
4.3 MWA Ionosphere . . . 93
4.4 Results and Discussion . . . 93
4.4.1 Comparisons of Ionosphere Gradients - Single-Station v/s Multi-Station Approach . . . 93
4.5 Summary . . . 94

5 Conclusions **101**
5.1 Thesis Summary . . . 101
5.1.1 Ionospheric Modelling Using GPS and GLONASS . . . 101
5.2 Scope for Future Work . . . 102
5.2.1 The Future Low Frequency Radio Astronomy . . . 102
5.2.2 Future Prospects for GNSS . . . 103
5.2.3 Proposed GNSS Station Installations . . . 104

Bibliography **107**

A Publications **115**

List of Figures

1.1 A graphical representation of the day time and night time vertical electron densities of ionosphere (courtesy SWS (Space Weather Service)). The figure is for illustrative purpose only. 6
1.2 The relationship between solar cycles and maximum frequencies supported by E, F1 and F2 layers for Canberra. Vertical lines indicate the start of each year. Note also the seasonal variations (courtesy SWS) 10
1.3 Scintillation index at GPS L1 (1575.42MHz) assuming constant local time (=2300) at all longitudes (courtesy SWS) 10
1.4 A graphical representation to show the effects of ionosphere on radio astronomical observations, courtesy Loi et al. (2016b). For illustrating the effects, each telescope can be considered equivalent to an interferometer, collectively they represent an interferometer array. Case (a) illustrates a scenario while the radio interferometers are unaffected by the ionosphere, since there is no change in the differential phase. Case (b) shows the effect of refraction, which is seen as linearly varying across the interferometer and would manifest as a position shift of the source. Case (c) illustrate the higher order ionospheric spatial variations, which can cause shape distortions. Case (d) presents a scenario which has sufficiently small irregularities (with respect to the interferometer array), a non-linear diffraction effect manifests as scintillation of the sources. 13

1.5 The MWA 128 tile distribution 14
1.6 A schematic depiction of GPS (6 orbital planes) and GLONASS (3 orbital planes) satellite constellation 17
1.7 A schematic depiction of global GPS satellite ground tracks (cyan lines) 18
1.8 A schematic depiction of global GLONASS satellite ground tracks (cyan lines) 18

2.1 Electron motion in presence of magnetic field 27
2.2 A graphical representation for classification of an interferometer, for the ionospheric effects, as a function of baseline length ($\overrightarrow{D}$) and antenna/tile FoV and isoplanatic patch size (I_p) 34
2.3 A basic two-element interferometer 35
2.4 A schematic representation of errors in GPS observables 39

3.1 Ionosphere single layer model representation. 49
3.2 Flow chart describing the implementation of a Kalman Filter. . . 52
3.3 Selected GPS station locations from Geoscience Australia's network (red), MWA location (blue) and MWA IPP (green) for the four MWA observation nights (DOY 062, 063, 065 and 075 marked by 1 to 4). 55
3.4 An example of a cycle-slip for GLONASS satellite, before repair (red) and after the cycle-slip is repaired (blue). 58
3.5 Global TEC (TECU) from CODE IONEX maps for DOY 062, year 2014. 59
3.6 Average RMS (1-σ uncertainties) in TECU, of CODE IONEX maps for DOY 062, year 2014, marked in white are the GPS/GNSS stations considered for the solution. 60
3.7 GA station locations (red) with satellite IPPs in earth fixed reference frame over a period of 24 hours (grey) and for 1 hour during the MWA observations (black). The MWA is marked in blue, whereas the IPP of the MWA is shown in green. 61

3.8 Offset (extrapolated to $\lambda = 0$), gradient (ionospheric offset at 150 MHz), and reduced χ^2 of a fit of source position offset as a function of λ^2. Each point is for a single observation, all quantities are averaged over all (100) sources detected in that observation. Left panels are for the East-West position offset (Right Ascension) right panels are for the North-South position offset (Declination). Red, Yellow, Green, Blue and Purple are for the 88 MHz, 118 MHz, 154 MHz 185 MHz and 215 MHz bands respectively. Note that the gradients (in arcmin m^1) have been multiplied by 4, representing an offset at a wavelength of 2 m (=150 MHz). Note that a different observation is used for self calibration for each frequency band, resulting in an arbitrary DC offset for each band. 63

3.9 Source position offset against λ^2 (m^2) for a strong source. Each line represents a measurement of the source in each of four sub-bands in a single 2-minute observation. There are many lines since the source in multiple observations as it passes through the field of view. Left panel presents the East-West position offset (Right Ascension) right panel presents the North-South position offset (Declination). Red, Yellow, Green, Blue and Purple are for the 88 MHz, 118 MHz, 154 MHz 185 MHz and 215 MHz bands respectively. More significant detections are given a darker colour. Note that each band is calibrated seperately, so there is an arbitrary offset in the gradients between each of the 5 bands. 64

3.10 $VTEC$ at stations MRO1, MTMA, YAR3, and WILU estimated using the method described in the text (blue curve) and CODE IONEX (red curve) on DOY 062, year 2014. 65

3.11 $VTEC$ at stations MRO1, MTMA, YAR3, and WILU estimated using the method described in the text (blue curve) and CODE IONEX (red curve) on DOY 063, year 2014. 66

3.12 $VTEC$ at stations MRO1, MTMA, YAR3, and WILU estimated using the method described in the text (blue curve) and CODE IONEX (red curve) on DOY 065, year 2014. 67

3.13 $VTEC$ at stations MRO1, MTMA, YAR3, and WILU estimated using the method described in the text (blue curve) and CODE IONEX (red curve) on DOY 075, year 2014. 68

3.14 Differences in $VTEC$ w.r.t CODE for stations MRO1, MTMA, YAR3, and WILU for DOY 062, 063, 065 and 075 year 2014. . . 69
3.15 Comparison of our estimated receiver DCBs (blue) with BERNESE estimates (red) and CODE DCBs (cyan) for DOY 062, 063, 065 and 075, year 2014. 72
3.16 EW and NS ionosphere gradients for selected GA stations and MWA for DOY 062, 063, 065 and 075 for year 2014. The time window related to MWA observations is shown by red line. . . . 74
3.16 EW and NS ionosphere gradients for selected GA stations and MWA for DOY 062, 063, 065 and 075 for year 2014. The time window related to MWA observations is shown by red line. . . . 75

4.1 Retrieved STEC for the selected GA GNSS stations on DOY 062, year 2014, each colour represents one complete satellite arc/pass. 83
4.1 Retrieved STEC for the selected GA GNSS stations on DOY 062, year 2014, each colour represents one complete satellite arc/pass. 84
4.2 Effect on estimated VTEC and receiver DCBs by the choice of H_{ion}, H_{ion} is varied between 350 to 550 km in steps of 50 km. . . 84
4.3 Temporal variation of $hmF2$ and H_{eff} obtained from IRI-Plas ionosphere profiles at the Taylor series expansion point. 86
4.4 HmF2 global map from IRI-Plas model for DOY 062, 2014. . . . 87
4.5 Effect on estimated ionosphere gradients by the choice of H_{ion}, H_{ion} is varied between 350 to 550 km in steps of 50 km. 88
4.6 Selected GNSS station locations from Geoscience Australia's network (red), MWA location (blue) and MWA IPP (green) for the four MWA observation nights (DOY 062, 063, 065 and 075 marked by 1 to 4, respectively) 90
4.7 Ionosphere single layer model representation, earlier presented in Chapter 3 as Figure 3.1. 91
4.8 A snapshot of MWA IPP (blue), GA GNSS stations (red), and satellite IPPs for 1 hour during MWA observations (gray) in Earth-fixed reference frame, on DOY 062, 2014. The MWA IPP is considered for the Taylor series expansion point. 92

4.9 EW ionosphere gradients observed from GNSS data [blue(H_{ion}) and red(H_{eff})] and the MWA (green) using single-station approach, GPS only (G, left column) and multi-station approach, GPS+GLONASS (GR, right column) on DOY 062, 063, 065 and 075, year 2014. . 96
4.9 EW ionosphere gradients observed from GNSS data [blue(H_{ion}) and red(H_{eff})] and the MWA (green) using single-station approach, GPS only (G, left column) and multi-station approach, GPS+GLONASS (GR, right column) on DOY 062, 063, 065 and 075, year 2014. . 97
4.10 NS ionosphere gradients observed from GNSS data [blue(H_{ion}) and red(H_{eff})] and the MWA (green) using single-station approach, GPS only (G, left column) and multi-station approach, GPS+GLONASS (GR, right column) on DOY 062, 063, 065 and 075, year 2014. . 98
4.10 NS ionosphere gradients observed from GNSS data [blue(H_{ion}) and red(H_{eff})] and the MWA (green) using single-station approach, GPS only (G, left column) and multi-station approach, GPS+GLONASS (GR, right column) on DOY 062, 063, 065 and 075, year 2014. . 99
4.11 Difference in the height component of the IPP coordinates (centred at MWA), computed using a fixed height (H_{ion}=450 km), and variable height (H_{eff}, as defined in Section 4.2.3) from IRI-Plas model, at 12 noon LT (left column) and 12 midnight LT (right column) 99

5.1 Current (green) and proposed (red) GNSS station locations in vicinity of MRO. The MWA location is marked in blue. 105

List of Tables

2.1 An example of the effect ionospheric phase delay on MWA and GNSS observations. First (ΔI_1) and second order (ΔI_2) phase ionospheric delays are given for per unit change in TEC. The magnetic field, $\mathbf{B}$ is considered to be 53 500 nT, the argument of the magnetic field angle, $\cos\theta_m$, is assumed to be equal to 1. 31

3.1 Description of the selected GA network GPS/GNSS stations and the MWA 54

3.2 Daily solar and geomagnetic indices for the selected MWA observation days 56

3.3 Differences between our estimated receiver DCBs with BERNESE and CODE for DOY 062, 063, 065 and 075, year 2014. 71

3.4 Correlation between the GPS and MWA observed gradients in EW (r_{EW}) and NS (r_{NS}) components, its standard error (σ_r), and IPP separations in longitude ($|\Delta\lambda_{IPP}|$) and latitude ($|\Delta\phi_{IPP}|$) of GPS stations and MWA (ΔIPP) for DOY 062, 063, 065 and 075, year 2014. 76

3.5 Inter-station correlation for the EW and NS gradients (r), its standard error (σ_r), and IPP separations in longitude ($|\Delta\lambda_{IPP}|$) and latitude ($|\Delta\phi_{IPP}|$) between GPS stations 77

4.1 Description of the selected GA GPS/GNSS stations and the MWA. Data were available for all the four observing sessions, DOY 062, 063, 065, and 075, year 2014. The acronyms given under GNSS, G and GR stand for GPS only and GPS+GLONASS, respectively. 89
4.2 Correlation between the GNSS and MWA observed gradients in EW (r_{EW}) and NS (r_{NS}) components, its standard error (σ_r) using single-station approach and multi-station approach. 95

1 Introduction

1.1 Motivation

The research work presented in this thesis can be broadly classified under three areas of radio science, the radio wave propagation through ionosphere, the radio astronomy, and the radio satellite communications. In this chapter we have made an attempt to give a background for each of the above mentioned three areas, however the reader is encouraged to go through Davies (1990); Zolesi & Cander (2014) for further reading on ionosphere, Thompson et al. (2004) for radio astronomy and Hofmann-Wellenhof et al. (1993); Seeber (2003); Leick (2004) for satellite based radio communications using the Global Positioning System (GPS) and GLONASS. We begin by revisiting the timelines of observing with radio astronomy, from the early years till the very recent, and understand the most deserved attention that ionosphere has gained.

1.1.1 The Developments in Radio Astronomy

During the early years of radio astronomy, around 1930s, Janksky's experiments were able to record shortwave (14.6 m wavelength, 20.5 MHz) and longwave (6936 m, 43 KHz) static (Jansky, 1932). The statics were found to be originating from a three distinct groups, firstly from local thunderstorms centers, secondly from distant thunderstorms refracted by the ionosphere, and thirdly a '*hiss static*', which was seen to come from a fixed direction, had a sidereal repeatability. After analysing the *hiss static* for an year of observations, it was confirmed to be originating from our Milky way galaxy (Jansky, 1933). It was also noted that the *hiss static*, while observed on short waves, was extremely weak, hence the receivers had to be designed to be very sensitive (Jansky, 1932).

Jansky further carried his experiments, observations were made on 14 m, 16.7 m, and 32.2 m (Jansky, 1937). The observations were made during the peak of the solar cycle of 1937 and were found to have been affected by the ionosphere, rendering most of the data inconclusive.

As the advancements in radio astronomy continued, there was a need to increase the angular resolution of the telescope. Considering that the angular resolution being proportional to the aperture wavelength and the observing frequency, a feasible approach at that time was to make a single parabolic dish which operated at high frequencies. Grote Reber, inspired by the works of Karl Jansky, became the world's first radio astronomer and engineered a 31 foot telescope in Wheaton, Illinois. The telescope, a 31 foot paraboloidal reflector operating at 160 MHz (187 cm), was installed in Wheaton, Illinois in 1939 (Sullivan, 2005). The receiver components were then upgraded by 1943 to provide a more sensitive and stable system.

Another approach, to improve the angular resolution, is by making use of the radio interferometers. While working in Macroni Wireless Telegraph Company, UK, Thomas Lydwell Eckersley used an interferometer for ionospheric studies post world war I (Eckersley, 1938). The developments in radio interferometry benefited from the post world war II advances, in Australia and England, both from the infrastructure and skills available (Sullivan, 1991). In October 1945 in Australia, at CSIR Radiophysics Laboratory, Joseph Pawsey with his team developed a Sea Cliff Interferometer. The Sea Cliff interferometer was a single antenna operating at 200 MHz, additionally the reflections from the sea surface were used, to form an interferometer, and were used to monitor the solar activity. Spoelstra & Yi-Pei (1995) studied the small-scale ionospheric irregularities ($\sim$25 to 500 m) as a function of ionospheric diffraction, by using the Westerbork Synthesis Radio Telescope (WSRT), with maximum baseline length of 2.7 km, operating at frequencies 327 and 608.5 MHz (corresponding to primary beam of 2.6° and 1.38°, respectively). One of the effects of ionospheric diffraction is scintillation, which is seen to affect the incoming EM wave, and is discussed in detail in the coming sections.

With Very Long Baseline Interferometry (VLBI), extremely high angular resolutions can be achieved with intercontinental interferometer baselines. VLBI can also be used to study the absolute ionosphere, since due to very long VLBI baselines, the ionosphere is incoherent for the two antennas forming the interferometer. Absolute values of ionosphere ($VTEC$ - Vertical Total Electron Content)

were estimated by VLBI, GPS and compared with Center for Orbit Determination in Europe (CODE) global ionosphere maps by Hobiger et al. (2006). In comparison to CODE estimated $VTEC$, GPS and VLBI estimated $VTEC$ lied between ± 6 and ± 10 TECU, respectively (1 TECU $= 10^{16}$ electrons m^{-2} (Hobiger et al., 2006).

The technological advances have seen a rapid advancement post the second world war, with the development of new antennas designed for radio communication. Some of the disposed equipment by the military, post 1945, also found use in radio astronomy, for example, the 7.5 m diameter 'Würzburg Riese' paraboloid antenna from the German radar system was deployed in several locations in Europe for radio astronomy. The earlier research using Radar, found that the fluctuations in cosmic radiations, caused due to discrete radio sources (Hey & Stewart, 1946), these radio sources were further identified by Bolton (1948). These findings helped to get attention of the scientific community and resulted in further research and development in radio astronomy. In 1944, van de Hulst predicted the existence of 21 cm hydrogen line (van de Hulst, 1945) (for English translation, refer Sullivan (1982)). This was followed by the discovery of neutral hydrogen (HI), at 21 cm, from our Milky way galaxy by Ewen & Purcell (1951). Hydrogen being the main building block of our Milky way galaxy, with this discovery the foundation for mapping Milky way galaxy using hydrogen was hence laid. In Australia, Joseph Lade Pawsey used the existing Air Force radar antennas installed in north of Sydney in Collaroy to study the temperature of the surface of the Sun (at 200 MHz) as well as the ionosphere (Pawsey, 1946; Pawsey et al., 1951).

With the success of the 31 foot reflector (operating at 160 MHz) installed at Illinois, US, there was a desire to explore the universe at higher frequencies. An inverse intensity versus frequency relation was established, with the positive outcomes obtained by observing at 160 MHz, observations were further carried at 480 MHz (Sullivan, 2005). Other examples of large parabolic reflector telescopes include Parkes Observatory, Australia (1-10 GHz, 64 m diameter), Arecibo Observatory, Puerto Rico (8 to 2380 MHz, 305 m diameter), among others.

By observing at higher frequencies, above 2 GHz, the ionosphere is not seen to affect the radio interferometry observations significantly (Spoelstra & Kelder, 1984). With the current developments in electronics radio communications, radio astronomers now aim to achieve the science goals, like Epoch of Reionisation, which were earlier not possible due to high sensitivity requirements. The current and next generation of radio telescope involve numerous dipoles operating

at low frequencies. Radio telescope arrays like Low-Frequency Array (LOFAR) (van Haarlem et al., 2013), Precision Array for Probing the Epoch of Reionization (PAPER) (Parsons et al., 2010), and the Long Wavelength Array (LWA) (Ellingson et al., 2009), Murchison Widefield Array (MWA) (Tingay et al., 2012) and the future low frequency component of the Square Kilometer Array (SKA-low) (Hall, 2005) will operate at low frequencies to achieve the desired science goals. The ionospheric effects would however be much higher at these frequencies and it is important to understand its behaviour and generate corrections for possible calibration of the ionosphere. This research works aims to characterise the ionosphere using independent observations from the GPS and GLONASS. The next section is dedicated to the ionosphere, its variability and other features are discussed in detail.

1.1.2 The Earth's Ionosphere

The Earth's ionosphere extends from 50 km above the Earth's surface to several Earth radii (Davies, 1990). The upper part of the ionosphere, above 1000 km is most commonly referred to as plasmasphere (Davies, 1990). The plasmasphere forms the lower part of the Earth's magnetosphere, consisting of cold plasma, and co-rotating with the Earth (Davies, 1990).

The atmosphere of the Earth is constantly bombarded by the solar radiation which results in ionisation of the atoms. The Sun emits radiation on a range of wavelengths, however the far ultra-violet and the x-ray radiation (emitted during high solar activity) are seen to ionise the Earth's atmosphere. Due to the x-rays and ultra-violet radiation, the atoms and molecules lose an electron leaving behind positively charged ions and free electrons. Apart from the radiation from the Sun, the travelling solar wind can also cause ionisation. However, the effect of the solar wind is observed to be reduced by the Earth's magnetosphere (magnetic field).

The rate of ionisation depends on the intensity of the solar radiation and the density of the atoms. However, if the density of the atoms is sufficiently high, the deficient, unstable atoms begin to recombine, hence reducing the number of free ions. Further, due to the atomic weight of the atoms, different atoms are distributed at different altitudes, as a function of Earth's gravity. Also, different ionising radiation reaches different altitudes of Earth's atmosphere. These effects causes forming of intermediate layers of the ionosphere. The following section

presents a discussion on the different layers of the ionosphere.

1.1.2.1 The Morphology of the Ionosphere

During the day time, the ionosphere generally consists of four layers, namely D (∼50 to 90 km), E (∼90 to 140 km), F1 (∼140 to 200 km) and F2 (∼200 to 600 km) (van Velthoven, 1990; Zolesi & Cander, 2014). However at night time, the F1 and F2 layers merge to form a single F layer (Zolesi & Cander, 2014), refer Figure 1.1.

In addition, the sporadic E region exists along the E layer. The sporadic E region however is understood to be independent of the E layer (Zolesi & Cander, 2014) and is generated by meteor showers and other phenomena. Thin clouds of high ionisation from along the E layer and are seen to reflect radio waves at much higher frequencies (100 MHz) than normal (Davies, 1990). The sporadic E is patchy and can occur in ∼100 km wide patches (Davies, 1990).

Due to the presence of layers of varying electron densities the propagating signal suffers multiple refractions. The ionospheric gradient above hmF2 causes the oblique signal paths to refract away from the Earth. Once the signal path is below hmF2 the paths will begin to refract towards the Earth. This happens at each of the ionospheric layers. The paths of the incoming wave bend/refract towards/away in the direction of propagation, in accordance to Snell's law.

Further each layer, depending upon the plasma frequency which is a function of the density of the electrons, gets affected by different proportions depending on the incoming wave frequency. The E and F layers are found to refract the medium frequency and allow penetration of the high frequency electromagnetic (EM) waves. The E layer is generally found to refract signals upto 20 MHz where as F layer upto 30 MHz. The D layer is found to strongly attenuate the EM waves of up to 8 MHz. This effect is understood to be caused due to the the plasma. The plasma frequency or the 'critical frequency' of each of the layers, which generally dictate the optical properties of the plasma, can be defined. It can be noted that the EM wave can penetrate the ionospheric layer above the critical frequency of the layer. This property of refraction of the EM waves by the ionosphere is used for radio communication applications. For astronomical applications or satellite communications, frequencies higher than the critical frequency are used to avoid loss of signal back to space.

There exists a atmospheric radio window through which EM radiation reaches

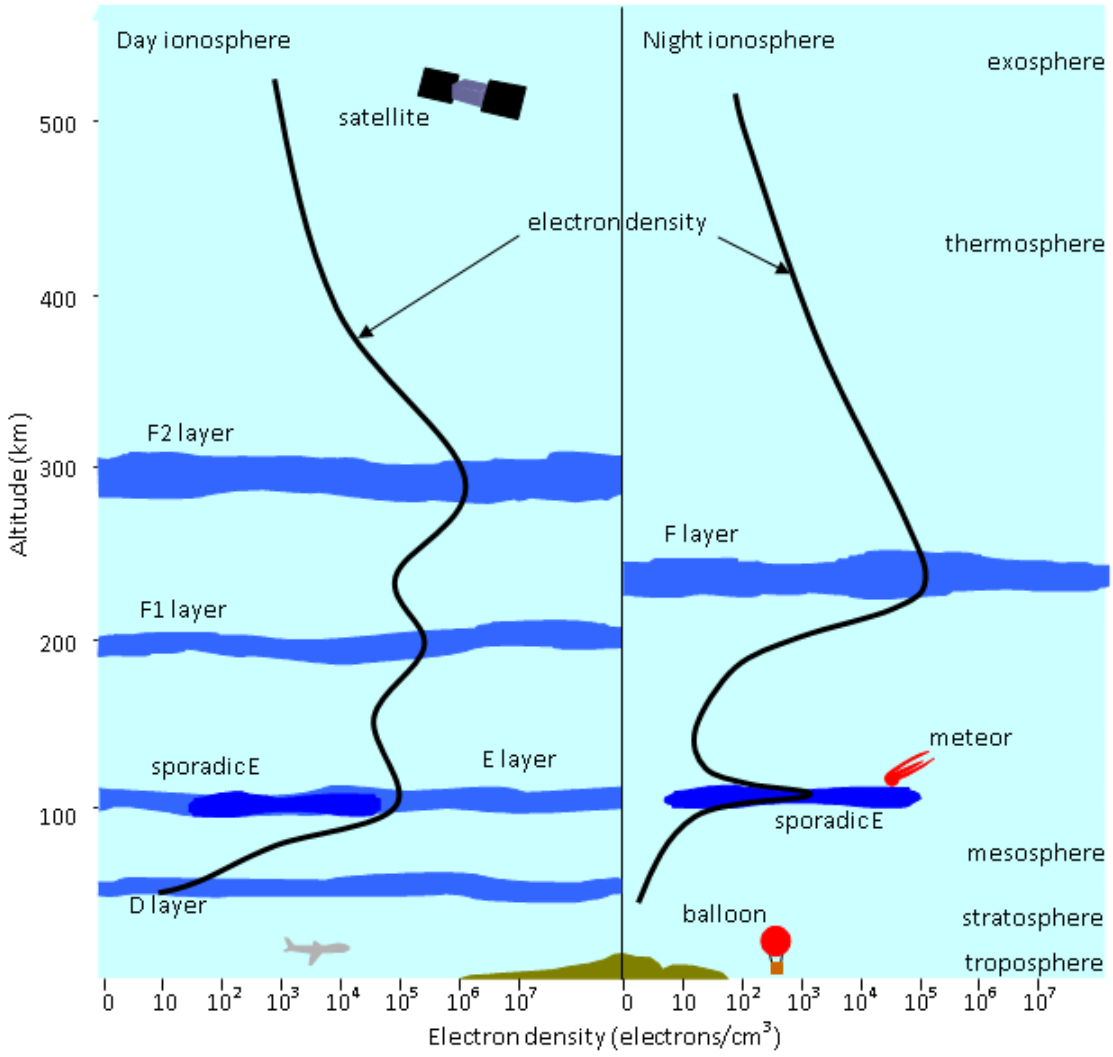

Figure 1.1: A graphical representation of the day time and night time vertical electron densities of ionosphere (courtesy SWS (Space Weather Service)). The figure is for illustrative purpose only.

the Earth. The window exists from ∼20 MHz to ∼50 GHz, the lower end is governed by the absorption and emission processes of the ionosphere and the upper end by the molecular absorption lines in the atmosphere. Astronomical and satellite communication applications make use of this atmospheric radio window.

The MWA is designed to operate between 80-300 MHz frequency bands (Tingay et al., 2012), which are much above the lower end of atmospheric radio window. The low frequency interferometer, LOFAR operates on frequencies ranging between 10-240 MHz (van Haarlem et al., 2013), the lower end of LOFAR frequencies are placed much below the atmospheric window, the capabilities to observe on such low frequencies can be exploited by observing at certain period of times while the atmospheric window is transparent.

1.1.2.2 The Solar Cycle

The activity of the ionosphere, as an effect of the emission from the Sun, is further found to vary in cycles of 11 years, see Figure 1.2. The activity of the Sun can be characterised as a function of sunspots emanating on its surface. Sunspots are found to appear in magnetic pairs, having temperature lower than its surroundings, and are highly magnetically active. Every peak of a solar cycle sees a corresponding maximum number of sunspots. Sunspots appear on the surface of the Sun and emit very high fluxes of magnetic field. The activity of sunspots lasts around 11 years, on which the length of a solar cycle is based. The maxima of the current solar cycle (Solar Cycle 24) was in 2013.

It should be noted that the perturbations in the ionosphere are found to be related to the period of solar cycles. Flares emanating from the sunspots, ionise the D layer during the day, which in turn could strongly attenuate EM waves of up to 8 MHz. One such phenomenon, termed as ionosphere scintillation, is caused due to high solar activity, is discussed briefly in the following section.

1.1.2.3 Ionospheric Disturbances

(i) Travelling Ionospheric Disturbances:

Ionosphere is found to exhibit high variability, the F layer located between ∼140 km and ∼600 km is the most variable, since it is known to hold disturbances within itself. The F2 layer (∼200-600 km), constitutes to the dynamics of the F layer, and is unarguably the most important layer from navigation and space

communication point of view. Due to its dynamics, it is also the most irregular region of the ionosphere from prediction point of view (Memarzadeh, 2009).

One of the commonly known disturbances that the F2 region withholds in itself is the Travelling Ionospheric Disturbances (TID). TID is a phenomenon associated with the collision of charged and neutral particles, induced due to passage of an internal atmospheric gravity wave, and is seen to take the form of a wave like disturbance (Yeh & Liu, 1974; Francis, 1975; Richmond, 1978).

TID's are usually divided into three classes (Rieger & Leitinger, 2002; van Velthoven, 1990) based on their latitudinal location, wavelength and velocity. The three classifications of TID's are, Large Scale TID, Medium Scale (MS) TID and Small Scale (SC) TID. The LSTID's have a wavelength larger than 1000 km and their occurrence is related to geomagnetic sub storms. MSTID are found to lie in subtropical region and have wavelength of a 100 to 1000 km and amplitude of one tenth of total ionospheric slant delay. Further, it is found that MSTID's occur more frequently than LSTID's (van Velthoven, 1990) since they are not related to extreme solar events but to the disturbance caused by the interaction of the electrons and neutral particles in the ionosphere. SSTID's have a wavelength smaller than MSTID's and period of a few minutes.

Considering the magnitude and scale of TID's, SSTID's are considered to be one of the contributors to residual position offsets for MWA data (Loi et al., 2015a). While observing with the Very Large Array (VLA) radio telescope, at 73.8 MHz, maximum antenna separation $\sim$35 km, MSTID's were detected (Dymond et al., 2011). It was further possible to evaluate the direction and speed of the MSTID with the VLA (Dymond et al., 2011). In view of future interferometers, namely SKA, with large antenna separations, MSTID's can be seen as one of the contributors towards ionospheric residual error. It is important to monitor and model TID's in order to accurately correct for ionospheric contribution in low frequency radio astronomy observations.

(ii) Ionosphere Scintillation:

Ionosphere scintillation causes fluctuation of the amplitude and phase of EM signals. This is due to the presence of small scale irregularities in the electron density, that are formed due to sudden solar bursts. Ionospheric scintillation is primarily an equatorial and high-latitude phenomenon, although it can (and does) occur with lower intensity at all latitudes. Scintillation at the equatorial

region can be found to occur at the belt around geomagnetic equator. Figure 1.3 gives a representation of geomagnetic latitude and corresponding ionospheric scintillation activity, courtesy IPS (http://www.sws.gov.au/Satellite/1/1).

In terms of geomagnetic distribution, ionospheric scintillation generally peaks in the subequatorial anomaly regions, located on average $\sim 20^\circ$ either side of the geomagnetic equator, as can be seen in Figure 1.3. This region around the magnetic equator with maximum ionisation concentration is referred to as Equatorial Ionisation anomaly (EIA). GPS receivers and telescopes located beyond 20° geomagnetic latitude are not found to be significantly affected by ionospheric scintillation.

Ionospheric scintillation can be defined as a function of the Fresnel radius, r_F. The scale size of the such irregularities, given as λ_F, as a function of the the observing wavelength, λ_0, can be given as follows (Beach, 1998),

$$\lambda_F = \sqrt{2} r_F = \sqrt{2 \lambda_0 r}$$

Now, assuming that the equivalent phase screen lies at a height (r) of 350 km from the ground observer, which yields a Fresnel scale size of 360 m for GPS $L1$ frequency (0.19 m wavelength). Hence for ionospheric irregularities at the equator with drifts of about $100\,\mathrm{m\,s^{-1}}$, and a stationary satellite, the resultant characteristic GPS scintillation timescales would be 4 s. Hence the commonly available GPS receivers, with data update rate of 30 s, are found to be incapable of detecting scintillations. High rate GPS receivers, with 1 s data latency, are specifically used to monitor scintillations. Further, the magnitude of drifts of the irregularities, is found to be atleast an order larger at high latitudes than at equator, which results in correspondingly shorter scintillation timescales. It should further be noted that, for a given GPS satellite with an eastward velocity, the net drift of the ionospheric irregularities observed by the satellite would be relative to the motion of the satellite.

The MWA, with wavelength of about 2 m at 150 MHz, the Fresnel's scale would correspond to 1.2 km. Hence for equatorial drift of $100\,\mathrm{m\,s^{-1}}$ the scintillation timescale would correspond to about 12 s. At MWA location (mid latitudes) the scintillation timescales should be shorter, about 8 to 10 s, for observations taken at zenith.

Considering the location of the Murchison Radio-astronomy Observatory (MRO), it is expected for the ionosphere to exhibit very low levels of scintillation (Ken-

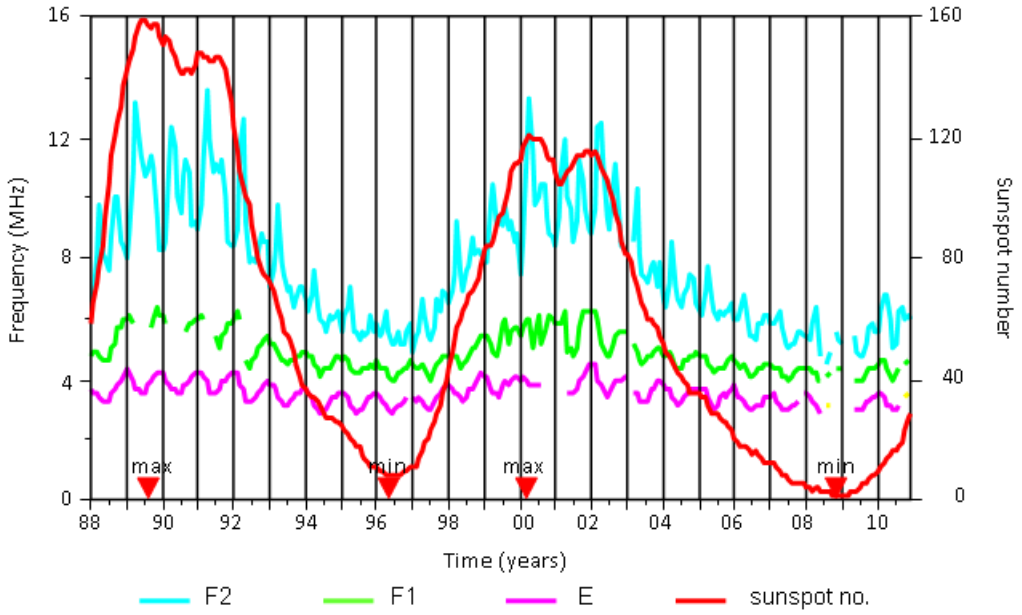

Figure 1.2: The relationship between solar cycles and maximum frequencies supported by E, F1 and F2 layers for Canberra. Vertical lines indicate the start of each year. Note also the seasonal variations (courtesy SWS)

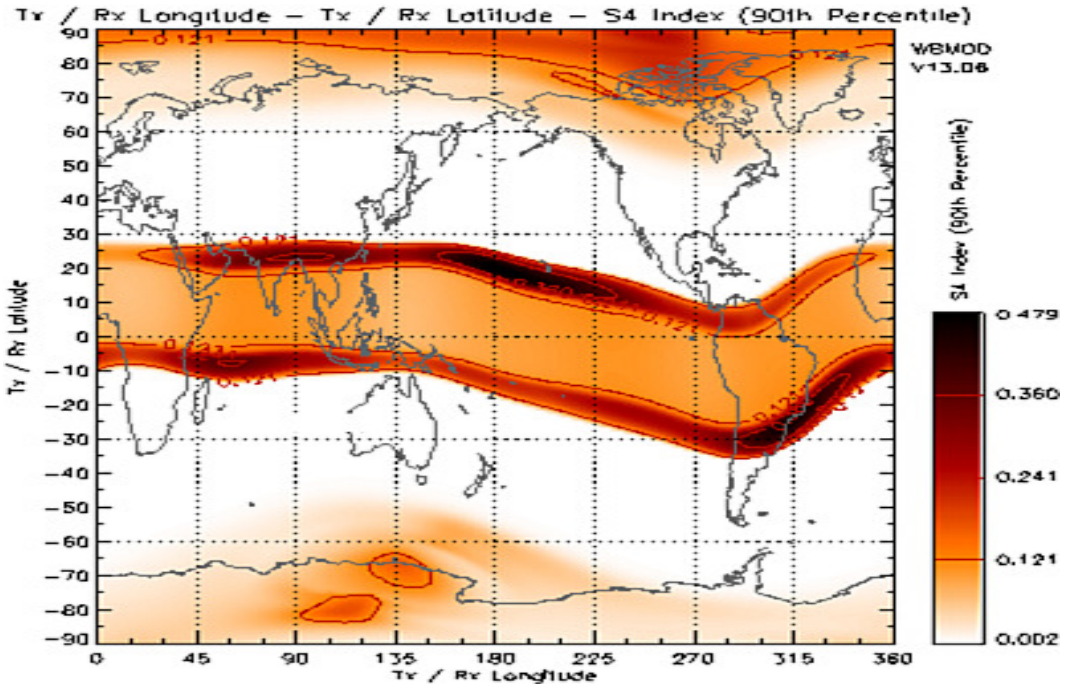

Figure 1.3: Scintillation index at GPS L1 (1575.42MHz) assuming constant local time (=2300) at all longitudes (courtesy SWS)

newell et al., 2005).

It is understood that the EM waves traversing the ionosphere would have an ionosphere induced effect. Ionosphere being inhomogenous and horizontally layered results in variation of the ionosphere with direction and altitude, refer Figure 1.1. Further, the magnitude of ionospheric delay is different for different frequencies of the EM wave, this is referred to as the dispersive property of ionosphere. The magnitude of ionospheric delay is also found to vary with the Earth's magnetic field, the ionospheric delay is found to be maximum at near the magnetic equator. This makes the ionosphere to have an anisotropic behaviour.

The ionosphere apart from varying horizontally, is found to be irregular spatially. It is important to understand the extent of its spatial irregularity and the size scales, before discussing its effect on radio astronomy. In the following section, the concept of ionospheric isoplanatic patch is discussed.

1.1.3 Ionospheric Isoplanatic Patch

The area over which the ionosphere remains spatially correlated, for an incoming wavefront, is termed as isoplanatic patch of the ionosphere. A typical size of the isoplanatic patch is found to be ∼10 km (at 74 MHz for VLA, (Cotton et al., 2004)). For radio astronomy, the phase of the incoming radiation is sensitive to the ionosphere and is proportional to f_0^{-1} (f_0 being the observing frequency), and the path length to f_0^{-2}. The field-of-view of the instrument is also a function of the observing wavelength (∼1.2 λ_0/d rad, where d = diameter of the telescope or maximum element separation for a tile). For an interferometer, while the variation in path length is small as compared to the observing wavelength, condition of isoplanatism holds true. For VLA, operating at 74 MHz, the field of view of 25 m antenna is about 13°. The isoplanatic patch size is found to be about 3°-4°, as observed by Erickson (1999), which is much smaller than the VLA FoV, hence the instrument would see different isoplanatic patches with in the FoV. For MWA, a tile (5 m x 5 m) the FoV at 150 MHz (1.9986 m wavelength) would be about 27°. Considering the observed value of isoplanatic patch size (Erickson, 1999), it would be important to account for the ionospheric correction for MWA and future interferometers.

The ionosphere is found to affect the phase of the radio astronomy observations. In the next section, we discuss the effects of the ionosphere in view of low frequency radio astronomy.

1.1.4 Ionospheric Effects on Low Frequency Arrays

he ionosphere is seen to affect the EM signal in different ways. It affects the phase of the radio astronomy observations causing a delay. For radio interferometers only the relative phase delay can be observed, hence while the ionospheric gradient is negligible across the array, there is no observed change in the differential phase, refer Figure 1.4, case (a). Further, the EM signals are found to suffer refraction (Figure 1.4, case (b)), Faraday rotation and dispersion due to the ionosphere. Due to the disturbed ionospheric conditions, the EM signals can suffer scintillation (Figure 1.4, case (d)), among other effects. Figure 1.4 illustrates the above mentioned effects of the ionosphere on radio astronomical observations. In this research work, we focus on the refraction due to the ionosphere.

With a new generation of wide-field low radio frequency telescopes now in operation, including the MWA, LOFAR, PAPER, and the LWA, interest in the effect of the ionosphere in radio astronomy is greatly renewed, and is leading to new insights in the field. These advances are required in order to understand how to design and operate the future low frequency array, the SKA-low (Hall, 2005).

The MWA, the low frequency precursor for the SKA-low located in Western Australia, has 128 aperture array elements (called tiles), has the maximum baseline length of ∼3 km, and an extreme wide Field-of-View (FoV) capability (25° full width at half maximum at 150 MHz) (Tingay et al., 2013). Figure 1.5 shows the 128 tiles distributed in East-West and North-South directions, with reference to the center of the array. These characteristics place the MWA in a regime where different paths through the ionosphere are observed for different sources across the FoV (Lonsdale et al., 2009). Recently the MWA has been funded to expand to 256 tiles and a maximum baseline of ∼6 km, which would result in finer angular resolution, for a given value of baseline length and frequency, in comparison to MWA 128 tiles. Since angular resolution $\propto 1/\overrightarrow{D}$, $\overrightarrow{D}$ being the baseline length, with $\overrightarrow{D}$ increasing by a factor ∼2, angular resolution would change by a factor ∼1/2. The sources being resolved better, a linear ionosphere approximation or a single ionosphere correction for all the sources across entire FoV may not be sufficient much of the time (Cotton, 2005).

With the MWA, 128 tile, ionospheric effects are routinely detected. For example, observations have revealed variations in the Rotation Measure of polarised point sources and the diffuse galactic background (E. Lenc, private communication). Loi et al. (2015c,d,b, 2016a) has demonstrated the utility of the MWA as a

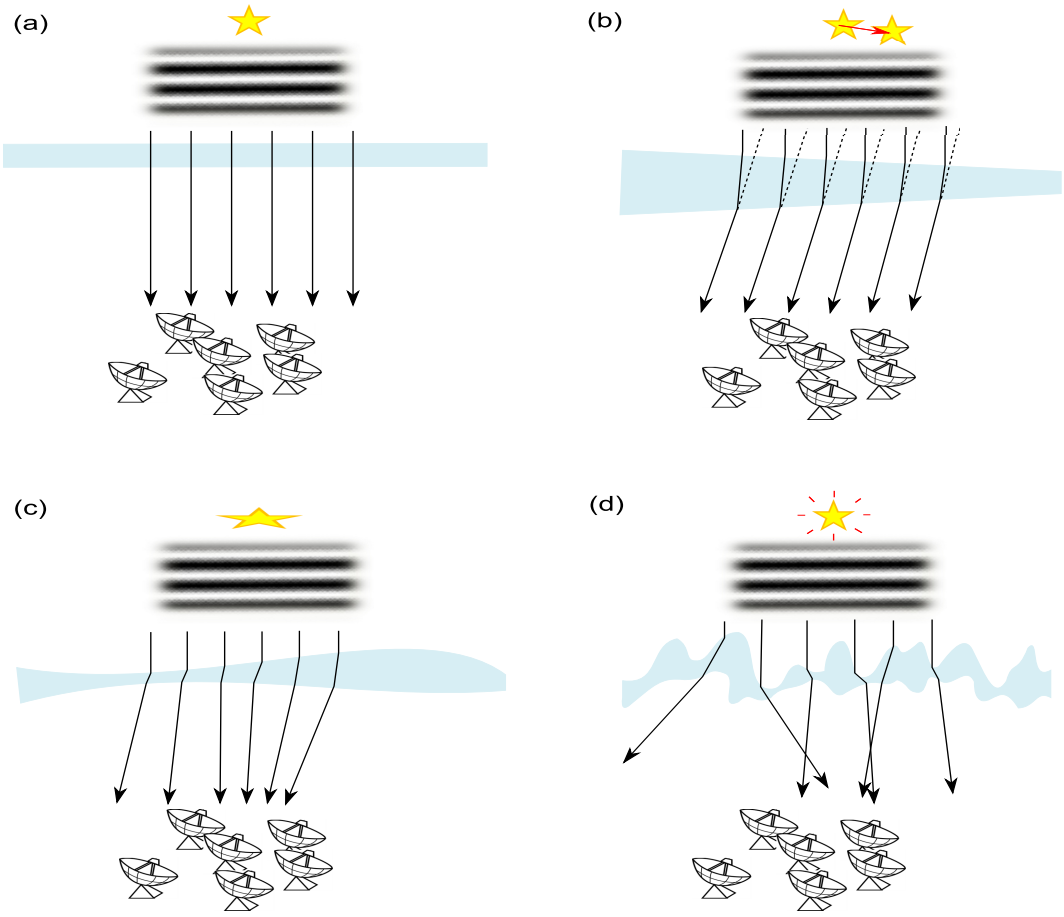

Figure 1.4: A graphical representation to show the effects of ionosphere on radio astronomical observations, courtesy Loi et al. (2016b). For illustrating the effects, each telescope can be considered equivalent to an interferometer, collectively they represent an interferometer array. Case (a) illustrates a scenario while the radio interferometers are unaffected by the ionosphere, since there is no change in the differential phase. Case (b) shows the effect of refraction, which is seen as linearly varying across the interferometer and would manifest as a position shift of the source. Case (c) illustrate the higher order ionospheric spatial variations, which can cause shape distortions. Case (d) presents a scenario which has sufficiently small irregularities (with respect to the interferometer array), a non-linear diffraction effect manifests as scintillation of the sources.

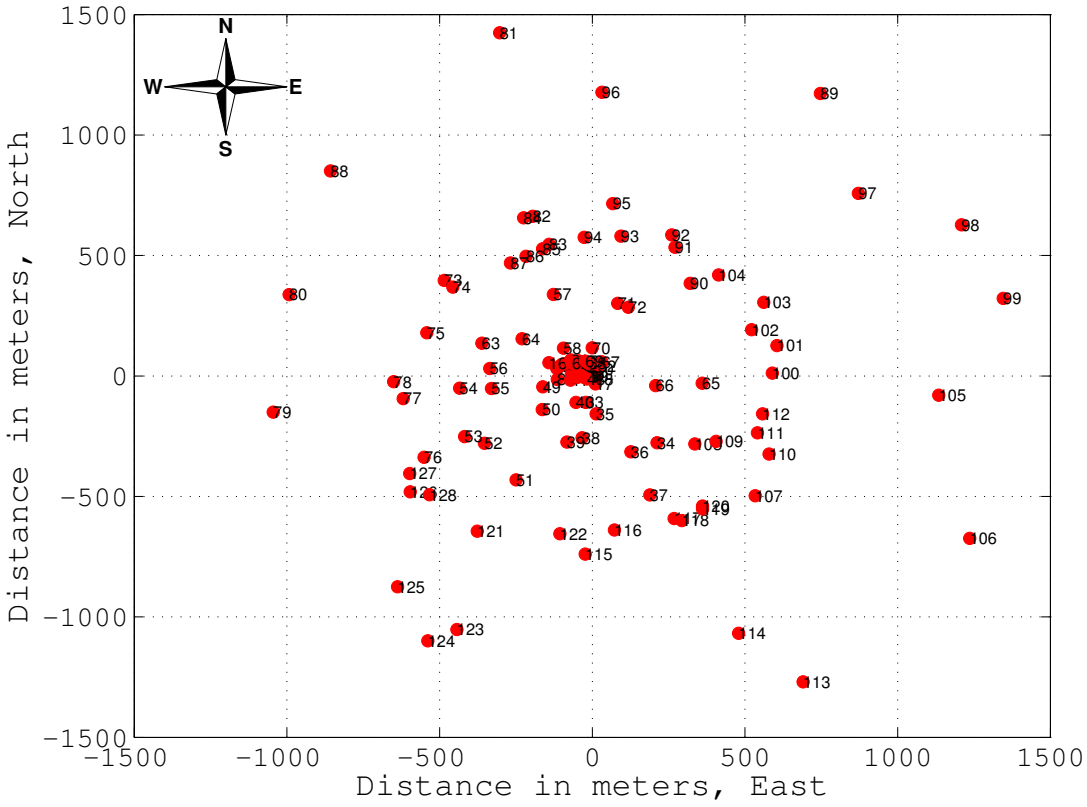

Figure 1.5: The MWA 128 tile distribution

powerful imager for studying high-altitude irregularities, revealing a population of field-aligned density ducts that appear regularly over the observatory. This illustrates the capability of the MWA to probe ionospheric structure in great detail.

The ionospheric gradients, as a function of position offset of sources, can be derived from MWA observations. While the ionospheric model is developed using external observations, from GPS, the MWA derived ionospheric gradients can be used as a reference value. This developments would equip generating the desired ionospheric corrections in view of future interferometers, namely the SKA.

1.1.5 Need for an Alternate Source of Ionospheric Corrections

The 128 tile MWA has been demonstrated as a useful tool for obtaining relative ionospheric structures (Loi et al., 2015c,d,b, 2016a). With MWA, the images were generated at 2 minutes interval, for such short intervals the ionosphere can be assumed to be constant and the visibilities can be integrated.The current MWA configuration allows for the characterisation of the ionosphere, however since the ionospheric information is dependent on the bright catalogued sources, deriving it can be challenging while the source confusion noise is higher during the passage of the galactic plane. It is important to utilise external sources like GPS/GNSS, and complement the existing ionospheric characterisation, like from the MWA.

The MWA, 256 tile configuration, will have higher angular resolution and would require different ionosphere corrections for different sources scattered across the FoV. Further, the future low frequency arrays, namely the SKA, would have narrow FoV as compared to MWA, and very high angular resolution, and would need precise direction dependent ionosphere corrections. Hence there is an emphasis laid on exploiting external sources of ionospheric information, like the GPS/GNSS.

Apart from the refraction, dispersion and Faraday rotation are also seen to affect radio astronomical observations. Refraction and Faraday rotation are relative to the antennas forming the interferometer, whereas the dispersion is based on the absolute value of TEC (Total Electron Content) observed on two different frequencies. Based on the fundamental observation for an interferometer, it is possible to capture the relative ionosphere effects but not the absolute TEC. By developing an external model of the ionosphere capable of providing with accu-

rate TEC values, it can also be possible to provide corrections for the dispersion measure.

In this research work, GPS and GLONASS observations are used to develop a model for the ionosphere. The brief description of GPS and GLONASS, and derived ionospheric products is given in the following section.

1.1.6 On Using GPS and GLONASS to Derive Ionospheric Information

The GPS was designed by the Department of Defence, U.S., in the early 1970s to fulfil U.S. military requirements (FRP, 2001). It has since been used in various civilian applications, from navigation to precise geodetic positioning. The promise of GPS to operate in all weather conditions, 24×7, in addition to its multi-frequency transmission, has made it a useful tool to monitor ionospheric parameters (El-Rabbany, 2006). In comparison to ground-based ionospheric sensors like radars and ionosondes, the satellite based system like GPS can provide continuous near real-time global coverage of the ionosphere.

A GPS constellation consists of up to 32 operational satellites placed in 6 orbital planes at an altitude of 20,200 km above the Earth's surface, refer Figure 1.6(a). With this constellation geometry and an orbital period of ∼11 h 58 min, 4 to 10 GPS satellites are visible anywhere in the world at any given time, refer Figure 1.7. The earlier GPS satellites (Block IIA (2nd generation, "Advanced") and Block IIR ("Replenishment") transmitted on two carrier frequencies ($L1$ and $L2$), each encoded with one or two digital codes, and navigation messages (El-Rabbany, 2006). The BLOCK IIR(M) ("Modernized") satellites have an additional civil signal on $L2$ ($L2C$) (Hofmann-Wellenhof et al., 1993). The BLOCK IIF ("Follow-on") satellites transmit an additional third frequency, $L5$, which has higher transmitted power and greater bandwidth, to support high-performance applications (El-Rabbany, 2006). This research work uses GPS satellite data transmitted on two GPS carrier frequencies, namely $f_1 = 1575.42$ MHz (for carrier $L1$) and $f_2 = 1227.60$ MHz (for $L2$).

GLONASS is the Russian global positioning system. It currently has 24 operational satellites in its constellation distributed in 3 orbital planes, located at an altitude of 19,100 km, refer Figures 1.6(b) and 1.8. The GLONASS satellites have an inclination of 64.8° and period of 11 h and 15 min. The GLONASS satellites continuously transmit dual frequency data centered at frequencies $f_{10} = 1602.0$

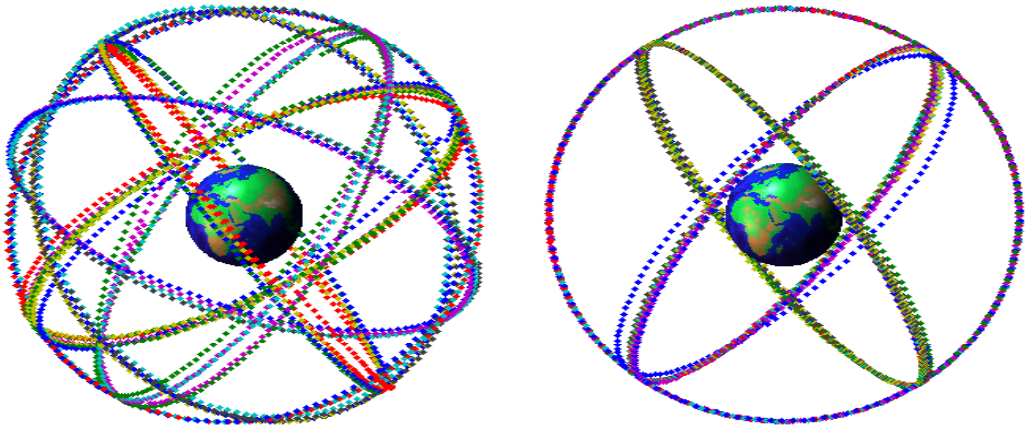

(a) GPS satellite constellation (b) GLONASS satellite constellation

Figure 1.6: A schematic depiction of GPS (6 orbital planes) and GLONASS (3 orbital planes) satellite constellation

MHz and $f_{20} = 1246.0$ MHz. Each GLONASS satellite transmits on a different frequency using a 15-channel Frequency Division Multiple Access (FDMA) technique.

Global ionospheric maps generated by global GPS and GLONASS data processing centres, namely, the CODE, the Astronomical Institute at the University of Bern (AIUB), Switzerland (Rothacher et al., 1997), and the Jet Propulsion Laboratory (JPL), California Institute of Technology, U.S (Mannucci et al., 1998; Komjathy et al., 2005), among others. The temporal and spatial resolution of global maps is generally of 2 h and 5°/2.5° in longitude/latitude, respectively.

GPS and GLONASS data are also processed at the Massachusetts Institute of Technology (MIT) Haystack Observatory by the MAPGPS software package in order to generate global TEC maps (see Rideout & Coster, 2006). The TEC maps are generated with a greater temporal and spatial resolution of 10 min and 1°/1° in longitude/latitude, respectively and are distributed through an open source, web based system[1]. To achieve even finer spatial resolution, regional ionosphere modelling must be performed. Regional ionosphere data centres like the Royal Observatory of Belgium (ROB) are able to model the ionosphere over small spatial areas with higher sampling of ground GPS stations with a temporal and spatial resolution of 15 min and 0.5°/0.5° in longitude/latitude, respectively (Chevalier et al., 2013).

[1] http://madrigal.haystack.mit.edu/

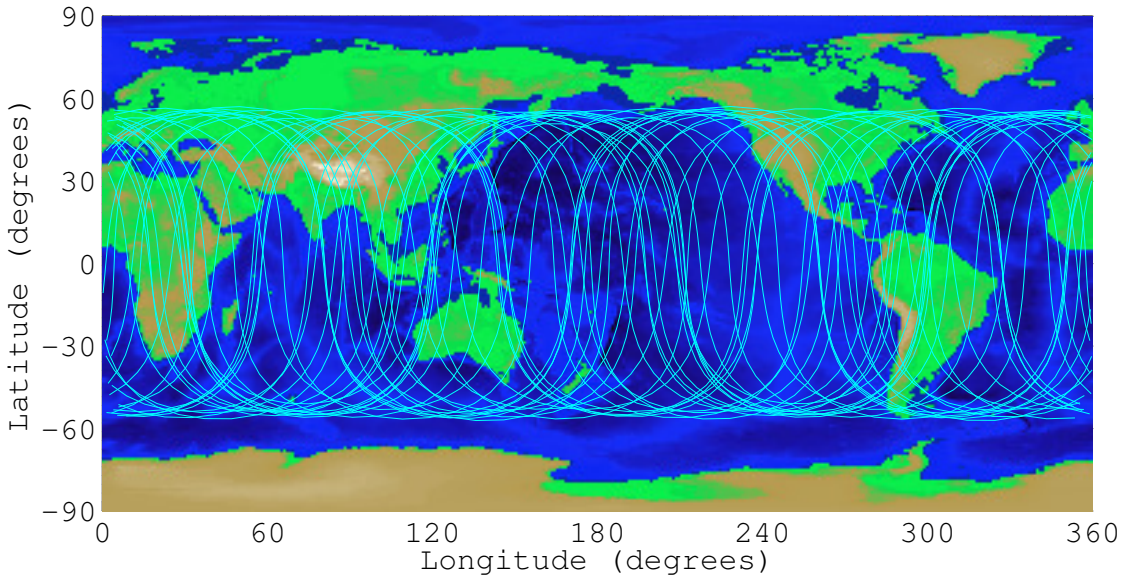

Figure 1.7: A schematic depiction of global GPS satellite ground tracks (cyan lines)

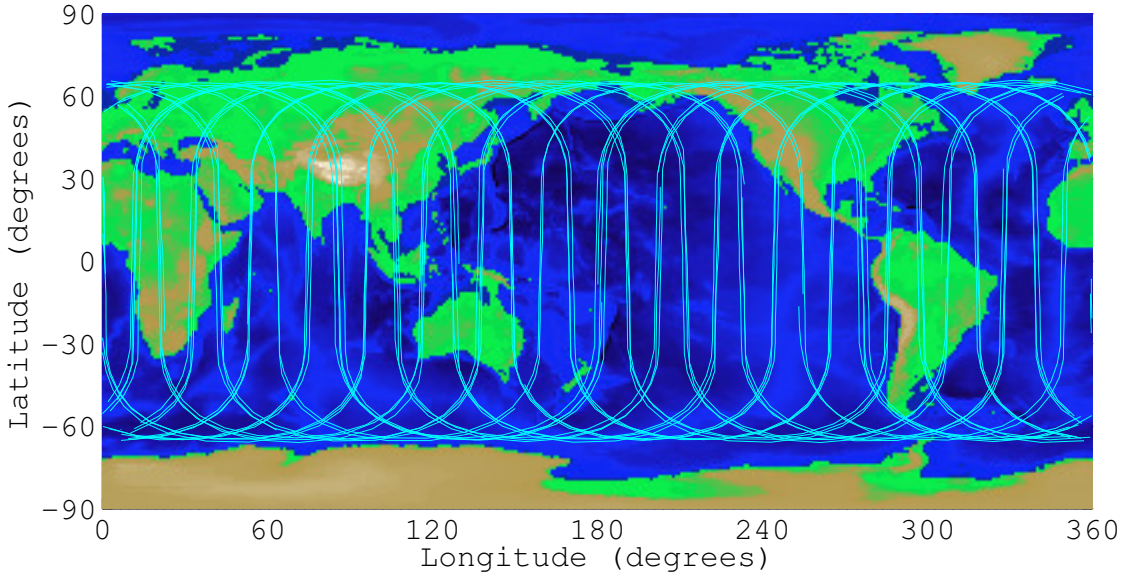

Figure 1.8: A schematic depiction of global GLONASS satellite ground tracks (cyan lines)

The global navigation satellite systems like GPS, GLONASS, BeiDou (China), Galileo (European Union) together are referred to as Global Navigation Satellite Systems (GNSS). The ionospheric information can be derived from GNSS observations. Since we make use of observations from GPS and GLONASS only, that are publicly available through Geoscience Australia (GA) archive, we refer GPS and GLONASS together as GNSS in our work. The current GNSS derived ionospheric TEC maps have too coarse resolution for MWA calibration. It is hence required to develop a regional ionospheric model by utilising the data from GNSS stations located in the vicinity of the low frequency array.

1.2 Scope of Thesis

In this thesis, a first attempt towards generating ionospheric corrections in view of calibration of the low frequency arrays has been made by utilising the GPS data located in the vicinity of MRO. The aim of the research is to utilise the current publicly available GNSS data to its full capacity, including from GLONASS, with an aim to generate ionospheric corrections as seen by MWA.

We deduce the effects of ionospheric refraction from the MWA, 128 tile configuration, and GNSS observations. The ionospheric gradients are derived from the MWA by using the GaLactic and Extragalactic All-sky MWA survey (GLEAM) observations, a bulk shift is estimated for all the bright sources within the MWA FoV. The ionospheric gradients are derived from GNSS observations using a single layer ionospheric model. The single layer ionospheric model is parameterised by second order polynomials, hence the absolute value of TEC as well as gradients are obtained. The bulk ionospheric shift from the MWA observations are compared with the GNSS derived ones.

This research work lays the foundation of obtaining ionospheric information form an independent source, the GNSS. The current GNSS infrastructure around MRO is sparse and is seen to limit the capability of GNSS to probe the ionosphere, at similar scales as MWA. This research work also highlights the shortcomings that limit the current approach for ionosphere calibration and suggests possible solutions.

1.3 Thesis Outline

The work presented in thesis is outlined as follows. Chapter 2 presents the fundamental electromagnetic wave equations for the refraction due to the ionosphere. Further, the effects of ionosphere on current and future arrays are discussed. The GPS and GLONASS observables are discussed, the observation equation for the GPS and combined GPS and GLONASS model are discussed.

Chapter 3 presents the first of the attempts to obtain ionospheric gradients from GPS observations and are compared with the ionospheric gradients obtained from the MWA observations. The MWA observations make use of the MWA, 128 tile configuration, obtained during GLEAM survey (Wayth et al. (2015); Hurley-Walker et al. (2017)). The ionospheric gradients from the MWA were obtained as a function of the position offset of the sources. A bulk ionospheric gradient over all the bright sources was used to compare with the GPS obtained ionospheric gradients. The GPS observations were used from the selective GPS stations of GA network in the vicinity of MRO. The GNSS data pre-processing methodology, which includes identifying and correcting the uncertainties in GPS and GLONASS observations is discussed. Further, the data from each of the GPS stations were used to model the ionosphere using second order polynomial. The ionosphere were assumed to be concentrated at a fixed height. This approach to model the GPS observations is referred to as single-station single layer model. The work presented in Chapter 3 can be found in the published article Arora et al. (2015).

The work done towards ionospheric modelling with GPS was further improved, which is presented in Chapter 4. The single-station, single layer model approach was upgraded to a multi-station single layer model. The data from other GNSS, namely GLONASS was incorporated in the model. The work presented in Chapter 3 assumes the ionosphere to be concentrated at a fixed height, in Chapter 4 the effective height of the ionosphere for a single layer model was investigated. The spatial and temporal variations into the effective height were incorporated using model values from external source. The comparison of the MWA obtained and multi-station GNSS ionospheric gradient model showed significant improvement as compared to single-station GPS model. The work presented in Chapter 4 can also be referred in the article Arora et al. (2016).

Chapter 5 concludes the thesis and proposes the future work ahead for ionospheric calibration of low frequency arrays. The work presented in this thesis makes a first attempt to use the publicly available GNSS observations towards

generating corrections for the ionosphere in view of calibration for low frequency arrays. The current infrastructure of the GNSS stations is limited around MRO and is seen as a shortcoming towards ionospheric calibration of the low frequency arrays. Chapter 5 highlights these problems and suggests a possible solution for the same. The installation of new GNSS stations around MRO is the solution recommended. Depending on the scales at which the MWA gets affected by the ionosphere, an approach to install the new GNSS stations is proposed. Further, considering the current infrastructure available around MRO and the requirements to install GNSS stations, plausible candidate sites for such installations are presented.

1.4 Statement of Originality

With the current developments in low frequency radio astronomy, observing instruments like the MWA, LOFAR, PAPER, LWA and the future SKA-low, aim at achieving the science goals specifically designed for low frequency, namely the Epoch of Reionisation (EoR). The ionosphere which was once an important contributor towards residual position shifts, among other effects, is seen to pose a challenge to achieve the desired science goals, especially when the antenna separation is larger than the isoplanatic patch size.

Attempts to generate ionosphere corrections have been made in the past for VLBI, observing at 8.4 and 2.3 GHz, using GPS TEC maps (Ros et al., 2000). Erickson et al. (2001) used data from collocated GPS receivers to generate ionospheric corrections for VLA (322 and 333 MHz). Ionospheric Faraday rotation corrections were computed using TEC from CODE and ROB maps for LOFAR (Sotomayor-Beltran et al., 2013).

In this research work we generate the ionospheric corrections using the observations from local GPS receivers in the vicinity of MRO. A first attempt has been made to compare the GNSS derived ionospheric corrections with ones obtained from the MWA observations (Arora et al., 2015).

The GPS observations are biased by instrumental biases of the receiver and the satellite. The global data processing centers, namely, CODE publish the values of the receiver biases, but only for the receivers used for generating the CODE product solutions. In this research work, a first attempt has been made to publish the instrumental biases of all the receivers in the vicinity of MRO (Arora

et al., 2015).

In this research work, we aim to introduce the GPS and GLONASS observation equations and errors to the astronomical community. Further, the methodology to process the GPS and GLONASS observations to model the ionosphere, including data integrity algorithms (pre-processing) are presented in detail (Arora et al., 2015, 2016).

This research work lays the foundation towards using GNSS derived ionospheric corrections for calibration of low-frequency instruments, namely, SKA-low. The current limitations towards generating resolved ionospheric corrections, at similar scales of the MWA, are identified and highlighted. The solutions towards the current limitations are proposed, which includes installation of new GNSS receivers in the vicinity of MRO, which also is a requirement towards generating more complex ionosphere models like the 3D tomography (Arora et al., 2016).

1.5 Contributions by Others

The work presented in this thesis was carried during the period 10 September 2012 till 10 March 2016. The completion of the work wouldn't have been possible without the collaborative efforts that were made with the members of the Curtin Institute of Radio Astronomy, Curtin University. The specifics oft he contributions by others are as follows:

- Chapter 3 - The integrity checks for the estimated ionosphere coefficients were done on each of the individual ionospheric terms, the $VTEC$, the gradients in the East-West (EW) and North-South (NS) directions which was proposed by Stephen Ord. The suggestion to include the second order polynomial terms for the ionospheric coefficients, to compute the GPS derived ionospheric gradients, was proposed by Steven Tingay. The MWA estimated ionospheric parameters from the GLEAM observations was carried independently by John Morgan.

- Chapter 4 - The ionospheric effects from the MWA using GLEAM observations were derived independently by John Morgan.

- Chapter 5 - The idea to propose sites near the existing infrastructure, such as homesteads and rural areas, near MRO for possible GPS station installations was proposed by Steven Tingay. The suggestions for the locations of the

proposed GNSS station installations was given by Steven Tingay. Further, discussions with David Emrich and David Kenney for GPS candidate sites were helpful.

2

MWA, GNSS and the Ionosphere

In this chapter we discuss physics of the ionosphere and derive the equations for the ionospheric refractive index. The effects of the ionosphere on radio interferometers is discussed in detail, with an emphasis on the Murchison Widefield Array (MWA). Further, using the expression for the ionospheric refractive index, the parameterisation of the ionospheric delay in GPS/GNSS observation model is done. The GPS and GLONASS system overview, the observables and the unknowns, for both GPS and GLONASS observation models, are discussed. The equations of refractive index of the ionosphere are discussed in detail in the following section.

2.1 Physics of the Ionosphere

The ionosphere is composed of free electrons and the heavier positive ions; the free electrons (with charge e, and mass m_e) and the ions, also referred to as the '*plasma*', exist in a quasi-neutral state, however have enough density to collectively affect the EM waves. In such a state, the free electrons and ions are separated by a distance known as the '*Debye length*', Debye length is the distance for which the energy required to deplete the positive ions is equal to the thermal energy. When the plasma equilibrium is disturbed, the plasma starts to oscillate, in a simple harmonic motion, with an *angular frequency* (ω_p). This results in displacement of the free electrons. Due to the presence of the electric field, the '*restoring force*' comes into play. The electrons and ions then recombine by the restoring force, to gain back their equilibrium.

The plasma frequency, f_p, as a function of the angular frequency, ω_p, can be given as follows

$$f_p^2 = \left(\frac{\omega_p}{2\pi}\right)^2 = \frac{N_e\, e^2}{4\pi^2 m_e \varepsilon_0} = 80.62\ N_e = A_p N_e \tag{2.1}$$

where, ω_p is the angular frequency of the electron ($\mathrm{rad\,s^{-1}}$), N_e is the electron density (electron/$\mathrm{m^3}$), e is the charge of electron, m_e is the mass of the electron and ε_0 is the dielectric constant. By substituting the values of the constants, $e = 1.602 \times 10^{-19}\,\mathrm{A\,s}$, $m_e = 9.107 \times 10^{-31}\,\mathrm{kg}$ and $\varepsilon_0 = 8.854 \times 10^{-12}\,\mathrm{s^4\,A^2\,m^{-3}\,kg^{-1}}$, we get the constant term for the plasma frequency, A_p ($\mathrm{m^3\,s^{-2}}$).

When an EM wave comes in contact with the ionosphere, it perturbs the state of the plasma. Further depending on the frequency of the EM wave, f, and the frequency of the plasma, f_p, we have the following conditions for the propagation of the EM wave

a. If $f > f_p$ then the EM wave propagates through the ionosphere, we have a propagating wave

b. If $f < f_p$, we have an evanescent or surface waves. When the EM waves from the Earth's surface reach the lower boundary of the ionosphere, it could both reflect and refract. However, while the angle of incidence is greater than the critical angle, the EM wave travels along the surface, resulting in an evanescent wave. The phase of the evanescent wave does not change, however the amplitude decays exponentially.

c. If $f = f_p = f_c$, f_c is known as critical frequency, the EM wave is reflected back

For a typical value of N_e, $N_e = 3.1 \times 10^{11}$ electrons/$\mathrm{m^3}$, the plasma frequency is, $f_p = 5\,\mathrm{MHz}$. This is very important with respect to High Frequency (HF) communications point of view. It could also be noted that for HF communications, all the above three mentioned conditions of wave propagation, as a function of frequency, f, are applicable. For ground radio astronomy applications, which require the propagation of EM waves to reach the telescope, we are restricted to observing well above the plasma frequency, hence condition (a.) applicable.

2.1.1 Interaction of Plasma and Magnetic Field

The Earth's magnetic field encompasses the ionosphere, the plasmasphere and beyond. In presence of the magnetic field, the electrons move along the direction

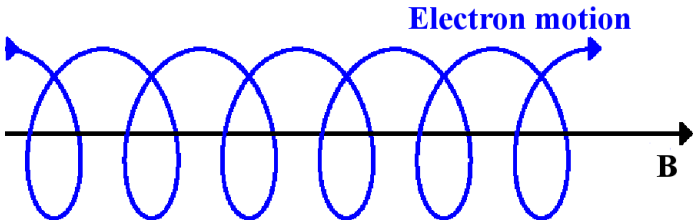

Figure 2.1: Electron motion in presence of magnetic field

of the magnetic field, refer Figure 2.1. The gyro frequency, f_g, which is a function of magnetic field, $\mathbf{B}$, can be given as follows

$$f_g = \left(\frac{\omega_g}{2\pi}\right) = \left(\frac{e}{2\pi m_e}\right)\mathbf{B} = 2.80 \times 10^{10}\,\mathbf{B} = A_g\,\mathbf{B} \tag{2.2}$$

where $A_g = (\mathrm{s\,A\,kg^{-1}})$ is the constant for the gyro frequency.

For typical values of the magnetic field, $\mathbf{B} = 53\,500\,\mathrm{nT}$, (T corresponds to Tesla, S.I. units of $\mathrm{T} = \mathrm{kg\,s^{-2}\,A^{-1}}$), the gyro frequency ($f_g$) is 1.5 MHz.

2.1.2 Refraction of EM Waves Through Ionosphere

The extraterrestrial EM signals reaching the Earth's surface, are affected by the ionosphere and the Earth's magnetic field. One of the effects that ionosphere causes is refraction of the EM waves, which can be mathematically formulated by the ionospheric refractive index. The refractive index for magnetically biased lossless (zero conductivity) homogeneous plasma is given by Appleton-Hartree formula (Appleton, 1932; Hartree, 1931), as follows

$$n_{\mp}^2 = 1 - \frac{2X(1-X)}{2(1-X) - Y^2\sin^2\theta_m \pm \sqrt{\left(Y^4\sin^4\theta_m + 4(1-X)^2Y^2\cos^2\theta_m\right)}} \tag{2.3}$$

where, θ_m is the angle that an incoming EM wave makes with the Earth's magnetic field, X is the normalised plasma frequency given as $X = \dfrac{f_p^2}{f^2} = A_p\dfrac{N_e}{f^2}$, Y is the modulus of normalised gyro frequency given as, $Y = |\mathbf{Y}| = A_g\dfrac{|\mathbf{B}|}{f}$

For GPS frequencies, assuming $Y << 2|\cos\theta_m|(1-X)/\sin^2\theta$ and values of θ up to 89 degrees, the expansion of equation (2.3) up to fourth inverse power of frequencies (Bassiri & Hajj, 1992) can be given as follows

$$n_{\mp} = 1 - \frac{1}{2}X \pm \frac{XY|\cos\theta_m|}{2} - \frac{1}{4}X\left(\frac{1}{2}X + Y^2\left(1+\cos^2\theta_m\right)\right) \tag{2.4}$$

In the equation (2.4), the two values of $n_{\mp}$ correspond to the ordinary (n_-) wave, and the extraordinary (n_+) wave. The refractive index n_+ is used while the incoming wave is Right Hand Circularly Polarised (RHCP) and n_- for Left Hand Circularly Polarised (LHCP). Depending on the angle of incidence of the incoming wave (θ_m) with the Earth's magnetic field, the wave can either be RHCP ($0 \leq \theta_m < \pi/2$) or LHCP ($\pi/2 < \theta_m \leq 0$) (Petrie et al., 2011; Moore & Morton, 2011). Due to the presence of Earth's magnetic field, the EM waves which are not one of the characteristic wave (RHCP or LHCP), suffer change in polarisation. The non-characteristic waves are separated into their components, the ordinary and the extraordinary wave, with characteristic polarisation which have different phase velocities. Due to the different phase velocities of the two waves, the total wave which is the sum of ordinary and the extraordinary waves suffers Faraday Rotation, as they recombine and are detected at the telescope. In this study, we will deal with the first order refractive index only, hence the angle of incidence of the incoming wave with the magnetic filed will not be a matter of concern. In addition to using the first order refractive index for GPS and GLONASS in our work, we additionally present a quantitative study of RHCP (second order refractive index) in the following discussion.

The expression for refractive index given in equation (2.4) corresponds to the phase refractive index. The group refractive index can be obtained by the relation $n_g = n + f(dn/df)$, given as follows

$$n_{g,\mp} = 1 + \frac{1}{2}X \mp XY|\cos\theta_m| + \frac{3}{4}X\left(\frac{1}{2}X + Y^2\left(1+\cos^2\theta_m\right)\right) \tag{2.5}$$

The above equations do not include the effect of electron collision for simplification purpose. With assumptions that massive positive ions have no effect on EM wave, plasma is a 'cold plasma', and the magnetic field remains uniform, the expression for refractive index is derived.

The refractive indexes for phase and group velocities can be formed, small terms which are less than 1 part in 10^{-9} after binomial expansion are ignored and the expression is truncated to second order (Petrie et al., 2011). The phase refractive index can be given as follows

$$
\begin{aligned}
n_{\mp} &= 1 - \frac{1}{2}\frac{A_p N_e}{f^2} \pm \left(\frac{A_p N_e A_g \mathbf{B}\cos\theta_m}{2f^3}\right) \\
&= 1 - \underbrace{40.3\frac{N_e}{f^2}}_{I_1} \pm \underbrace{\left(1.1284\times 10^{12}\frac{N_e \mathbf{B}\cos\theta_m}{f^3}\right)}_{I_2}
\end{aligned}
\tag{2.6}
$$

and for the group velocity

$$
n_{g,\mp} = 1 + \underbrace{40.3\frac{N_e}{f^2}}_{I_{g,1}} \mp \underbrace{2\left(1.1284\times 10^{12}\frac{N_e \mathbf{B}\cos\theta_m}{f^3}\right)}_{I_{g,2}} \tag{2.7}
$$

where I_1, I_2, and $I_{g,1}$, $I_{g,2}$ are the first, and second order terms for the ionosphere refractive index for phase and group, respectively.

Since for GPS and GLONASS, we include the discussion for higher order refractive index terms for RHCP only, hence the lower sign for refractive index will be used. The constant term in the second order refractive index, 1.1284×10^{12}, can be written in multiples of the speed of light c. Equations (2.6) and (2.7) can be rewritten as follows

$$
\begin{aligned}
n &= 1 - \underbrace{40.3\frac{N_e}{f^2}}_{I_1} - \underbrace{\left(\frac{1}{2}7527.87c\frac{N_e \mathbf{B}\cos\theta_m}{f^3}\right)}_{I_2} \\
n_g &= 1 + \underbrace{40.3\frac{N_e}{f^2}}_{I_{g,1}} + \underbrace{\left(7527.87c\frac{N_e \mathbf{B}\cos\theta_m}{f^3}\right)}_{I_{g,2}}
\end{aligned}
\tag{2.8}
$$

It can be noted that since the phase velocity experiences and advance and group velocity experiences a delay, the mathematical expression for the refractive index of phase is given as negative and for the group it is positive, refer equations (2.8). Also it can be noticed that the effect of second order ionosphere term is twice in magnitude for the group delay as compared to phase delay.

2.2 The Ionospheric Delay

The GPS signal transmitted by the satellite, s would have traversed the path l before being detected by a receiver, r, located at the Earth's surface. The

measured range between the receiver and the satellite has effects due to the ionosphere, given as ρ_{ion}, can be deduced from Fermat's principle, as follows

$$\rho_{ion} = \int_r^s n \ \ dl \tag{2.9}$$

where n is the refractive index due to the ionosphere

The geometric range can also be calculated by setting the refractive index as 1, n=1, given as follows

$$\rho_{ion,0} = \int_r^s dl \tag{2.10}$$

The difference between the refracted signal and the geometric signal gives the delay due to the ionosphere, as follows

$$\Delta I = \rho_{ion} - \rho_{ion,0} = \int_r^s (n-1) \ \ dl \tag{2.11}$$

By substituting the value of the ionosphere refractive index, given by equations (2.8), for phase delay (I_1) and group delay ($I_{g,1}$), equation (2.11) can be rewritten as follows

$$\begin{aligned} \Delta I &= \underbrace{-\frac{40.3}{f^2}\int N_e \ \ dl}_{\Delta I_1} \underbrace{-\left(\frac{7527.87\ c\ \mathbf{B}\cos\theta_m}{2\ f^3}\right)\int N_e \ \ dl}_{\Delta I_2} \\ \Delta I_g &= \underbrace{\frac{40.3}{f^2}\int N_e \ \ dl}_{\Delta I_{g,1}} + \underbrace{\left(\frac{7527.87\ c\ \mathbf{B}\cos\theta_m}{f^3}\right)\int N_e \ \ dl}_{\Delta I_{g,2}} \end{aligned} \tag{2.12}$$

where $\int N_e$ can be written in terms of Slant Total Electron Content ($STEC$). $STEC$ is the line-of-sight Total Electron Content (TEC, 1 TEC unit or TECU $= 10^{16}$ electrons/m^2).

The typical values of first and second order ionospheric phase delays at GNSS and MWA frequencies, for change in 1 TECU, and $\mathbf{B} = 53\,500$ nT, are given in Table 2.1.

It should be noted that, though ΔI_1 and ΔI_2 are given for change in 1 TECU. Generally, the GPS and GLONASS satellites, would see $STEC$ of the order of

Table 2.1: An example of the effect ionospheric phase delay on MWA and GNSS observations. First (ΔI_1) and second order (ΔI_2) phase ionospheric delays are given for per unit change in TEC. The magnetic field, **B** is considered to be 53 500 nT, the argument of the magnetic field angle, $\cos\theta_m$, is assumed to be equal to 1.

Observing System	Frequency MHZ	ΔI_1/TECU (m)	ΔI_2/TECU (m)
MWA	150	17.91	0.18
GPS (L1)	1575.42	0.16	0.00015
GPS(L2)	1227.60	0.27	0.00033
GLONASS($L1_0$)	1602.00	0.16	0.00015
GLONASS($L2_0$)	1246.00	0.26	0.00031

$\sim$50 to 120 TECU depending on the season, time, elevation angle of satellite and location of the receiver. The second order ionospheric delay, ΔI_2, would have a magnitude of a few centimetres for such high values of $STEC$ ($\sim$ 2-4 cm).

The frequencies at which the MWA operates, the first order ionospheric delay, ΔI_1, can have significant affect for change in 1 TECU, refer Table 2.1. However, the second order ionospheric delay, ΔI_2, presented in Table 2.1, though is relevant for studying the frequency-dependent effects on polarisation at MWA frequencies, would not significantly affect the source position, and is beyond the scope of this thesis.

In this research work, we aim to generate first order ionospheric delay corrections (ΔI_1) using GNSS observations, for possible calibration of low frequency interferometers.

2.3 Low Frequency Interferometers and the Ionosphere

The ionosphere behaves coherently for a short baseline interferometer, and can be interpreted by a simple linear relation, to the first order. This behaviour of the ionosphere is attributed to the isoplanatic patch size. The order of isoplanatic patches is generally found to be $\sim$10 km (Cotton et al., 2004), hence the antenna elements forming the interferometer, separated by distances <10

km, are understood to lie within the same isoplanatic patch size. For such a scenario, single ionospheric correction would be sufficient for the interferometer antenna elements. As the distance between the interferometer antenna elements increases (>10 km), the ionosphere can no longer be correlated, hence individual ionospheric corrections would be be required for each antenna element.

The ionosphere variation can also be classified with respect to an antenna's Field of View (FoV). The isoplanatic patch, in this context, can be described as the area within the ionospheric region over which the variation in the path length for an observed EM wave is small compared to the observing wavelength (Thompson et al., 2004). For centimetre and shorter wavelengths, the antenna beam is smaller than the isoplanatic patch size. Hence a single ionospheric correction could be applied to a single point source. For meter wavelengths, the size of the antenna beam can reach several times of the size of isoplanatic patch size. Hence within each antenna's FoV, the ionosphere would behave differently for sources lying in different isoplanatic patches, direction-dependent ionospheric corrections would be needed for calibration. Erickson (1999) estimated the size of isoplanatic patch to $\sim 3^{\circ}$ to 4° while observing at 74 MHz (4 m wavelength). Kassim et al. (2007) while observing with VLA, 74 MHZ, primary beam width of $11^{\circ}.7$ Full width at half maximum (FWHM), made use of different ionospheric corrections for sources lying in different isoplanatic patch sizes within the VLA FoV.

Based on the above two considerations, the antenna elements separation (baseline) and the FoV, a broad classification can be formed for different interferometers. The general four classifications can be, (1) while both the baseline length ($\overrightarrow{D}$) and FoV are smaller than the isoplanatic patch size (I_p), hence single ionospheric correction would be needed for both the antenna elements. Due to limited number of ionospheric unknowns, the degrees of freedom (df) for the mathematical model are very high. The interferometers separated by short distances and operating at GHz frequencies fall under this regime, for example certain VLA configurations. Scenario (2) correspond to large baseline length ($\overrightarrow{D}$) in comparison to the isoplanatic patch size. Hence different ionospheric corrections would be needed for each antenna element. However, since the FoV is smaller than the isoplanatic patch size, direction-dependent corrections would not be needed. All the VLBI configurations and some VLA configurations fall under this scenario. The df are still higher for such a scenario. Further, scenario (3) corresponds to very large FoV and short baseline lengths. Hence for both the antenna elements,

single ionospheric corrections would be needed for any given source. However, direction-dependent corrections would be needed for sources lying within different isoplanatic patches within the FoV. The *df* reduce sufficiently, however are enough to estimate the ionospheric corrections from the radio astronomy observations, for example, ionospheric corrections were estimated using MWA observations (Loi et al., 2015c,d,b). Low frequency interferometers like the MWA fall under this regime. In scenario (4), both the baseline length ($\overrightarrow{D}$) and FoV are larger than the isoplanatic patch size. Hence different ionospheric corrections would be needed for each antenna element. Further, for each antenna element, direction-dependent ionospheric corrections would be needed. Future telescopes like the SKA-low fall under this regime. For such a scenario, the *df* are very low to estimate the ionospheric corrections from the radio astronomy observations. An independent source of ionospheric corrections, like the GNSS, would help support the ionospheric calibration for future interferometers. These classifications are also referred to as ionospheric regimes (Wijnholds et al., 2010). The above mentioned four cases are also illustrated in Figure 2.2.

2.3.1 Ionospheric Effects on MWA

This research work makes use of the 128 tile configuration, MWA observations. The MWA is a low-frequency radio telescope located within the Murchison Radioastronomy Observatory (MRO) in Western Australia. The MWA is capable of imaging with wide-field of view at such low frequencies (Lonsdale et al., 2009; Tingay et al., 2013). The MWA, 128 tile configuration, has maximum baseline lengths of $\sim$3 km and FoV of $\sim$ 25°, which is classified under (3), refer Figure 2.2.

The acceptable change in the ionosphere, that leads to refraction, can be deduced by understanding the permissible change in phase of the signal. The isoplanatic patch is understood to be the characteristic scale over which the phase of the signal varies by 1 rad. The approximation for the change in phase due to ionospheric refraction can be deduced, by using the expression for phase of the interferometer, refer Figure 2.3.

The phase of the interferometer can be given as

$$\phi = \omega \, \tau_{geo} = \frac{2\pi D \sin\theta}{\lambda_0} \tag{2.13}$$

where ϕ (rad) is the phase of the interferometer, ω (rad s^{-1}) is the angular fre-

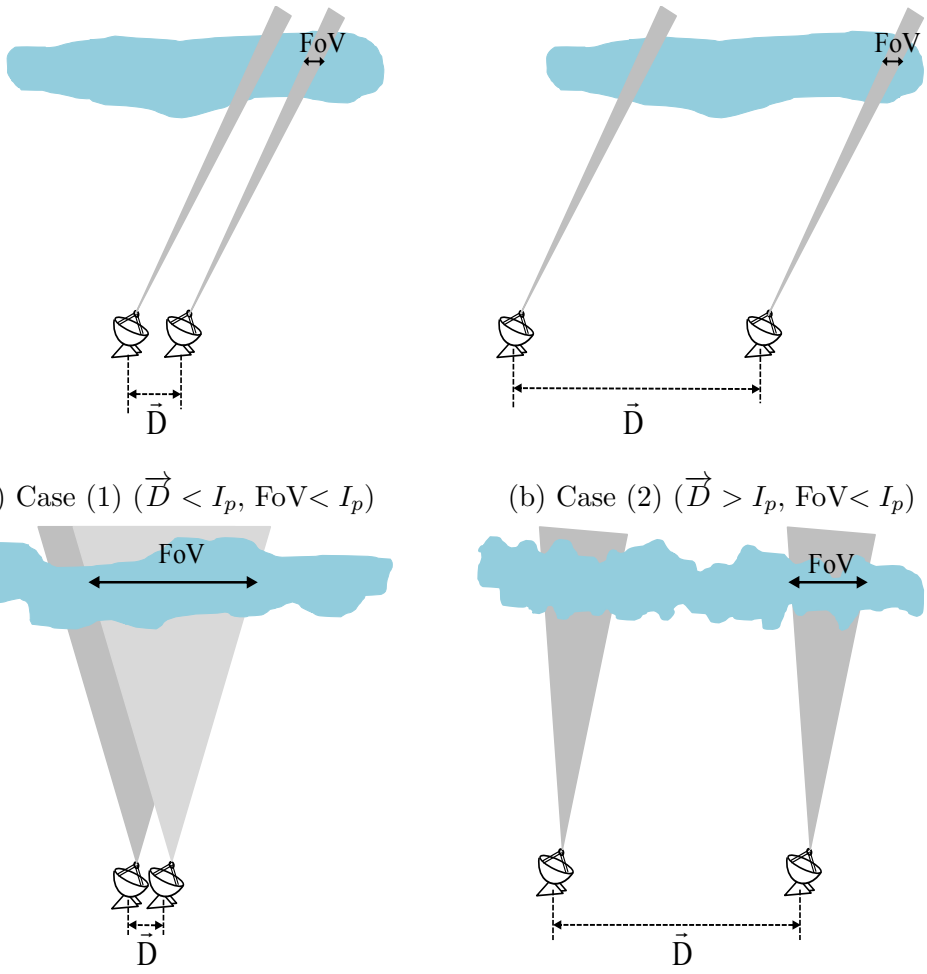

(a) Case (1) ($\overrightarrow{D} < I_p$, FoV$< I_p$)

(b) Case (2) ($\overrightarrow{D} > I_p$, FoV$< I_p$)

(c) Case (3) ($\overrightarrow{D} < I_p$, FoV$> I_p$)

(d) Case (4) ($\overrightarrow{D} > I_p$, FoV$> I_p$)

Figure 2.2: A graphical representation for classification of an interferometer, for the ionospheric effects, as a function of baseline length ($\overrightarrow{D}$) and antenna/tile FoV and isoplanatic patch size (I_p)

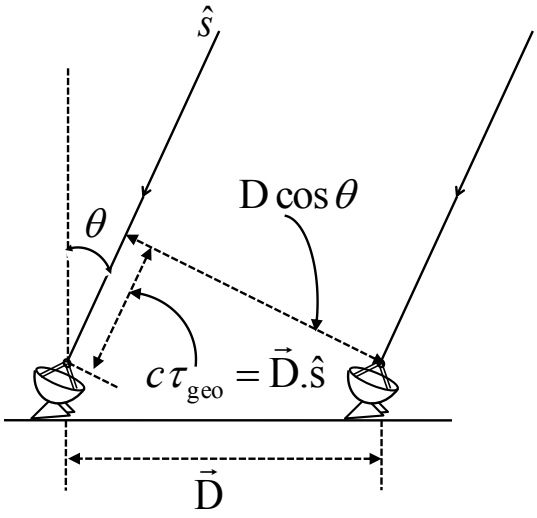

Figure 2.3: A basic two-element interferometer

quency, τ_{geo} (s) is the geometrical delay, λ_0 (m) is the observing wavelength, D (m) is the interferometer baseline length, θ (rad) is the arrival angle for the source.

Due to the ionosphere, the position of the source, indicated by direction $\hat{s}$ and arrival angle θ (refer Figure 2.3), is observed to be shifted. The expression for the change in phase of the interferometer can now be given as follows

$$d\phi = \frac{2\pi D \cos\theta}{\lambda_0} d\theta \tag{2.14}$$

where, $d\phi$ is the change in the phase (rad), $d\theta$ is the change in the arrival angle (rad)

The change in position of the source can be accounted in terms of the change in arrival angle of the source, $d\theta$. The change in arrival angle, $d\theta$, is proportional to the ionospheric gradient over the baseline (D), which is the ratio of the first order ionospheric delay and the baseline length. The value of first order phase ionospheric delay (ΔI_1, equation (2.12)) can be substituted for $d\theta$, by using the first order ionospheric refractive index from equations (2.1) and (2.6). since we are evaluating the change in phase, the negative sign for the first order phase refractive index is ignored. The change in arrival angle can be given as follows

$$d\theta = \frac{\nabla \Delta I_1}{D} = \frac{e^2}{8\pi^2 m_e \varepsilon_0 f_0^2} \frac{\nabla \int N_e}{D} \tag{2.15}$$

where ΔI_1 (m) is the first order ionospheric delay, the operator ∇ indicates the differential ionospheric effects seen by the interferometer elements, e is the charge of the electron, m_e is the mass of the electron, ε_0 is the permittivity of vacuum, f_0 is the observing frequency, $\int N_e$ (electrons/m^3) is the integrated electron density.

Approximating the expression given in equation (2.14) for a source at zenith, $\cos\theta$ =1. Substituting the value of $d\theta$ from equation (2.15) in equation (2.14), we get,

$$d\phi = \frac{e^2}{4\pi m_e \varepsilon_0 f_0 c} \nabla \int N_e \tag{2.16}$$

Equation (2.16) can be rewritten by substituting for the classical electron radius r_e, $r_e = \dfrac{e^2}{4\pi m_e \varepsilon_0 c^2} = 2.817\,940\,326\,7 \times 10^{-15}$ m, and $c/f_0 = \lambda_0$, c (m s^{-1}) is the speed of light. Further the integrated electron density can be written as a function of $STEC$ (electrons/m^2), $\int N_e = STEC \times 10^{-16}$, as follows

$$d\phi = r_e \, \lambda_0 \, \nabla STEC \times 10^{-16} \tag{2.17}$$

For MWA, with observing frequency, f_0=150 MHz (λ_0 =2 m), and a maximum baseline length of ∼3000 m. The maximum observed change in the arrival angle, $d\theta$, for the MWA is found to be $\pm 1 \times 10^{-4}$ rad (Arora et al., 2015). The change of phase, $d\phi$, can be computed from equation (2.14), which comes to ∼1 rad. The maximum allowable change in ionosphere, $\nabla STEC$, can be now computed from equation (2.17), which equates to ∼0.02 TECU.

The future upgrades to MWA and the low frequency SKA would have larger baseline lengths, hence the expected change in the ionosphere, $\nabla STEC$, would be ∼0.02 TECU or higher.

The GNSS data, has the very precise phase measurements, as one of the observables. The precision of the GPS phase observables is about 0.003 m, which translates to ∼0.03 TECU. This research work makes use of GPS and GLONASS observables for the estimation of the ionosphere, which includes the precise phase measurements.

2.4 The GNSS Observables and the Ionospheric Delay

The GNSS satellite systems, namely the GPS and GLONASS, used in this study, transmit on GHz frequencies. The GNSS satellites transmit on atleast two carrier frequencies (some recent upgrades to GPS satellite have an additional third transmission frequency). The ionospheric delay is dispersive, refer equation (2.3) (ionosphere refractive index) and equation (2.12) (ionospheric delay), it can hence be parameterised based on frequency or the wavelength of GNSS signal. The multi-frequency transmission by GNSS systems makes them a useful tool for monitoring the ionosphere.

In this work we estimate the first order ionospheric delay from the GNSS observables. In GNSS terminology, the total number of cycles between the receiver and the satellite, affected by errors, are referred to as *phase observables*. The group delays, which are the refracted ranges between the receiver and satellite, are commonly referred to as the *code observables*. We recall equation (2.12) for ionospheric phase delay (for GNSS phase observables), ΔI_1) and ionospheric group delay, $\Delta I_{g,1}$ (for GNSS code observables), given as follows

$$\begin{aligned} \Delta I_1 &= -\frac{40.3}{f_j}\int_r^s N_e = -\frac{40.3\ STEC}{f_j^2} = -i^s_{r,j} \\ \Delta I_{g,1} &= \frac{40.3}{f_j}\int_r^s N_e = \frac{40.3\ STEC}{f_j^2} = i^s_{r,j} \end{aligned} \tag{2.18}$$

where, $i^s_{r,j}$ is the ionospheric delay as seen be receiver r towards satellite s on jth GNSS frequency, $i^s_{r,j}$ will be the notation used to represent the slant ionospheric delay ($STEC$) in GPS/GLONASS observation model.

Even though the GNSS satellites aim to serve the common prime purpose of providing navigation solutions, different GNSS constellations sometimes differ in the technical functionality. The GLONASS system uses Frequency Division Multiple Access (FDMA) for transmission (as opposed to the Coarse Division Multiple Access for GPS), hence can have different frequencies for different satellites, also known as channels, which will be discussed in detail in the later sections of this chapter. We start in the next section with the most widely used GNSS sys-

tem, the GPS. The basic GPS observation equations are discussed in the following section.

2.5 The GPS Observables

The signals transmitted by the GPS satellites form the observables, namely the phase (of the carrier frequency) and code (digital code) measurements. A phase measurement is the number of cycles at the corresponding carrier frequency between the satellite and the receiver. The phase delay between the receiver and the satellite is obtained by multiplying the number of phase cycles with the wavelength of the corresponding carrier. The phase measurements are biased by an unknown number of phase cycles, in addition to other errors. When a GPS receiver is switched on or tracks a newly risen satellite, it cannot determine the total number of complete cycles between the receiver and the satellite. Hence the initial number of complete cycles remains ambiguous, known as phase ambiguity bias.

The GPS code measurements have two types of code observables, namely the C/A-code (Coarse/Acquisition code, modulated only on the L1 carrier, denoted as C1) and P-code (Precise code, modulated on both L1 and L2 carriers, denoted as P1 and P2, respectively). The code modulation is different for each GPS satellite, with code signals sometimes also referred to as PRN (Pseudo Random Noise). The C/A-code measurement is less precise than the P-code, since the bit rate of C/A-code is 10 times lower than P-code (Langley, 1993). The GPS receiver generates replicas of the transmitted code signals. By comparing the code signal to its replica, the signal travel time is obtained (Hofmann-Wellenhof et al., 1993). For a more detailed description, one can refer to Hofmann-Wellenhof et al. (1993), Langley (1993) and El-Rabbany (2006). This work uses two GPS carrier frequencies, namely $f_1 = 1575.42$ MHz (for carrier L1) and $f_2 = 1227.60$ MHz (for L2).

2.5.1 The GPS Observation Equation

The terms contributing to the GPS phase and code observables, is depicted in Figure 2.4, can be given as follows (Teunissen & Kleusberg, 1998):

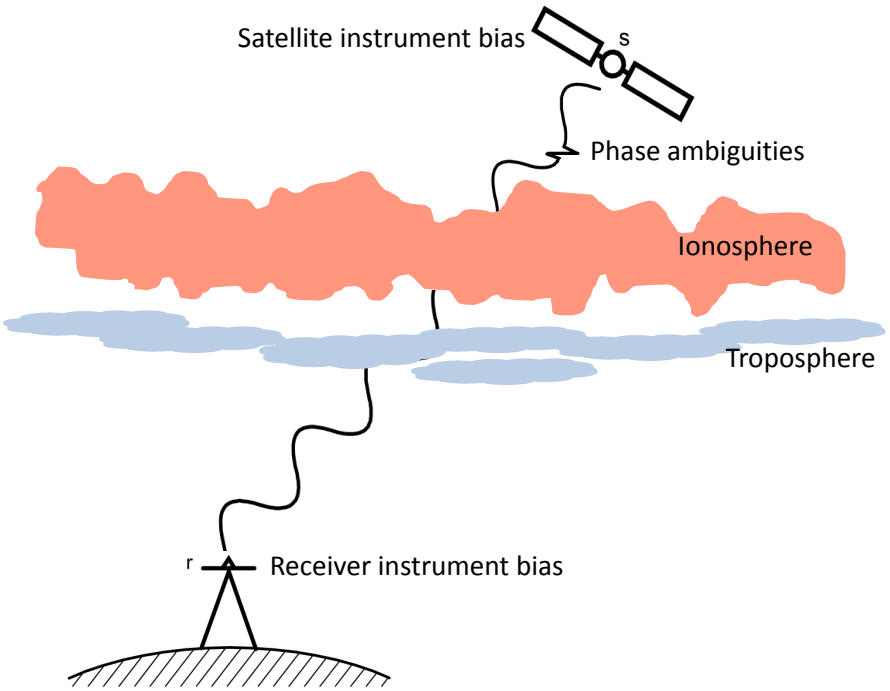

Figure 2.4: A schematic representation of errors in GPS observables

$$E(\Phi^s_{r,j}) = \overline{\rho}^s_r - \iota^s_{r,j} + c \cdot (\delta_{r,j} - \delta^s_{,j}) + \lambda_j M^s_{r,j}, \tag{2.19}$$

$$E(P^s_{r,j}) = \overline{\rho}^s_r + \iota^s_{r,j} + c \cdot (d_{r,j} - d^s_{,j}). \tag{2.20}$$

where Φ and P are GPS phase and code observables, respectively, subscripts s, r, and j indicate satellite, receiver and GPS frequency number, respectively, $\delta_{r,j}, \delta^s_{,j}$, $d_{r,j}, d^s_{,j}$ are the phase and code instrumental delays, $\overline{\rho}^s_r$ includes the '*Geometry*' parameters, namely, the geometric range, ρ^s_r, the tropospheric delay, τ^s_r, and the clock delay $c{\cdot}dt^s_r$, λ_j is the wavelength at frequency jth GPS frequency. $M^s_{r,j}$ are the non-integer ambiguities on the phase observables which contain the unknown integer ambiguities, $N^s_{r,j}$, and the non-integer initial phase offsets for the receiver ($\phi_{r,j}(t_0)$) and satellite ($\phi^s_{,j}(t_0)$), i.e.,

$$M^s_{r,j} = N^s_{r,j} + \phi_{r,j}(t_0) - \phi^s_{,j}(t_0). \tag{2.21}$$

The phase ambiguities remain constant for any given receiver, frequency, and continuous satellite arc unless there is a loss of signal lock.

Since the effect of the ionospheric delay is a function of frequency, a frequency difference of phase and code observables can be formed which retains the ionospheric delay while the geometry-related parameters are eliminated. Along with the ionospheric delay (ι^s_r), the phase and code instrumental delays ($\delta_{r,j}, \delta^s_{,j}, \ d_{r,j}, d^s_{,j}$) and phase ambiguities ($\lambda_j M^s_{r,j}$) remain. The frequency-difference phase and code observation equations for dual frequency GPS observables, formed using equations (2.19) and (2.20), are given as follows:

$$E(\Phi^s_{r,21}) = \Phi^s_{r,1} - \Phi^s_{r,2} \ = \ -\iota^s_{r,21} + \mathrm{C}^s_r, \tag{2.22}$$

$$E(P^s_{r,21}) = P^s_{r,1} - P^s_{r,2} \ = \ \iota^s_{r,21} + c \cdot (d_{r,21} - d^s_{,21}). \tag{2.23}$$

Here, $d^s_{,21}$ and $d_{r,21}$ are the inter-frequency code instrumental bias for the satellite and the receiver. The inter-frequency code instrumental bias are also referred to as Differential Code Bias (DCB). The constant phase term C^s_r is given as follows:

The observations formed under equations (2.22) and (2.23) are refereed to as Geometry-Free (GF) combination of observables.

$$\mathrm{C}^s_r = \left[c \cdot (\delta_{r,21} - \delta^s_{,21}) + \left(\lambda_1 M^s_{r,1} - \lambda_2 M^s_{r,2}\right)\right]. \tag{2.24}$$

2.6 The GLONASS Observables

The GLONASS satellites transmits data using a 15-channel FDMA technique. The frequency for each channel is given by $\mathrm{L1}_n = \mathrm{L1}_0 + n \times (9/16)$ MHz and $\mathrm{L2}_n = \mathrm{L2}_0 + n \times (7/16)$ MHz, where n is the GLONASS channel number, $n = -7, \cdots, 0, \cdots, 6$. The GLONASS channel number for each satellite can be obtained from the GLONASS broadcast ephemerides file.

The GPS and GLONASS systems transmit in different reference times. The GPS satellites have an atomic clock which was synchronised to UTC (Coordinated Universal Time) at the time of its launch (1980). Unlike the principal Universal Time (UT1), the UTC time does not account for the Earth's rotation, hence has to be corrected timely by adding leap seconds. The leap second corrections, though cannot be corrected directly in GPS satellite clocks, but have to be manually accounted for, by adding leap seconds to GPS time from the date of its launch.

Since the GPS time began, on January 1, 1980, 17 seconds have been added to GPS time to synchronise it to UT1, the most recent one was on June 30, 2015 at 23:59:60 UTC. The GLONASS system accounts for leap seconds and is in sync with UT1. For an integrated GPS and GLONASS system, a common time system can be realised, and the data can be corrected accordingly. The GLONASS orbit data is processed by the International GNSS Service (IGS) and made publicly available with a common time system, the GPS time. For the observation data, recorded as a mixed (GPS+GLONASS) file, the header section of the observation data specifies the time system used by the receiver clock. The observation data file generally uses GPS time. In this case, the GLONASS pseudo range can be corrected as suggested in the observation file format description[1], ($P^{Rs}_{r,j} = P^{Rs}_{r,j}$ - $c \times$ leap_seconds, where P is the GLONASS pseudo-range observable, subscripts and superscripts r, j, and Rs indicate receiver, frequency and GLONASS satellite, respectively, c is the speed of light). However, if the GF combination is used, as in our work, the pseudo range correction is compensated and not required.

2.6.1 GPS and GLONASS Observation Model

The observation equations for the GF, GPS observation model, are given in equations (2.22) and (2.23). The combined GPS and GLONASS, GF observation model, for estimation of ionospheric delay can be given as follows

$$E(\Phi^{Gs}_{r,21}) = \Phi^{Gs}_{r,1} - \Phi^{Gs}_{r,2} = -\iota^{Gs}_{r,21} + \mathrm{C}^{Gs}_{r}, \tag{2.25}$$

$$E(P^{Gs}_{r,21}) = P^{Gs}_{r,1} - P^{Gs}_{r,2} = \iota^{Gs}_{r,21} + c \cdot (d_{r,21} - d^{Gs}_{,21}). \tag{2.26}$$

$$E(\Phi^{Rs}_{r,21}) = \Phi^{Rs}_{r,1} - \Phi^{Rs}_{r,2} = -\frac{\mu^{R}_{21}}{\mu_{21}}\iota^{s}_{r} + \mathrm{C}^{Rs}_{r}, \tag{2.27}$$

$$E(P^{Rs}_{r,21}) = P^{Rs}_{r,1} - P^{Rs}_{r,2} = \frac{\mu^{R}_{21}}{\mu_{21}}\iota^{s}_{r} + c \cdot d^{Rs}_{r,21}. \tag{2.28}$$

where $E(\cdot)$ is the expectation operator, Φ is the phase observable, P is the code observable, subscript $_r$ indicates receiver, $_1$, $_2$ and $_{21}$ indicates frequencies at L1, L2 and L4, respectively, superscripts ^{Gs}, ^{Rs} indicate GPS and GLONASS satellites, respectively, $d_{r,21}$ and $d^{Gs}_{,21}$ are the GPS, receiver and satellite, inter-frequency code instrumental biases also known as DCB, μ_{21} is the GPS frequency

[1]Receiver INdependent EXchange (RINEX) format (Gurtner, 1994)

coefficient given as, $\mu_{21} = \mu_1 - \mu_2$ and $\mu_1 = \frac{1}{f_1^2}$, $\mu_2 = \frac{1}{f_2^2}$, f_1 and f_2 are GPS frequencies at L1 and L2. Similarly, the GLONASS frequency coefficient is given by μ_{21}^R.

2.7 Summary

In this chapter, we presented the physics of the ionosphere, along with equations for ionospheric refractive index and the ionospheric delay. The ionospheric effects on low frequency interferometers were presented and discussed, the equation to determine the threshold for the ionospheric effects were derived for the interferometers, and evaluated for the MWA. Further, the GPS and GLONASS observation models for modeling the ionosphere were presented. The following chapters, Chapters 3 and 4, will use the formalism presented here to model the ionosphere using GPS and GLONASS observations, and draw comparisons with the MWA observed ionospheric effects.

3

Comparison of First Order Ionospheric Effects Obtained Using Single-Station GPS Models and MWA Observations

Adapted from:

Ionospheric modelling using GPS to calibrate the MWA. 1: Comparison of first order ionospheric effects between GPS models and MWA observations B. S. Arora, J. Morgan, S. M. Ord, S. J. Tingay, N. Hurley-Walker et. al., 2015, Publications of the Astronomical Society of Australia, Volume , 32, e029 doi:10.1017/pasa.2015.29.

3.1 Introduction

In this chapter, we present the methodology to model the ionosphere using Global Positioning System (GPS) observations. The data from Geoscience Australia (GA) GPS stations near the Murchison Radio-astronomy observatory (MRO), located at Murchison (MRO1), Mount Magnet (MTMA), Yaragadee (YAR3) and Wiluna (WILU), were used for ionospheric modelling. A single-station approach is adopted, data from a single GPS station is used for ionospheric modelling using an assumption that ionosphere is concentrated at a single layer at a fixed height above the Earth's surface. The estimated ionospheric parameter obtained from GPS observations is compared with the ones derived from Murchison Widefield array (MWA) observations.

3.1.1 GPS Studies of the Ionosphere

The Global Positioning System (GPS) has widely been used in civilian applications for precise geodetic positioning and navigation. For precise positioning applications using GPS, new control points can be established by applying constraints using positions from the established control points. Global GPS data processing centres like the International GNSS (Global Navigation Satellite System) Service (IGS), with international multi-agency members, provide support for such global geodetic activities. In addition to the positions of the global network of GPS/GNSS stations, a number of products such as precise satellite ephemerides, satellite clock parameters, Earth rotation parameters, global ionosphere maps, and zenith tropospheric path delays are routinely generated (Beutler et al., 1999). We recall from Chapter 1 that the global ionospheric maps are generated by various IGS analysis centres, namely, the Center for Orbit Determination in Europe (CODE), the Astronomical Institute at the University of Bern (AIUB), Switzerland (Rothacher et al., 1997), however they have a coarse resolution. The global network of GPS/GNSS stations which are used to generate global ionospheric maps by CODE are presented in Figure 3.6 (marked by white dots). It can be noted that, due to the global nature of solutions, the density of the stations is sparse, including from near MRO, Western Australia.

Ros et al. (2000) evaluated the quality of GPS-based ionosphere corrections for Very Long Baseline Interferometry (VLBI) at 8.4 and 2.3 GHz. In his study, Ros et al. (2000) corrected the ionosphere for continental (∼200 to ∼700 km) and inter-continental (∼7800 to ∼8300 km) baseline lengths and concluded that GPS maps of TEC can usefully contribute to VLBI astrometric analysis. Erickson et al. (2001) made use of the ionospheric corrections generated from an experimental set-up of four GPS receivers at the Very Large Array (VLA) site to correct for the ionospheric effect. Erickson et al. (2001) found that large scale structures (>1000 km) could be resolved observing at frequencies of 322 and 333 MHz, whereas small scale fluctuations (<100 km) could not be seen using a global model; it was noted that global ionosphere models perform averaging over the ionosphere and hence lose their capacity to monitor small scale ionospheric changes. Erickson et al. (2001) argues that a dense GPS network is required to correct for small scale fluctuations in the ionosphere.

3.1.2 MRO Studies of the Ionosphere

GPS-based estimation of the ionosphere has also been carried out by Herne et al. (2013). High-fidelity GPS systems were specially deployed by the U.S. Air Force for measurement of ionospheric TEC and scintillation indices at the location of the MRO and Australian Space Academy campus (Meckering, Western Australia). Two periods of time corresponding to low (2008-2009) and high (2012-2013) ionospheric activity were studied. During 2008-2009, the F10.7[1] Index varied between 65 to 82 ($10^{-22} W m^{-2} Hz^{-1}$), the monthly variation was found to be insignificant for most of the period. The Ap[2] index reached a maximum of 35 during this period. However, during high solar activity (2012-2013), F10.7 led between 85 to 190, the monthly variation was significant throughout the period. Ap index reached a maximum of 90. The ionosphere at the MRO was expected to exhibit very low levels of scintillation (Kennewell et al., 2005). For Kp[3]=9, scintillation at MRO reached about 0.2. In Herne et al. (2013), during 2012-2013, scintillation was found to reached a maximum of about 0.3.

The MWA has recently operations in 2013, and ionospheric effects are routinely detected. For example, observations have revealed variations in the Rotation Measure of polarised point sources and the diffuse galactic background (E. Lenc, private communication). Loi et al. (2015c) demonstrate the utility of the MWA as a powerful imager for studying high-altitude irregularities, revealing a population of field-aligned density ducts that appear regularly over the observatory. The spatial distributions of celestial source refractive offsets over the field of view, combined with a novel parallax technique for altitude measurement, enable the 3D characterisation of ionospheric structures at high temporal cadence. Travelling ionospheric disturbances (TIDs), sinusoidal perturbations with wavelengths of 100-1000 km and periods of several tens of minutes to an hour, are also often observed in MWA data. A technique for the spatio-temporal power spectrum analysis of ionospheric gradients, presented by Loi et al. (2015d), enables characteristic wavelengths and periods of fluctuation to be measured. A quantitative study of the statistical properties of ionosphere-induced position and amplitude variations of sources in MWA images (Loi et al., 2015b) has yielded information about characteristic density gradients and the diffractive scale in the ionosphere. This illustrates the capability of the MWA to probe ionospheric structure in great

[1]Noise level generated by Sun at 10.7 cm (2800 MHz)

[2]Daily average level for geomagnetic activity

[3]Quasi-logarithmic index of geomagnetic activity relative to an assumed quiet day

detail.

3.1.3 The Need for Better Resolution

All previous attempts at GPS-based ionosphere calibration for radio astronomy made use of ionosphere information from TEC maps which have a temporal resolution of 2 hours. Ionospheric structures such as TIDs have a period of several tens of minutes, hence it is important to generate ionospheric information with higher resolution. We present here a method where publicly available data from GPS stations are used to generate location-specific ionosphere models at 10 minutes intervals. This requires the calibration of GPS receiver/transmitter instrumental biases in order to accurately model the ionosphere, also known as Differential Code Bias (DCB).

The GPS data from Geoscience Australia (GA) GNSS network, located in the vicinity of MRO were used, refer Figure 3.3. The GA GNSS stations located at Murchison (MRO1), Mount Magnet (MTMA), Yaragadee (YAR3), and Wiluna (WILU) were used for modelling the ionosphere.

We perform a simultaneous fit for both GPS DCBs and ionospheric parameters. While the BERNESE software provides the GPS DCBs and ionospheric parameters (Dach, R. and others, 2007), our work allows much higher time resolution of the ionospheric parameters than is commonly obtained, while simultaneously solving for the DCBs.

This chapter is organised as follows, Section 3.2 presents, in detail, the methodology for estimation of ionospheric coefficients using GPS observables. The estimated parameters, namely the $VTEC$, can be checked for its integrity by drawing comparisons with the GPS global maps generated by CODE analysis center. Section 3.3 presents the details of the GPS station which were used in this study. Further, the methodology used for GNSS data integrity is presented in Section 3.3.1. The GNSS data can sometimes contain uncertainties in the observables, which need to be detected and corrected for, before the estimation process. Section 3.3.2 discusses in detail the approach adopted by CODE analysis center to generate global ionosphere maps. The MWA observations are used to derive information about the ionosphere, Section 3.4 presents the procedure to model the ionosphere seen by the MWA in the form of position shifts. The results are presented and discussed in Section 3.5. Results from the IGS analysis centre, CODE, serve as reference to validate our $VTEC$ results. In particular, we compare our

estimated receiver DCBs, the inter-frequency biases on code observables, with those determined by the BERNESE processing software employed by CODE. The ionosphere observed by the MWA and the GPS are analysed and the agreement discussed. Finally, the summary of the chapter is presented in Section 3.6.

3.2 Estimation of the Ionosphere Using GPS Observations

The GPS satellite constellation and technical overview are discussed in detail in Chapters 1 and 2, respectively. The GPS satellite constellation consists of ∼32 satellites, the GPS satellites have a global coverage and at any given time 4 to 10 GPS satellites are visible. We recall that all the GPS satellites transmit at least two frequencies. In this research work, we make use of two GPS carrier frequencies, namely $f_1 = 1575.42$ MHz (for carrier $L1$) and $f_2 = 1227.60$ MHz (for $L2$). On each of the frequencies, two GPS observables, carrier *phase* (denoted by $L1$ and $L2$) and *code* (denoted as $C1$ for Coarse-Acquisition code, $P1$ and $P2$ for Precise code), refer Chapter 2 for detailed description of the observables.

3.2.1 Ionospheric Modelling Using GPS

We recall the GPS phase and code observables given in Chapter 2, Section 2.5.1, by equations (2.22) and (2.23)

$$E(\Phi^s_{r,21}) = \Phi^s_{r,1} - \Phi^s_{r,2} \;=\; -\iota^s_{r,21} + \mathrm{C}^s_r,$$

$$E(P^s_{r,21}) = P^s_{r,1} - P^s_{r,2} \;=\; \iota^s_{r,21} + c \cdot (d_{r,21} - d^s_{,21}).$$

where $E(\cdot)$ is the expectation operator, Φ is the phase observable, P is the code observable, subscripts r and s indicate receiver and satellite, respectively, $_1$, $_2$ and $_{21}$ indicates GNSS frequency/frequency combinations corresponding to phase (or code) observables, $L1$ (or $C1$), $L2$ (or $P2$) and $L4$ (or $P4$), respectively, $\iota^s_{r,21}$ is the slant ionospheric delay, $d^s_{,21}$ and $d_{r,21}$ are the inter-frequency biases for the satellite and the receiver on code observables, and C^s_r is the constant phase term consisting of non integer ambiguities and instrumental biases on phase observables.

The slant ionospheric delay, $\iota^s_{r,j}$, j indicates the frequency number, is related

to the Slant Total Electron Content ($STEC$), refer Chapter 2, equation (2.18), as follows

$$\iota^s_{r,j} \;=\; \frac{40.3\ STEC}{f_j^2}. \tag{3.1}$$

As shown in Figure 3.1, the $STEC$ can be mapped to the Vertical Total Electron Content, $VTEC$, using the obliquity factor F^s, also known as the ionosphere mapping function. F^s is a function of zenith angle at the Ionosphere Pierce Point (IPP), z', given as follows:

$$\left.\begin{aligned} STEC &= VTEC \cdot F^s \\ F^s &= \frac{1}{\cos(z')} = \frac{1}{\sqrt{1-\sin^2 z'}} \\ \sin z' &= \frac{R_e}{R_e + H_{ion}} \sin(z) \end{aligned}\right\} \tag{3.2}$$

where z' is the zenith angle at the IPP, R_e is the mean radius of the Earth, (6371 km) and assuming a spherical Earth, H_{ion} is the height at the sub-ionospheric point, assumed to be 450 km, and z is the zenith angle of the satellite as seen by the receiver. The geometry of the model is illustrated in Figure 3.1. This study aims to compare and analyse ionosphere gradients, the height, H_{ion}, of 450 km was chosen in order to compare the $VTEC$ with CODE analysis center published values.

We can now map the GPS observables to the $VTEC$ as follows

$$\left.\begin{aligned} E\left(\frac{\Phi^s_{r,21}}{40.3\ \mu_{21}}\right) &= -F^s\ VTEC + \frac{\mathrm{C}^s_r}{40.3\ \mu_{21}} \\ E\left(\frac{P^s_{r,21}}{40.3\ \mu_{21}}\right) &= F^s\ VTEC + \frac{c\cdot(d_{r,21} - d^s_{,21})}{40.3\ \mu_{21}} \end{aligned}\right\} \tag{3.3}$$

Here $c\cdot(d_{r,21})$ and $c\cdot(d^s_{,21})$ are commonly known as DCB, for the receiver and the satellite, respectively, where

$$\left.\begin{array}{lll} \mu_{21} & = & \mu_1 - \mu_2 \\ & \text{and} & \\ \mu_1 = \dfrac{1}{f_1^2} & & \mu_2 = \dfrac{1}{f_2^2} \end{array}\right\} \tag{3.4}$$

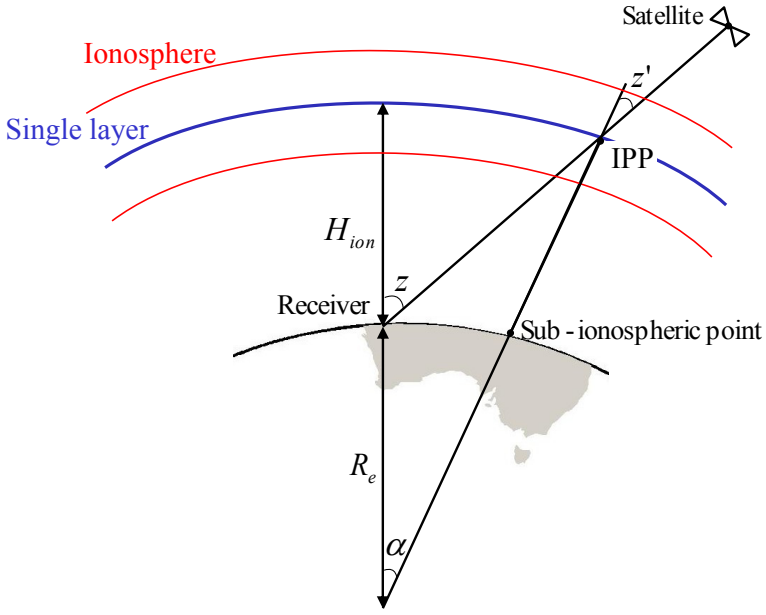

Figure 3.1: Ionosphere single layer model representation.

3.2.2 Ionosphere Model Coefficients

The $VTEC$ can be modelled by assuming that the ionosphere is concentrated at a single layer at height H_{ion} as illustrated in Figure 3.1 (Schaer, 1999; Wang et al., 2014). The intersection of the GPS receiver-satellite line-of-sight with the ionospheric layer is known as the Ionospheric Pierce Point (IPP). The slant TEC is mapped to the vertical TEC by an obliquity factor (equation (3.2)), which is a function of the zenith angle at the IPP, z'. $VTEC$ is modelled as a function of geomagnetic latitude, φ_g, and Sun fixed longitude, s, using the

following polynomial function (Wang et al., 2014)

$$\begin{aligned} VTEC(\varphi_g, s) &= VTEC_0 + (\varphi_g - \varphi_{g_0})f'\varphi + (s - s_0)f's + \\ &+(\varphi_g - \varphi_{g_0})^2 f''\varphi_g\varphi_g + (s - s_0)^2 f''ss \\ &+(\varphi_g - \varphi_{g_0})(s - s_0)f''\varphi_g s. \end{aligned} \tag{3.5}$$

The activity of the ionosphere varies with the time of the day. For modelling the ionosphere it is better to consider its behaviour constant over a certain period of time, for which the argument of the time of the day is adjusted with the argument of longitude. This is also referred to as Sun fixed reference frame, and the resultant longitude as Sun fixed longitude. The Sun fixed longitude, s, is related to the local solar time (LT) as $s = \lambda_g + LT - \pi$, where λ_g is the geomagnetic longitude at IPP, LT is in radians, $VTEC_0$ is the $VTEC$ at the receiver location and $f's,\ f'\varphi_g,\ f''ss,\ f''\varphi_g\varphi_g,\ f''\varphi_g s$ are the first and second order derivatives of $VTEC$ along the Sun fixed longitude and latitude, respectively.

The single layer ionospheric model is a computation efficient model to estimate local ionospheric gradients at the zenith. However, the ionospheric features, for example those along the magnetic field lines, cannot be resolved using this model.

3.2.3 VTEC Determination Through Kalman Filtering

The GPS model to estimate unknowns can be formed from equation (2.23). In our method, the DCBs for receiver and satellite are estimated as a single parameter, $\widetilde{DCB^s} = c \cdot (d_{r,21} - d^s_{,21})$, since the model presented in equation (3.3) is rank deficient. The parameters, namely the receiver and the satellite DCBs, cannot be separated from each other, hence cannot be independently estimated. A minimum set of parameters, known as the $\mathcal{S}$-basis, are chosen which can be lumped with the remaining parameters in order to overcome the rank deficiency in the underlying model (Teunissen, 1984). For m satellites seen by receiver r, a weighted least square model is formed using equations (2.23) and (3.5), given as follows

$$\left.\begin{aligned} E(\boldsymbol{y_i}) &= \mathbf{A_i}\ \boldsymbol{x_i} \\ D(\boldsymbol{y_i}) &= \mathbf{Q_{yi}} \\ \boldsymbol{x_i} &= \left[\mathrm{C}_r^s\ \widetilde{DCB^s}\ VTEC_0\ f'\varphi_g\ f's\ f''\varphi_g\varphi_g\ f''ss\ f''\varphi_g s\right]^T \end{aligned}\right\} \tag{3.6}$$

where $E(\cdot)$ and $D(\cdot)$ denote the expectation and dispersion operators, $\boldsymbol{y_i}$ denotes a vector of observables of size $[2m \times 1]$ at time stamp i, $\mathbf{A_i}$ is the design matrix of size $[2m \times (2m+6)]$, the unknowns given by $\boldsymbol{x_i}$ are of size $[(2m+6) \times 1]$, and $\mathbf{Q_{yi}}$ is the stochastic model for observables in $\boldsymbol{y_i}$ given as

$$\mathbf{Q_{yi}} = \left(\frac{1}{40.3\ \mu_{21}}\right)^2 \frac{\sigma_0^2}{\sin^2(\boldsymbol{el})}, \tag{3.7}$$

$\boldsymbol{el}$ is the vector of elevation angles of all the visible satellites, and σ_0 is the measurement noise of the observables.

To solve the above model, a cut-off for the satellite zenith angle of 70° was chosen. The model given in equation (3.6) cannot be solved in a single epoch. An ionosphere refreshing interval of 20 epochs (1 epoch = 30 seconds) is chosen over which the ionosphere is assumed to remain constant. The phase bias term C_r^s constitutes an integer phase ambiguity and non-integer receiver and satellite phase bias terms. The integer phase ambiguities remain constant for a single continuous satellite arc unless there is a loss of signal lock, hence C_r^s is assumed to remain constant for a continuous satellite arc. The GPS observables were free of multipath and cycle-slips. The code bias terms, $\widetilde{DCB^s}$, are assumed to remain constant over a period of 24 hours for any satellite.

With the above considerations, the unknowns given in equation (3.6) are estimated using the Kalman Filter approach (Kalman, 1960; Kailath, 1981; Grewal & Andrews, 2011). In this work, Kalman filter is used in data assimilation mode. A Kalman filter can be described as a three step procedure, with initialisation, prediction, and measurement update executed at different time steps t, $t = 1, \cdots, t_{max}$. The implementation of the Kalman filter is shown in Figure 3.2, where, $\hat{\boldsymbol{x}}_{\mathbf{0|0}}, \mathbf{A}_{\mathbf{0|0}}^{\mathbf{T}}, \mathbf{Q_y}$, and $\boldsymbol{y}_{\mathbf{0|0}}$ indicate the unknowns, the design matrix, the Variance Covariance (VC) matrix of the measurements, and the measurements, respectively. $\mathbf{\Phi_{t|t-1}}$ is the transition matrix which relates the unknowns at the current $\hat{\boldsymbol{x}}_{\boldsymbol{t|t-1}}$ and previous $\hat{\boldsymbol{x}}_{\boldsymbol{t-1|t-1}}$ time step with a system noise given by the VC matrix. $\mathbf{S_t}$, $\mathbf{v_t}$ are the predicted residuals and $\mathbf{Q_{v_t}}$ its VC matrix. $\mathbf{K_t}$ is the

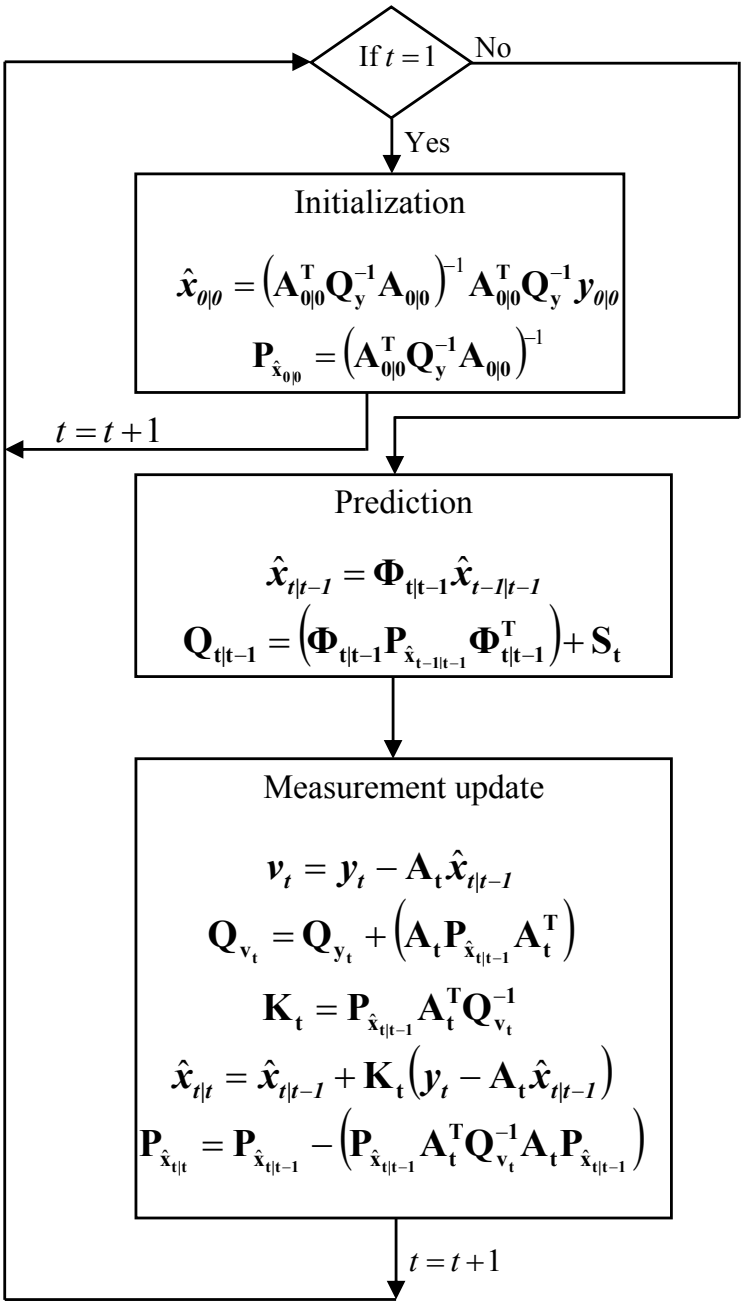

Figure 3.2: Flow chart describing the implementation of a Kalman Filter.

Kalman gain which is used to compute the measurement update given by $\hat{\boldsymbol{x}}_{t|t}$ and its VC matrix $\mathbf{P}_{\hat{\mathbf{x}}_{t|t}}$.

3.3 GPS Data Preparation

The data from the three Geoscience Australia (GA) GPS/GNSS stations nearest to the MRO were used for this analysis, namely, MRO1 (Murchison), MTMA (Mount Magnet), YAR3 (Yarragadee), and WILU (Wiluna) (Figure 3.3). A description of the selected GPS/GNSS stations is given in Table 3.1. The data for the selected GA GNSS network were downloaded from the GA archive[4] for 3^{rd}, 4^{th}, 6^{th} and 16^{th} March 2014 corresponding to Day of Year (DOY) 062, 063, 065 and 075, respectively. The four days chosen for this analysis were the first four nights of GLEAM observations for which suitable MWA data was available. Also, by choosing data from the year 2014, data from the recently active GPS receiver MRO1 could be included. Only YAR3 is included in CODE analysis, illustrating why our analysis is required to establish dense GPS networks near the MWA. Table 3.2 presents the summary of ionospheric weather on the selected four days, the parameters, F10.7 solar flux, and Planetary Kp indices are presented. The data presented in Table 3.2 indicate quiet ionospheric conditions, which are ideal for testing the methods described in this chapter.

The GPS/GNSS data can sometimes be affected by discontinuities, which can bias the solutions significantly, if not addressed. The following section presents the methodology adopted to correctly identify and repair the discontinuities in GNSS observables.

3.3.1 GNSS Data Pre-Processing

In GNSS data pre-processing, discontinuities in the phase and code observables are identified and repaired (Lichtenegger & Hofmann-Wellenhof, 1990; Remondi, 1985, among others). The uncertainties in the GNSS observables, namely, phase cycle-slips and jumps, and multi-path.

[4] `ftp://ftp.ga.gov.au/geodesy-outgoing/gnss/data/daily/`*yyyy*/*yyddd*/*xxxxddd*0.*yy*d.Z
The abbreviations *yyyy* and *yy* are the four and two digit year, *ddd* is the DOY, *xxxx* represents the four character GPS station id, *d* stands for Hatanaka compressed (Hatanaka, 2008) Receiver INdependent EXchange (RINEX) format (Gurtner, 1994), and *Z* indicates compressed/zipped file. The Hatanaka compressed files can be decompressed by the software available at `ftp://terras.gsi.go.jp/software`

Table 3.1: Description of the selected GA network GPS/GNSS stations and the MWA

Station	Receiver type	Antenna type	Observables used	Location (degrees)	Observing sessions (Year,Day of Year)
MRO1	TRIMBLE NETR9	TRM59800.00	$L1$, $L2$, $C1$, $P2$	26.70° S 116.37° E	2014, 062, 063, 065, 075
MTMA	LEICA GRX1200+GNSS	LEIAR25.R3	$L1$, $L2$, $C1$, $P2$	28.11° S 117.84° E	2014, 062, 063, 065, 075
YAR3	LEICA GRX1200GGPRO	LEIAR25	$L1$, $L2$, $C1$, $P2$	29.04° S 115.34° E	2014, 062[a], 063, 065, 075
WILU	LEICA GRX1200+GNSS	LEIAR25.R3	$L1$, $L2$, $C1$, $P2$	26.62° S 120.21° E	2014, 062, 063, 065, 075
MWA	-	-	-	26.70° S 116.67° E	2014, 062, 063, 065, 075

[a] Partial data available, from 00:00:00 UTC to 18:07:00 UTC

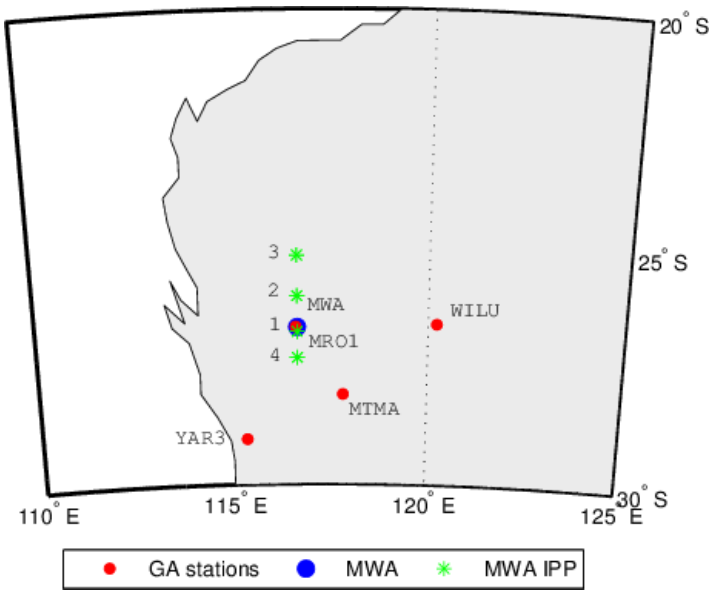

Figure 3.3: Selected GPS station locations from Geoscience Australia's network (red), MWA location (blue) and MWA IPP (green) for the four MWA observation nights (DOY 062, 063, 065 and 075 marked by 1 to 4).

3.3.1.1 Cycle-Slip Detection and Repair

When a receiver tracks a satellite, the integer and fractional number of cycles (total number of wavelengths at the GPS frequency) between the receiver and the satellite are recorded as phase observables. However, the initial number of phase cycles, upon first acquisition of the satellite signal, remain ambiguous, which are termed phase ambiguities. The ambiguities present in the phase observables remain constant for a complete satellite pass, unless a cycle-slip occurs. Cycle-slip can occur for a number of reasons including, temporary blocking of the GNSS signal by a physical obstruction, multi-path effects, high ionospheric activity, low signal-to-noise ratio (Hofmann et al., 2008). It is important to account for cycle-slips in order to ensure the continuity of carrier phase data on which high precision GNSS applications are dependent. Cycle-slips can be dealt with prior to processing the GNSS observables from the Receiver INdependent EXchange (RINEX) format (Gurtner, 1994) observation data, known as 'pre-processing', or in real-time. In this work we address cycle-slips during the pre-processing of the GNSS observables.

There are three stages for pre-processing of cycle-slips. Firstly, the cycle-slip is detected, secondly its magnitude is quantified, and thirdly it is flagged

Table 3.2: Daily solar and geomagnetic indices for the selected MWA observation days

Year, DOY	Solar Flux at 10.7 cm (F10.7[a]) $10^{-22}Wm^{-2}Hz^{-1}$	Planetary K index (Kp[b]) 3 hourly, from 00 to 24 UTC, ranging from 0-9 (low-high)							
2014, 062	161	3	2	2	2	2	1	1	1
2014, 063	158	2	1	0	2	3	2	2	3
2014, 065	149	1	1	1	2	2	2	3	1
2014, 075	136	1	1	1	0	0	0	1	0

[a] National Geophysical Data Center (NGDC), National Oceanic and Atmospheric Administration (NOAA) ftp://ftp.ngdc.noaa.gov/STP/GEOMAGNETIC_DATA/INDICES/KP_AP/2014 [b] Space Weather Prediction Center (SWPC), NOAA, BOULDER, USA ftp://ftp.swpc.noaa.gov/pub/warehouse/2014

or accounted for in the observables. While pre-processing GNSS observables, the generic approach to cycle-slip detection is by forming linear combinations of observables. During pre-processing using the BERNESE software (Dach, R. and others, 2007), a combination of the phase and code observables is formed, also known as Melbourne-Wübbena combination (Melbourne, 1985; Wübbena, G, 1985), which allows detection of cycle-slips. The new observables formed by the Melbourne-Wübbena combination is referred to as L6 observable, given as follows

$$\mathrm{L6} = \frac{1}{f_1 - f_2}\left(f_1\mathrm{L1} - f_2\mathrm{L2}\right) - \frac{1}{f_1 + f_2}\left(f_1\mathrm{P1} + f_2\mathrm{P2}\right) \tag{3.8}$$

$$\mathrm{L5} = \frac{1}{f_1 - f_2}\left(f_1\mathrm{L1} - f_2\mathrm{L2}\right) \tag{3.9}$$

$$\mathrm{L3} = \frac{1}{f_1^2 - f_2^2}\left(f_1^2\mathrm{L1} - f_2^2\mathrm{L2}\right) \tag{3.10}$$

It can be noted from equation (3.8) that, the noise of the L6 observable, in Melbourne-Wübbena combination is driven by the noise of the code observable, the code observables are found to have a precision of 25 cm or worse. Other combinations, namely, the "wide-lane" (the new observable is denoted as L5, refer equation (3.9)) (Hofmann et al., 2008) and "ionosphere-free" (the new observable is denoted as L3, refer equation (3.10)) (Hofmann et al., 2008) combinations, although driven by the very precise phase observables, have noise of 5.7 and 3.0 times the original observables, respectively (Dach, R. and others, 2007).

$$\mathrm{L4} = \mathrm{L1} - \mathrm{L2} \tag{3.11}$$

In this chapter, a method for detecting cycle-slips is presented. The cycle-slips are detected by forming linear combination, L1-L2, also known as GF model. The equations (2.22) - (2.23), presented in Chapter 2, Section 2.5.1, for $\Phi_{r,21}$ and $P_{r,21}$ indicate GF phase and code observables, respectively. Subscripts r indicate receiver, and 21 indicate the frequency difference of observables, that is, $\Phi_{r,1} - \Phi_{r,2}$. Subscript for the satellite is not presented since the data integrity is performed for a single satellite arc at a time, however it is already introduced earlier in Chapter 2, Section 2.5.1.

The cycle-slip is detected using the phase observables of the GF model. For a GF combination, the new phase observables ($\Phi_{r,21}$) has the constant instrumental term, which has ambiguities and other biases, and the ionospheric error. The time difference of the $\Phi_{r,21}$ observables, $\Phi_{r,21}(t) - \Phi_{r,21}(t-1)$ can be used to eliminate all other terms except the variable part of the ionospheric error. Any unusual variation in the ionosphere can be easily flagged for a cycle-slip. Such examples of cycle-slip detection can be found in the literature (Vaclavovic & Dousa, 2015), which is also used in this work, given as follows:

$$|\Phi_{r,21}(t) - \Phi_{r,21}(t-1)| > k \cdot \sigma_{\Phi_{r,21}} + \Delta I_{max} \tag{3.12}$$

where $\Phi_{r,21}$ is the GF observable formed from GNSS phase observables $\Phi_{r,1}$ and $\Phi_{r,2}$, t is the observation time, k is a scaling factor, $\sigma_{\Phi_{r,21}}$ is the precision of the $\Phi_{r,21}$ observable, and I_{max} is the maximal ionospheric delay. ΔI_{max} can be empirically chosen to 0.4 $m/hour$ and the factor k to 4 for GNSS frequencies.

Once the cycle-slip is detected, the hypothesis can further be tested by using the GF code observable ($P_{r,21}$) for a sufficient number of epochs (Teunissen & Kleusberg, 1998).

The cycle-slip can be repaired by estimating the elapsed time of propagation in the ionosphere from $\Phi_{r,21}$ observables, using the information before and after the slip. The $\Phi_{r,21}$ observables being precise, are capable of sensing ionosphere variations as small as 0.07 Total Electron Content Unit (TECU) (at GPS frequencies, 1 TECU = 10^{16} electrons/m^2). Figure 3.4 shows an example of multiple GLONASS cycle-slips for a single satellite pass, which were repaired with the algorithm described above. Considering the location of GNSS receivers used in this study (far below the equatorial anomaly), phenomenon such as scintil-

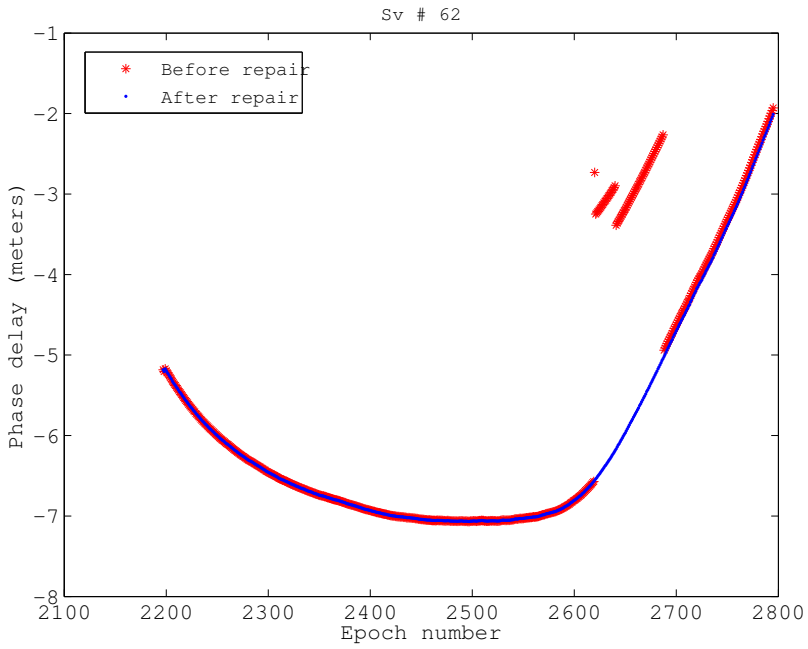

Figure 3.4: An example of a cycle-slip for GLONASS satellite, before repair (red) and after the cycle-slip is repaired (blue).

lations are not expected to be observed. However, variations of the order of 1 TECU every 30 seconds can be easily accounted for, if due to ionosphere, by this algorithm.

The above algorithm, however, is not capable of differentiating whether the slip occurred on the $\Phi_{r,1}$ or $\Phi_{r,2}$ GPS frequency. Since our software makes use of $\Phi_{r,21}$ observables for estimating the ionosphere and other unknowns, estimating cycle-slips at individual frequencies is not a concern.

3.3.2 CODE IONEX Maps

The daily ionosphere maps from the CODE, available in IONosphere Map EXchange Format (IONEX), are based on a global network of ∼200 GPS/GNSS stations. The line of sight GPS ionospheric delay is mapped to $VTEC$ using a Modified Single Layer Model (MSLM) mapping function approximating the Jet Propulsion Laboratory (JPL) Extended Slab Model (ESM) (for ESM mapping function see, Coster et al., 1992). The MSLM[5] is given as follows:

[5] www.aiub.unibe.ch/download/users/schaer/igsiono/doc/mslm.pdf

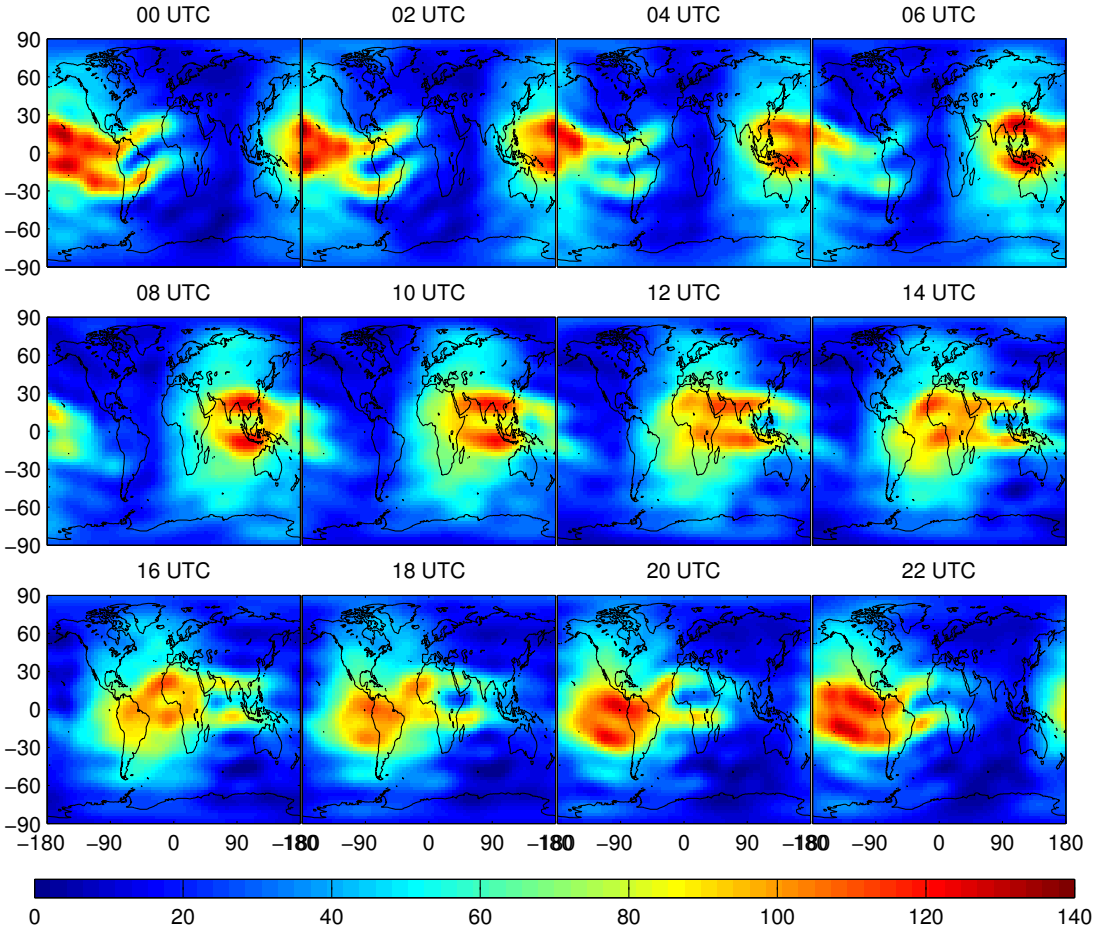

Figure 3.5: Global TEC (TECU) from CODE IONEX maps for DOY 062, year 2014.

$$F_{MSLM} = \frac{1}{\cos z'}; \quad \sin z' = \left(\frac{R}{R+H} \cdot \sin(\alpha z) \right). \tag{3.13}$$

where $H = 506.7$ km and $\alpha = 0.9782$.

The $VTEC$ is modelled using spherical harmonic coefficients of order and degree 15 in the solar magnetic reference frame as snapshots with an ionosphere refreshing interval of 2 hours (Schaer et al., 1996). The spatial resolution of CODE maps is 5°/2.5° in longitude/latitude, respectively. The spherical harmonic model used by CODE to interpret the global ionosphere is described in Schaer et al. (1996).

CODE maps are available as daily final solutions in CODE's online archive[6].

[6] `ftp://ftp.unibe.ch/aiub/CODE/`*yyyy*/*CODGddd.yyI*, where *yyyy* and *yy* are the four and two digit year, *ddd* is the DOY. The ionosphere maps are exchanged in IONEX format, see

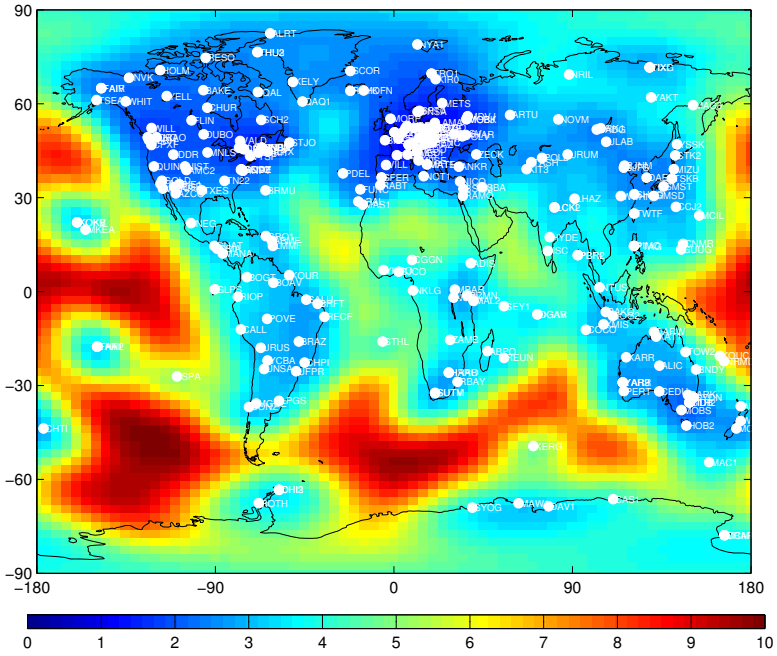

Figure 3.6: Average RMS (1-σ uncertainties) in TECU, of CODE IONEX maps for DOY 062, year 2014, marked in white are the GPS/GNSS stations considered for the solution.

Figure 3.5 presents the 2 hour snapshots for the day 03-03-2014 (DOY 062), which is one day of interest for the MWA observations. The average CODE $VTEC$ RMS (Root Mean Square error) is shown in Figure 3.6. The RMS of the $VTEC$ fit is higher over oceans and regions with sparse coverage of GPS/GNSS receivers, due to limited data points available for the fit.

3.4 Measurement of the Ionosphere Using MWA Observations

3.4.1 MWA Observations

For comparison with our GPS modelling of the ionosphere, we used observations from the GLEAM survey (Wayth et al. (2015); Hurley-Walker et al. (2017)). In this survey, the MWA observes in meridian drift-scan mode, where the telescope remains pointing at a single point on the meridian throughout the night. Four nights from March 2014 were chosen, when the telescope was pointed close to the

Schaer et al. (1998) for detailed description of IONEX data format and its interpolation.

zenith. The ionosphere pierce point corresponding to the pointing centre of the telescope is shown for each night in (Figure 3.7).

During GLEAM observations, the instrument cycles five frequency bands, centred on approximately (88 MHz, 118 MHz, 154 MHz 185 MHz and 215 MHz), with a dwell time of 2 minutes on each band, each band having an instantaneous bandwith of 30.72 MHz. Each two-minute observation is then imaged with separate images being generated for 4 subbands (each having a bandwidth of 7.68 MHz). The position of a prepared list of bright sources was then determined for each of these images.

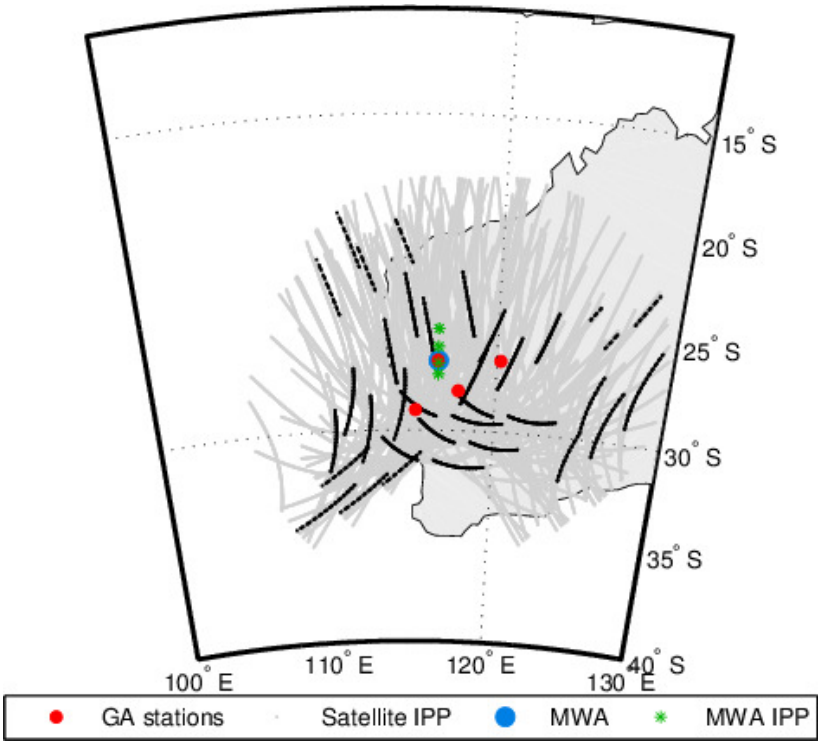

Figure 3.7: GA station locations (red) with satellite IPPs in earth fixed reference frame over a period of 24 hours (grey) and for 1 hour during the MWA observations (black). The MWA is marked in blue, whereas the IPP of the MWA is shown in green.

3.4.2 MWA Ionospheric Modelling

By comparing the position of each source in all four subbands, it is possible to quantify the effect of the ionosphere, separating it from instrumental and calibration effects. By making a least-squares fit to all four points, the contribution

of the ionosphere (the gradient) can be determined for each source. The offset in position at each frequency is shown in Figure 3.9 for a single strong source. It can be seen that the change in apparent position of the source depends precisely on λ^2, exactly as would be expected from ionospheric refraction.

A comprehensive analysis of this dataset using MWA observations is underway (J. Morgan et al. in preparation). For this analysis, ionospheric gradient were estimated over all sources detected in each snapshot. Figure 3.8 shows the gradient of this fit for each source, scaled by λ^2 for the highest frequency offset shown in the left panel. The fact that the average reduced χ^2 for each observation is ~ 1, and the fact that $\lambda = 0$ position of the sources remains at zero throughout the night, both serve to reinforce the hypothesis that the shift in sources is largely due to the ionosphere.

For simplicity, only the lowest-frequency data were used, since these observations are the most sensitive to ionospheric effects, and still yield sufficient time resolution. This yields two time series (on in the North-South (NS) direction and one in the East-West (EW) direction) representing the average shift due to the ionosphere of ∼100 sources within a 35°radius of the pointing centre. In order that these shifts could be compared directly with GPS measurements, both measurements were scaled to a common reference frequency of 150 MHz and the (angular) offset was converted to radians.

3.5 Results and Discussion

3.5.1 Comparison of VTEC With CODE IONEX

The $VTEC$ was estimated by our software at a time resolution of 10 minutes as described in Section 3.2.3 with software developed in MATLAB for the location of the four GPS stations, MRO1, MTMA, YAR3, and WILU. The CODE values of $VTEC$ are available at intervals of 2 hours. Values of the $VTEC$ corresponding to our time resolution were interpolated from CODE $VTEC$ maps (see Schaer et al., 1998) for each of the four GPS locations. Our estimated values of $VTEC$ along with the CODE $VTEC$ values are presented in Figure 3.10 for DOY 062, year 2014. Figures 3.10(a), 3.10(b), 3.10(c), 3.10(d), present $VTEC$ for MRO1, MTMA, YAR3, and WILU respectively for DOY 062. The $VTEC$ for all the selected GPS stations for DOY 063, 065 and 075 are presented in Figures 3.11, 3.12 and 3.13. Figure 3.14 shows the difference between our $VTEC$ estimates

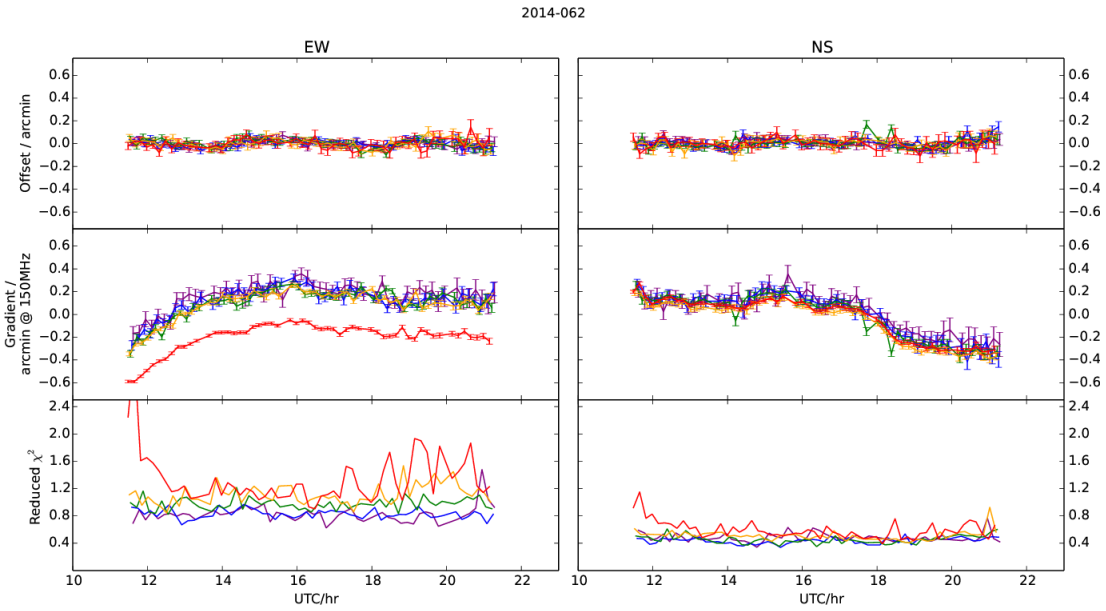

Figure 3.8: Offset (extrapolated to $\lambda = 0$), gradient (ionospheric offset at 150 MHz), and reduced χ^2 of a fit of source position offset as a function of λ^2. Each point is for a single observation, all quantities are averaged over all (100) sources detected in that observation. Left panels are for the East-West position offset (Right Ascension) right panels are for the North-South position offset (Declination). Red, Yellow, Green, Blue and Purple are for the 88 MHz, 118 MHz, 154 MHz 185 MHz and 215 MHz bands respectively. Note that the gradients (in arcmin m^1) have been multiplied by 4, representing an offset at a wavelength of 2 m (=150 MHz). Note that a different observation is used for self calibration for each frequency band, resulting in an arbitrary DC offset for each band.

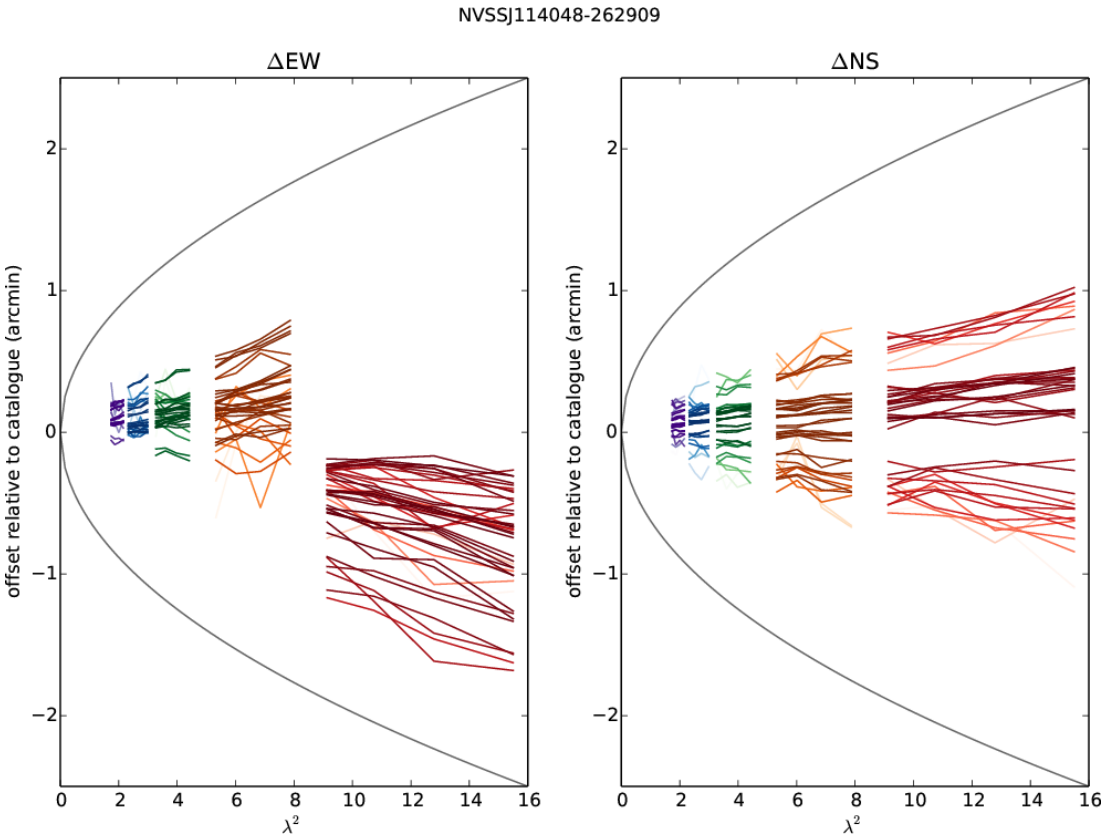

Figure 3.9: Source position offset against λ^2 (m^2) for a strong source. Each line represents a measurement of the source in each of four subbands in a single 2-minute observation. There are many lines since the source in multiple observations as it passes through the field of view. Left panel presents the East-West position offset (Right Ascension) right panel presents the North-South position offset (Declination). Red, Yellow, Green, Blue and Purple are for the 88 MHz, 118 MHz, 154 MHz 185 MHz and 215 MHz bands respectively. More significant detections are given a darker colour. Note that each band is calibrated seperately, so there is an arbitrary offset in the gradients between each of the 5 bands.

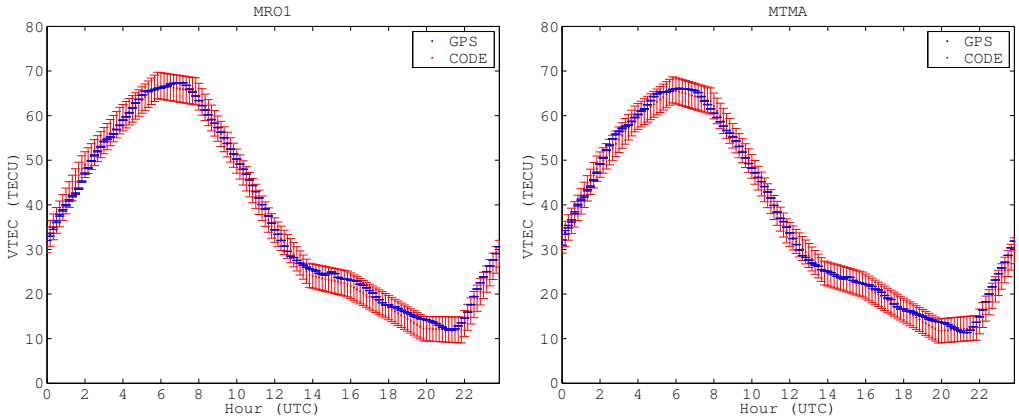

(a) $VTEC$ at station MRO1

(b) $VTEC$ at station MTMA

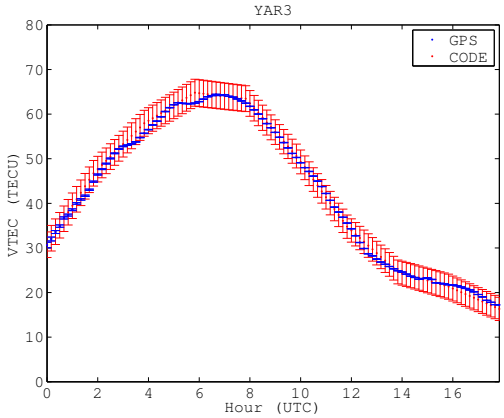

(c) $VTEC$ at station YAR3

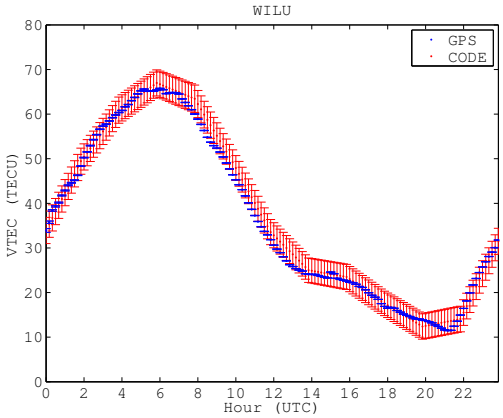

(d) $VTEC$ at station WILU

Figure 3.10: $VTEC$ at stations MRO1, MTMA, YAR3, and WILU estimated using the method described in the text (blue curve) and CODE IONEX (red curve) on DOY 062, year 2014.

with respect to CODE. The F10.7 solar flux, presented in Table 3.2, is highest on DOY 062 and lowest on 075. This is reflected in the $VTEC$ values, they reach a maximum of ∼68 TECU on DOY 062 and ∼57 TECU on DOY 075 for MRO1, refer Figures 3.10(a) and 3.13(a). The 1σ uncertainties in CODE maps reach a maximum of 8 TECU (Figure 3.6). The differences between CODE and our $VTEC$ are found to lie within the errors, with the differences ranging between -6 to 6 TECU for four different days of observations, (Figure 3.14).

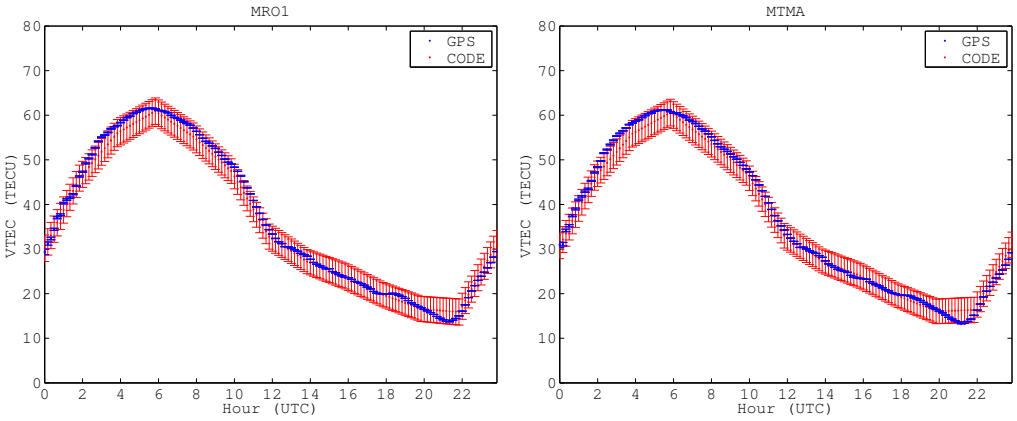

(a) $VTEC$ at station MRO1

(b) $VTEC$ at station MTMA

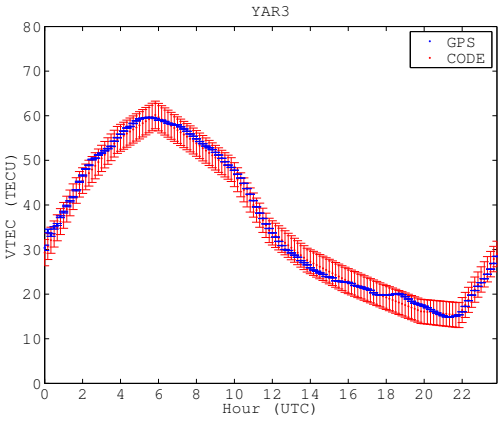

(c) $VTEC$ at station YAR3

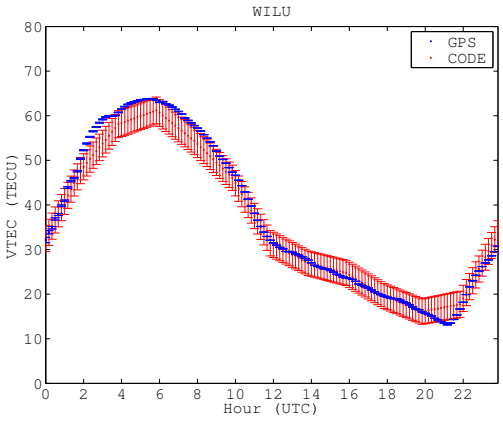

(d) $VTEC$ at station WILU

Figure 3.11: $VTEC$ at stations MRO1, MTMA, YAR3, and WILU estimated using the method described in the text (blue curve) and CODE IONEX (red curve) on DOY 063, year 2014.

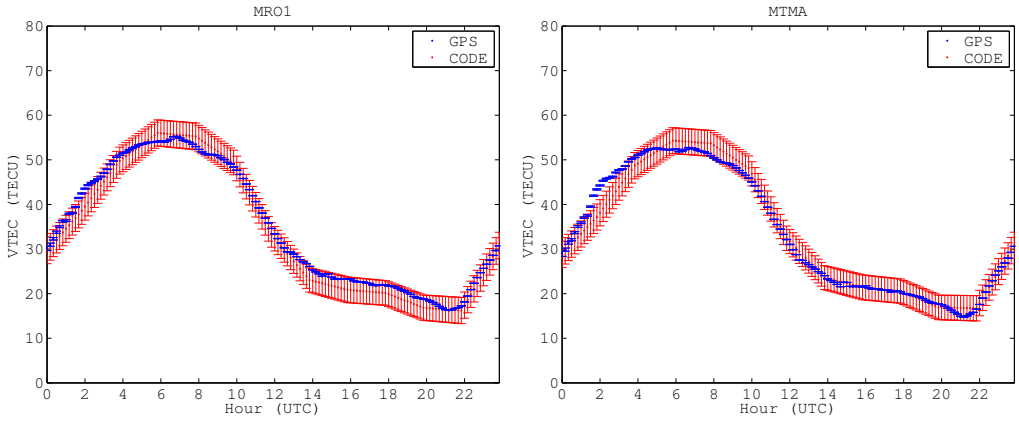

(a) $VTEC$ at station MRO1

(b) $VTEC$ at station MTMA

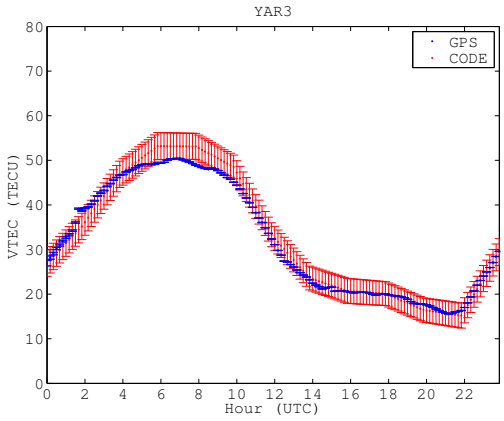

(c) $VTEC$ at station YAR3

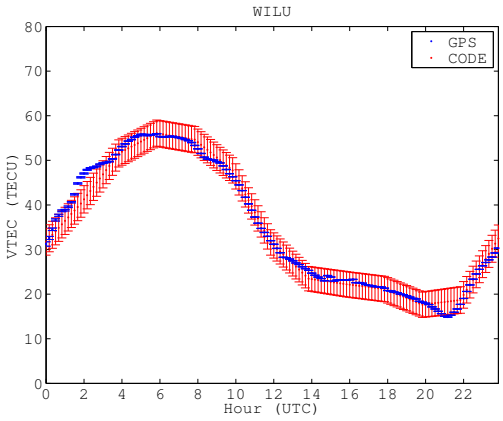

(d) $VTEC$ at station WILU

Figure 3.12: $VTEC$ at stations MRO1, MTMA, YAR3, and WILU estimated using the method described in the text (blue curve) and CODE IONEX (red curve) on DOY 065, year 2014.

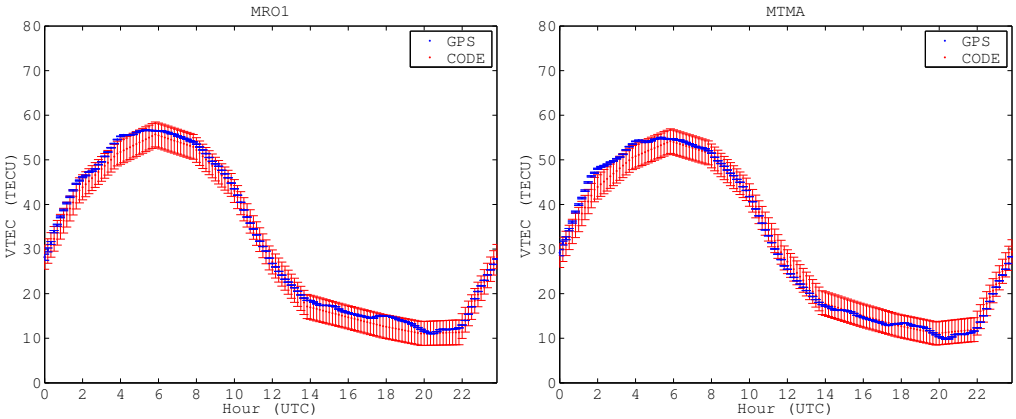

(a) $VTEC$ at station MRO1

(b) $VTEC$ at station MTMA

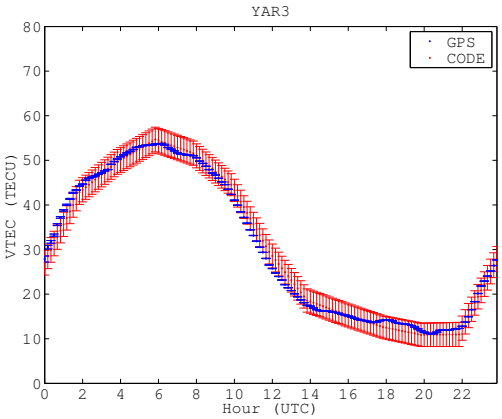

(c) $VTEC$ at station YAR3

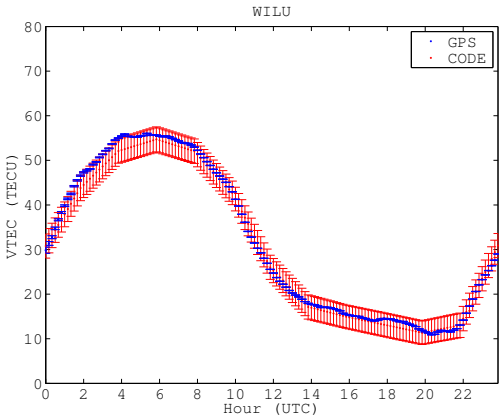

(d) $VTEC$ at station WILU

Figure 3.13: $VTEC$ at stations MRO1, MTMA, YAR3, and WILU estimated using the method described in the text (blue curve) and CODE IONEX (red curve) on DOY 075, year 2014.

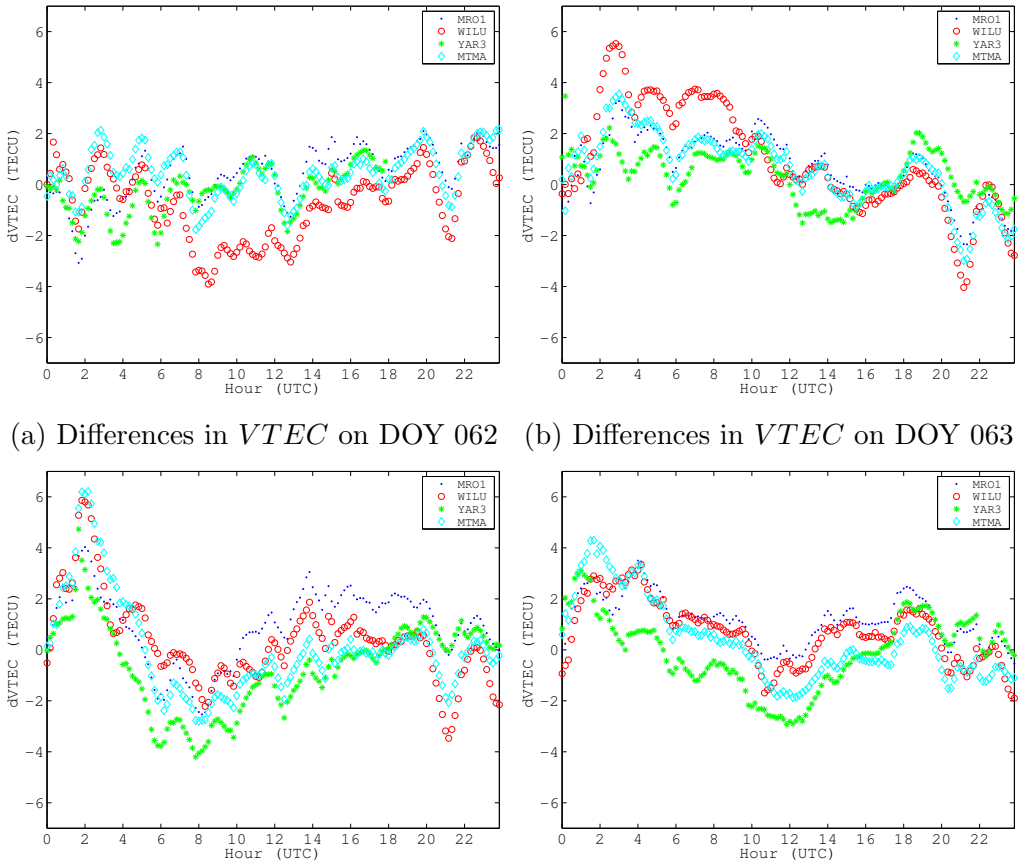

(a) Differences in $VTEC$ on DOY 062 (b) Differences in $VTEC$ on DOY 063

(c) Differences in $VTEC$ on DOY 065 (d) Differences in $VTEC$ on DOY 075

Figure 3.14: Differences in $VTEC$ w.r.t CODE for stations MRO1, MTMA, YAR3, and WILU for DOY 062, 063, 065 and 075 year 2014.

3.5.2 Comparison of Receiver DCBs

The receiver DCBs given by $d_{r,21}$ in equation (2.23) are the inter-frequency biases on code GPS data. Estimation of receiver DCBs is important for correct estimation of ionospheric parameters from GPS/GNSS observables (Gaposchkin & Coster, 1992; Sardon et al., 1994; Teunissen & Kleusberg, 1998). The receiver DCBs were estimated as described in Section 3.2.3. In addition, the BERNESE GNSS data processing software (Dach, R. and others, 2007) was used to estimate receiver DCBs for the selected GA GPS/GNSS stations given in Table 3.1. BERNESE 5.0 Precise Point Positioning (PPP) processing estimates one set of station specific ionosphere parameters for the entire session as well as receiver DCBs using the script `PPP_ION` (Dach, R. and others, 2007). With BERNESE PPP it is possible to obtain centimetre level station positions using precise satellite orbits, satellite clock and Earth Orientation Parameters (EOP) along with the receiver DCB.

The station specific ionosphere parameters are estimated by BERNESE PPP by forming frequency-differenced geometry-free observables. In this work, frequency-differenced observables were used to estimate station specific parameters. Unlike BERNESE PPP where only one set of ionospheric coefficients are estimated for a given session, we make use of a Kalman filter to estimate the ionosphere every 10 minutes and a single value of receiver-satellite DCB for an entire session.

Since there exists a rank deficiency between the receiver and satellite DCBs. To overcome this rank deficiency, CODE[7] assumes a zero-mean condition over all the satellite DCBs, $\sum_{s=1}^{m} DCB^s = 0$. By assuming a zero-mean condition it implies that the DCB results may be shifted by a common offset value (see Dach, R. and others, 2007, Chapter 13), which is a function of total number of satellites m considered for the solution. Hence an independent $\mathcal{S}$-basis was formed for estimation of DCBs.

Our estimated receiver DCBs and BERNESE PPP estimates are compared in this section. CODE also provides estimates of receiver DCBs which are estimated while performing a global fit for ionosphere parameters. However, of the selected stations used in this study, only receiver DCBs for station YAR3 are available from CODE.

Figure 3.15 shows our estimated receiver DCBs (blue), with BERNESE (red)

[7] http://igscb.jpl.nasa.gov/igscb/center/analysis/archive/code_20080528.acn

Table 3.3: Differences between our estimated receiver DCBs with BERNESE and CODE for DOY 062, 063, 065 and 075, year 2014.

Station	Difference (ns) w.r.t BERNESE				Difference (ns) w.r.t CODE			
	Year 2014, DOY				Year 2014, DOY			
	062	063	065	075	062	063	065	075
MRO1	-1.311	-0.861	-0.651	-0.648	-	-	-	-
MTMA	-0.640	-0.760	-0.629	-0.882	-	-	-	-
YAR3	-1.262	-0.475	-0.778	-0.756	0.553	0.230	0.095	0.055
WILU	-0.924	-0.806	-0.711	-0.980	-	-	-	-

and from CODE (cyan) for DOY 062. Table 3.3 presents the differences between our estimated receiver DCBs and BERNESE and CODE values. In comparison with BERNESE estimated DCBs, differences are between -0.475 to -1.311 ns which corresponds to -1.356 to -3.743 TECU. Whereas comparing to CODE DCBs, the DCB for YAR3 differed by 0.055 ns to 0.553 ns, 0.157 to 1.579 TECU.

Hong et al. (2008) estimated the receiver DCBs by initially estimating single differenced DCBs. Further, by finding the time t_0 for which the single difference geometric range is zero, absolute receiver DCBs were computed. Hong et al. (2008) compared the estimated receiver DCBs with BERNESE values and found the maximum difference to lie around 15cm or 0.5ns. Arikan et al. (2008) estimated the receiver DCBs using IONOsphere research LABoratories single-station receiver BIAS estimation algorithm (IONOLAB-BIAS) method and compared them with CODE estimates. Arikan et al. (2008) found the differences in receiver DCBs to lie between -0.552ns and 0.110ns for different receivers.

3.5.3 Comparison of GPS Ionospheric Gradients With the MWA Observed Gradients

The gradients in the East-West (EW) and North-South (NS) directions were computed from the ionosphere first order coefficients given in equation (3.5) for each of the selected stations and compared with MWA observed gradients.

It should be noted that for deriving MWA gradients, a calibration solution had to be derived comprising of the data from the full array (amplitude and phase

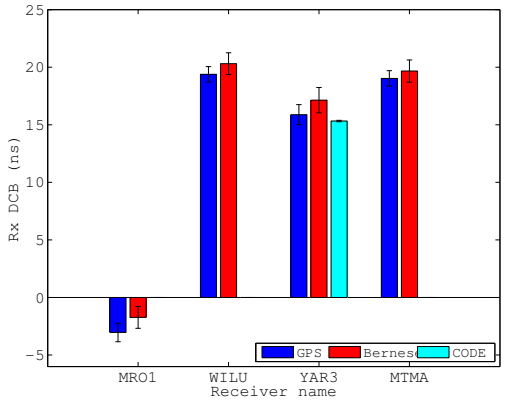

(a) Receiver DCBs for DOY 062, year 2014

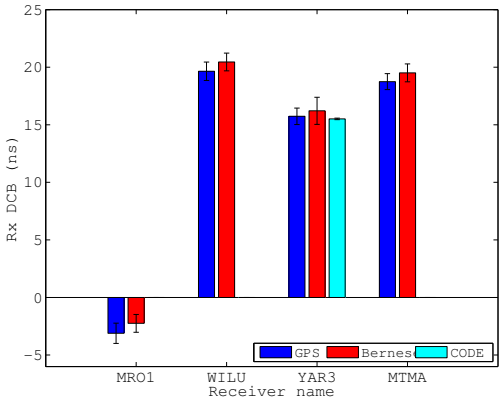

(b) Receiver DCBs for DOY 063, year 2014

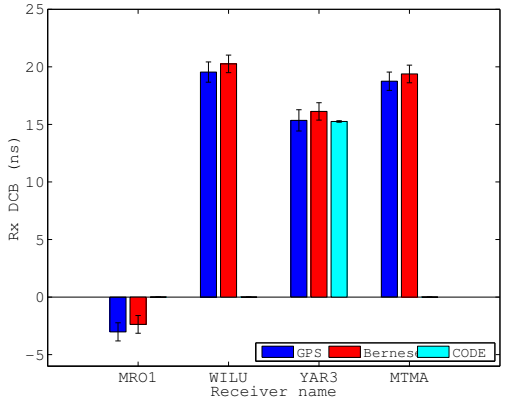

(c) Receiver DCBs for DOY 065, year 2014

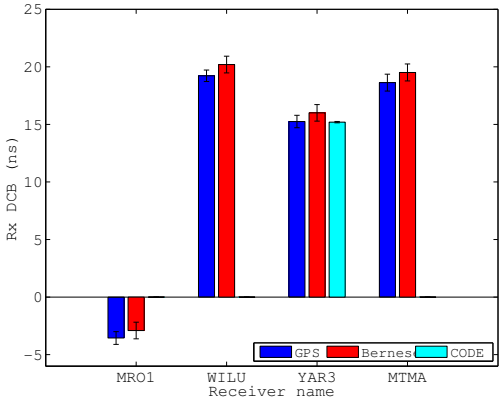

(d) Receiver DCBs for DOY 075, year 2014

Figure 3.15: Comparison of our estimated receiver DCBs (blue) with BERNESE estimates (red) and CODE DCBs (cyan) for DOY 062, 063, 065 and 075, year 2014.

correction for each antenna), based on an observation of a strong astrophysical source with known structure. This 'self calibration' procedure corrects for both instrumental effects, and the prevailing ionospheric conditions towards the source at the time of the calibration observation. All ionospheric gradients in this thesis derived from the MWA are therefore relative, and each will have an arbitrary DC bias relative to the true gradient estimated by GNSS observations. This calibration procedure is carried out only once per night, and so each timeseries of ionospheric gradients is self-consistent.

Figure 3.16 presents each of the EW and NS gradients for all the GA GPS stations and MWA. Figures 3.16(a), 3.16(c), 3.16(e),and 3.16(g), show the EW gradients for DOY 062, 063, 065 and 075 of year 2014, respectively. The NS gradients are presented in Figures 3.16(b), 3.16(d), 3.16(f),and 3.16(h) for DOY 062, 063, 065 and 075 of year 2014, respectively. In each of the subplots, along with the GPS ionospheric gradients, the MWA observed gradients are shown.

Table 3.4 presents the correlation between GPS and MWA gradients in the EW and NS directions for the four days of observations. The IPP separations in longitude ($|\Delta\lambda_{IPP}|$) and latitude ($|\Delta\phi_{IPP}|$) for each of the GPS stations and MWA are presented in Table 3.4. The correlation between the GPS and MWA ionosphere gradients is computed using Pearson's coefficient of correlation, r, for an assumed mean method along with the standard error, σ_r, refer Fisher (1936).

There is a high correlation in the EW and NS gradient between GPS and MWA for most of the GPS stations for all the days (Table 3.4). The NS gradients had a weak correlation with YAR3 for most days. The correlation was highest on DOY 075 while the IPP was closest among the four days of observation (Table 3.4). The EW gradient showed consistent good correlation with MRO1 GPS stations, whereas correlation with WILU seemed to be most inconsistent (Table 3.4). A general trend seemed to show that the EW gradient correlation was proportional to the longitudinal difference and the NS gradient correlation to the latitude difference. For DOY 075 while the solar activity was the lowest among the selected days (Table 3.2), the EW gradient was found to be high for all the stations. NS gradient did not have a similar behaviour.

Table 3.5 and Figure 3.16 present the comparison of zenith EW and NS gradients between GPS stations. Correlation for the EW and NS gradients, presented in Table 3.5, were computed between each of the selected GPS stations for the time window of MWA observations (marked by the red line in Figure 3.16). Table

3.5 summarises the inter-station EW and NS gradient correlations. Inter-station correlation is strong for the EW and NS gradient for almost all the days between all the stations. The EW gradient is consistently strong between all the stations, however the NS gradient is found to be weakest between WILU and YAR3 which have a distinguished latitudinal and longitudinal separation (Figure 3.3).

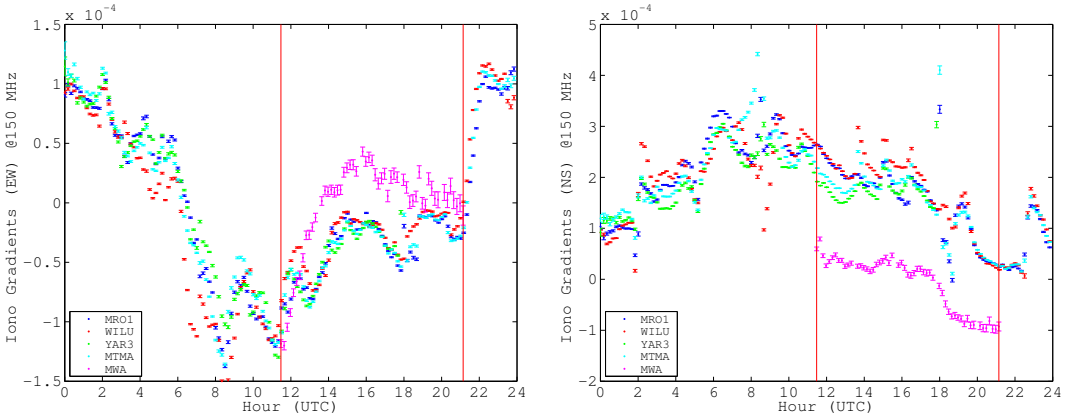

(a) EW gradient for DOY 062

(b) NS gradient for DOY 062

Figure 3.16: EW and NS ionosphere gradients for selected GA stations and MWA for DOY 062, 063, 065 and 075 for year 2014. The time window related to MWA observations is shown by red line.

3.6 Summary

This chapter presents a single-station approach to estimate $VTEC$ ionosphere gradients. The $VTEC$ and ionosphere gradients were estimated at intervals of 10 minutes. The ionosphere gradients in the EW and NS direction at the GPS station locations are in good agreement with the MWA observed gradients.

The ionosphere gradient analysis presented in this chapter brings forth various questions, namely, the variation of EW and NS gradients with respect to IPP separation, and the elevation dependency reflected by the correlation of gradients between the GPS station, MRO1, and MWA. With the limited data set, these questions cannot not be resolved comprehensively. In the following chapter, Chapter 4, work will focus on including more MWA observation and will attempt to closely probe the above questions in a statistical sense.

With our single-station approach, the GPS receiver DCBs can be accurately estimated for any available GPS receiver. Thus our method can be applied to

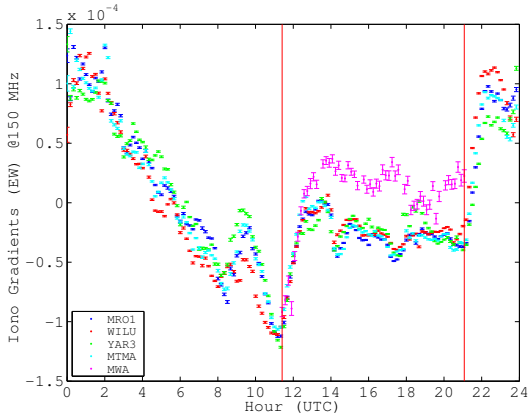

(c) EW gradient for DOY 063

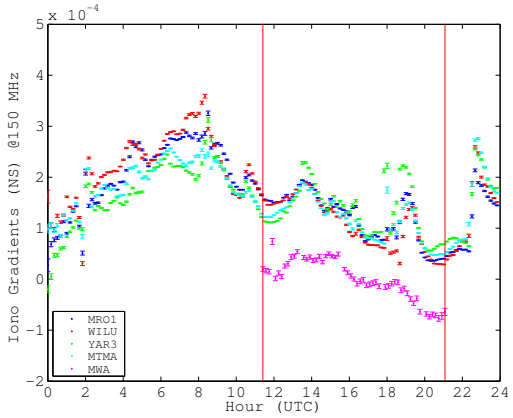

(d) NS gradient for DOY 063

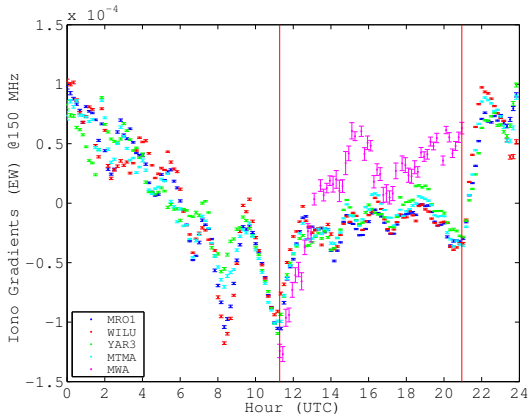

(e) EW gradient for DOY 065

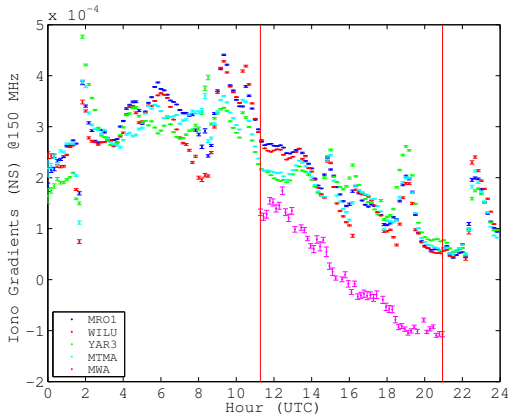

(f) NS gradient for DOY 065

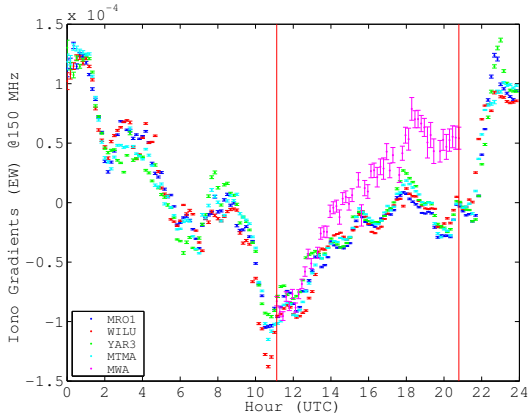

(g) EW gradient for DOY 075

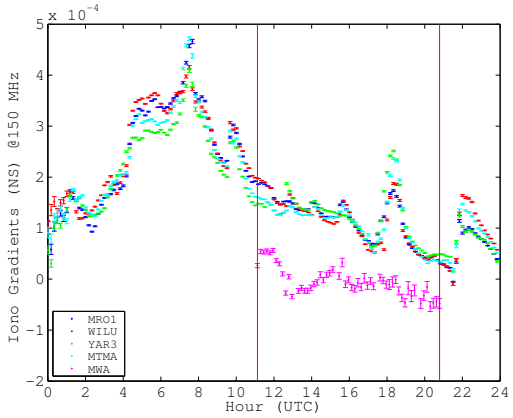

(h) NS gradient for DOY 075

Figure 3.16: EW and NS ionosphere gradients for selected GA stations and MWA for DOY 062, 063, 065 and 075 for year 2014. The time window related to MWA observations is shown by red line.

Table 3.4: Correlation between the GPS and MWA observed gradients in EW (r_{EW}) and NS (r_{NS}) components, its standard error (σ_r), and IPP separations in longitude ($|\Delta\lambda_{IPP}|$) and latitude ($|\Delta\phi_{IPP}|$) of GPS stations and MWA (ΔIPP) for DOY 062, 063, 065 and 075, year 2014.

Station	r_{EW} ($\sigma_{r_{EW}}$)				$\lvert\Delta\lambda_{IPP}\rvert$ (degrees)			
	Year 2014, DOY				Year 2014, DOY			
	062	063	065	075	062	063	065	075
MRO1	0.79(0.05)	0.73(0.06)	0.66(0.08)	0.93(0.02)	0.03	0.03	0.03	0.03
MTMA	0.72(0.07)	0.65(0.08)	0.71(0.07)	0.94(0.02)	1.17	1.17	1.17	1.17
YAR3	0.83[a](0.05)	0.73(0.06)	0.77(0.06)	0.92(0.02)	1.32	1.32	1.32	1.32
WILU	0.60(0.09)	0.83(0.04)	0.54(0.10)	0.94(0.01)	3.54	3.54	3.54	3.54
	r_{NS} ($\sigma_{r_{NS}}$)				$\lvert\Delta\phi_{IPP}\rvert$ (degrees)			
MRO1	0.84(0.04)	0.78(0.05)	0.87(0.03)	0.69(0.07)	0.10	0.65	1.51	0.65
MTMA	0.77(0.06)	0.75(0.06)	0.74(0.06)	0.46(0.11)	1.31	2.07	2.93	0.77
YAR3	0.21[a](0.16)	0.45(0.11)	0.50(0.10)	0.35(0.12)	2.24	3.00	3.86	1.70
WILU	0.89(0.03)	0.77(0.05)	0.86(0.04)	0.64(0.08)	0.17	0.58	1.43	0.72

[a]Partial data available, from 00:00:00 to 18:07:00 UTC (MWA observation window = $\sim$ 11 to 21 UTC)

Table 3.5: Inter-station correlation for the EW and NS gradients (r), its standard error (σ_r), and IPP separations in longitude ($|\Delta\lambda_{IPP}|$) and latitude ($|\Delta\phi_{IPP}|$) between GPS stations

Station	r_{EW} ($\sigma_{r_{EW}}$)				$\lvert\Delta\lambda_{IPP}\rvert$ (degrees)
	Year 2014, DOY				
	062	063	065	075	
MRO1-MTMA	0.88(0.03)	0.97(0.01)	0.94(0.02)	0.99(0.002)	1.21
YAR3-MTMA	-	0.83(0.04)	0.94(0.01)	0.97(0.01)	2.50
MTMA-WILU	0.90(0.03)	0.91(0.02)	0.92(0.02)	0.98(0.01)	2.37
MRO1-YAR3	-	0.89(0.03)	0.91(0.02)	0.97(0.01)	1.29
MRO1-WILU	0.88(0.03)	0.96(0.01)	0.93(0.02)	0.97(0.01)	3.58
WILU-YAR3	-	0.86(0.04)	0.84(0.04)	0.94(0.02)	4.87
	r_{NS} ($\sigma_{r_{NS}}$)				$\lvert\Delta\phi_{IPP}\rvert$ (degrees)
MRO1-MTMA	0.94(0.02)	0.92(0.02)	0.95(0.01)	0.89(0.03)	1.42
YAR3-MTMA	-	0.79(0.05)	0.88(0.03)	0.93(0.02)	0.93
MTMA-WILU	0.81(0.05)	0.87(0.03)	0.95(0.01)	0.90(0.03)	1.49
MRO1-YAR3	-	0.71(0.07)	0.83(0.04)	0.84(0.04)	2.35
MRO1-WILU	0.84(0.04)	0.91(0.02)	0.96(0.01)	0.96(0.01)	0.07
WILU-YAR3	-	0.53(0.10)	0.74(0.06)	0.79(0.05)	2.42

local GPS receiver data for which the DCBs are not publicly available.

To develop a regional model for the ionosphere, a multi-station approach needs to be adopted. Furthermore, the spatial resolution of ionosphere gradients is closely related to the scale of the GPS/GNSS receiver network on the ground. The scales at which MWA sees the ionosphere lie between 10 - 100 km. In order to estimate the ionosphere gradients on such scales, dense GPS networks of the order of the ionosphere scales seen by the MWA need to be present around MWA site. The existing GPS network near the MWA site is of scale 150 - 250 km, which limits the GPS based ionosphere research possible for the MWA.

In addition to GPS satellite data, other satellite systems can be used to densify the IPPs over the study area. Other global navigation systems like GLONASS, launched by Russia, BeiDou from China, and the European Union's Galileo could be adopted in our model. Of these three global navigation systems, only the GLONASS system is close to completely operational, with 23 operational satellites in orbit. GA receivers capture data from the GLONASS system, and using GLONASS data along with the GPS data has been shown to improve ionospheric modelling (Coster et al., 1999).

Chapter 4 will focus on developing a regional ionosphere model using data from both GPS and GLONASS satellite systems.

4

Comparison of First Order Ionospheric Effects Obtained Using Multi-Station GPS Models and MWA Observations

Adapted from:

Ionospheric Modelling using GPS to Calibrate the MWA. II: Regional ionospheric modelling using GPS and GLONASS to estimate ionospheric gradients B. S. Arora, J. Morgan, S. M. Ord, S. J. Tingay et. al., 2016, Publications of the Astronomical Society of Australia, Volume 33, doi:10.1017/pasa.2016.22.

4.1 Introduction

In Chapter 3, we undertook an initial study of refractive effects due to the ionosphere, as observed by the MWA, and compared them with independent measurements using the Global Positioning System (GPS). Bulk ionospheric gradients causing the refractive effects observed with the MWA were found to agree well with those estimated from GPS observables. The results presented in Chapter 3 establish a methodology and show that ionospheric information can plausibly be obtained from GPS, to help calibrate the MWA.

In Chapter 3, the ionosphere is modelled by assuming it to be concentrated at a single layer, stationary and fixed at a height of 450 km, as also assumed with global GNSS (Global Satellite Navigation System) centres, for example CODE (Centre for Orbit Determination in Europe). This assumption was made in order to allow ready comparison between our techniques and CODE analysis, for example. For a single layer model, the ionosphere obliquity factor, which maps

the slant ionosphere to the vertical, and the coordinates at the Ionospheric Pierce Points (IPP) are computed using the height of the single layer. As a simplified model, this proved successful.

The research presented in this chapter aims to build on our earlier work. In Chapter 3, the ionospheric modelling was performed by using data from a single GPS station for any given ionospheric solution. To capture the ionospheric behaviour on finer spatial resolution over regional scales, additional data need to be incorporated for ionospheric modelling. To this end, we incorporate the GLONASS satellite system into our analysis. GLONASS currently has 24 active satellites in orbit. The data for GLONASS are available for the ground stations in the Geoscience Australia (GA) network. Further, we now upgrade our "*single-station*" analysis to a "*multi-station*" analysis, whereby each ionospheric solution we calculate uses data from multiple receiving stations.

Finally, we explore the effectiveness of various relaxations of the single layer model for ionospheric modelling. Methods to include spatial and temporal variations into the height of the single layer model are discussed.

Thus, we start from the methodology presented in Chapter 3 and explore a number of extensions to this methodology: 1) addition of GLONASS data to the GPS data; 2) a multi-station analysis approach rather than a single-station approach; and 3) exploration of ionospheric models more complex than single layer.

This chapter is organised as follows; Section 4.2 recalls the combined GPS and GLONASS observation model. Further, the effect of the single layer model height on the estimated ionosphere coefficients and methods to incorporate the variation in single layer model height are presented. The multi-station approach to estimate ionosphere coefficients using GPS and GLONASS is presented in Section 4.2. Section 4.3 presents the summary of obtaining ionosphere gradients from MWA observations as a function of position shifts. The results from the multi-station approach are presented and discussed in Section 4.4. The Chapter is concluded in Section 4.5, where we discuss future directions for this work.

4.2 Ionospheric Modelling Using GPS and GLONASS

4.2.1 GPS and GLONASS Observation Model

The GF GPS and GLONASS observation model is discussed in detail in Chapter 2. We recall the GPS and GLONASS GF model observation equations described in Chapter 2, Section 2.6.1, equations (2.25) to (2.28), given as follows

$$
\begin{aligned}
E(\Phi^{Gs}_{r,21}) = \Phi^{Gs}_{r,1} - \Phi^{Gs}_{r,2} &= -\iota^{Gs}_{r,21} + \mathrm{C}^{Gs}_{r}, \\
E(P^{Gs}_{r,21}) = P^{Gs}_{r,1} - P^{Gs}_{r,2} &= \iota^{Gs}_{r,21} + c \cdot (d_{r,21} - d^{Gs}_{,21}). \\
E(\Phi^{Rs}_{r,21}) = \Phi^{Rs}_{r,1} - \Phi^{Rs}_{r,2} &= -\frac{\mu^{R}_{21}}{\mu_{21}}\iota^{s}_{r} + \mathrm{C}^{Rs}_{r}, \\
E(P^{Rs}_{r,21}) = P^{Rs}_{r,1} - P^{Rs}_{r,2} &= \frac{\mu^{R}_{21}}{\mu_{21}}\iota^{s}_{r} + c \cdot d^{Rs}_{r,21}.
\end{aligned}
$$

where $E(\cdot)$ is the expectation operator, Φ is the phase observable, P is the code observable, subscript $_r$ indicates receiver, $_1$, $_2$ and $_{21}$ indicates GNSS frequency/frequency combinations corresponding to phase (or code) observables, $L1$ (or $C1$), $L2$ (or $P2$) and $L4$ (or $P4$), respectively, superscripts ^{Gs}, ^{Rs} indicate GPS and GLONASS satellites, respectively, $c \cdot (d_{r,21})$ and $c(d^{Gs}_{,21})$ are the GPS receiver and satellite Differential Code Biases (DCBs), respectively, μ_{21} is the GPS frequency coefficient given as, $\mu_{21} = \mu_1 - \mu_2$ and $\mu_1 = \frac{1}{f_1^2}$, $\mu_2 = \frac{1}{f_2^2}$, f_1 and f_2 are GPS frequencies at $L1$ and $L2$. Similarly, the GLONASS frequency coefficient is given by μ^{R}_{21}.

The instrumental biases and other unknowns are estimated for each GNSS receiver using least squares and kalman filter approaches as described in Arora et al. (2015). The precision of the time-constant parameters propagate as the inverse of the square-root of the number of epochs (n), $\sigma = 1/\sqrt{n}$. For a continuous satellite arc, n is very large, of the order of 100 epochs or more. This results in a very precise estimation of time-constant parameters.

The Total Electron Content (TEC) between the receiver and the satellite, also known as Slant TEC ($STEC$) can hence be retrieved from GF phase observables ($\Phi_{r,21}$), for both GPS and GLONASS satellites, by substituting for the

time-constant parameters estimated for GF observables. Figure 4.1 presents the retrieved $STEC$ for the selected GA GNSS stations on DOY 062. The seven selected GA stations are, MRO1 (Murchison), WILU (Wiluna), MTMA (Mount Magnet), YAR3 (Yaragadee), MEDO (Meadow), GASC (Gascoyne) and TOMP (Tom Price). The description for each of the GNSS station can be found in Table 4.1.

4.2.2 Single-Station versus Multi-Station Approach

In a single-station approach, the ionospheric coefficients and time constant parameters, namely the frequency dependent receiver and satellite biases on code observable, also known as DCBs, and the constant phase term (containing the ambiguities and other biases) are estimated using the observables from a single-station. Hence the ionospheric coefficients can only be estimated with time resolution of 10 minutes to allow sufficient robustness of solution. Due to limited number of observations used in a single-station approach for estimation of the ionospheric coefficients and, receiver and satellite specific biases, the ionosphere gradients show artificially high levels of variation as a satellite sets and rises.

For multi-station ionosphere modelling, the GNSS model can be designed such that all the parameters (ionosphere and other time-constant) are estimated in a multi-station mode. This approach adds constraints to the time-constant satellite specific parameters, namely, the GPS satellite DCBs. However, the multi-station approach requires algorithms to account for different number of satellites, rising and setting, for different receivers at any given time. Another feasible approach is to consider only satellites that are visible to all receivers at any given time, however this can result in loss of information. Hence in this work, the $STEC$ is retrieved for each GNSS receiver and further ionospheric modelling is performed using a multi-station approach.

The multi-station approach by retrieved $STEC$ as observables allows for the estimation of ionospheric coefficients at a higher temporal resolution. Collective data from all the stations are used to estimate ionospheric coefficients, which is explained in detail in Section 4.2.4. We estimate a single set of ionospheric coefficients at every 2 minutes using multi-station approach. The redundancy of a full-rank model is given by the number of observations minus the number of unknowns. The multi-station ionospheric model, which uses the retrieved $STEC$, has higher redundancy as compared to the single-station model.

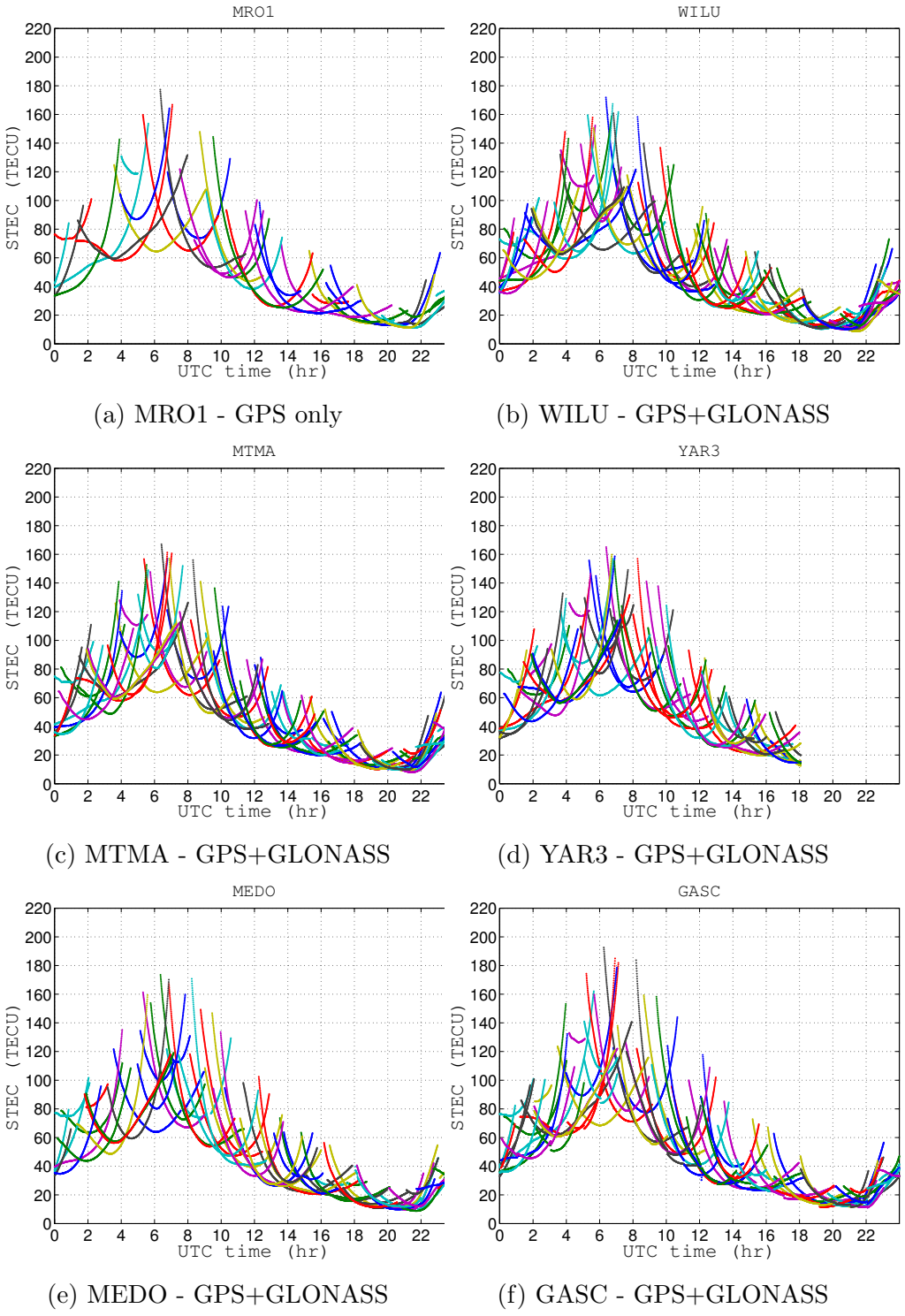

(a) MRO1 - GPS only

(b) WILU - GPS+GLONASS

(c) MTMA - GPS+GLONASS

(d) YAR3 - GPS+GLONASS

(e) MEDO - GPS+GLONASS

(f) GASC - GPS+GLONASS

Figure 4.1: Retrieved STEC for the selected GA GNSS stations on DOY 062, year 2014, each colour represents one complete satellite arc/pass.

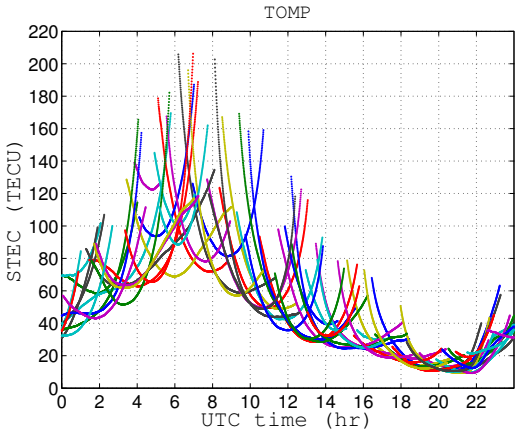

(g) TOMP - GPS+GLONASS

Figure 4.1: Retrieved STEC for the selected GA GNSS stations on DOY 062, year 2014, each colour represents one complete satellite arc/pass.

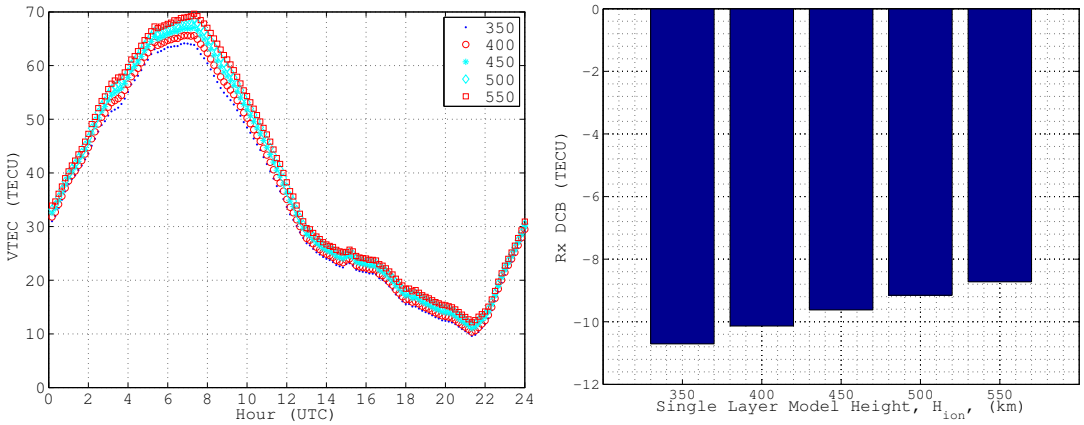

(a) VTEC as a function of H_{ion} (b) Receiver DCB as a function of H_{ion}

Figure 4.2: Effect on estimated VTEC and receiver DCBs by the choice of H_{ion}, H_{ion} is varied between 350 to 550 km in steps of 50 km.

4.2.3 Effective Height of the Ionosphere Layer

While modelling the ionosphere using a single layer model assumption, in Chapter 3, the ionosphere electron density is assumed to be integrated at a fixed height of 450 km. The single layer height, referred to as H_{ion}, is used to compute the obliquity factor (mapping function) and the coordinates at the IPP.

To understand the effect of H_{ion} on estimated ionospheric coefficients and receiver DCBs, H_{ion} was varied between 350 and 550 kms in steps of 50 km. Only the GPS observables for GA station MRO1 for DOY 062, year 2014, were used for this analysis (i.e. using a single-station model approach). Figure 4.2(a) shows the estimated values of $VTEC$ (Vertical TEC) for different chosen values of H_{ion}. The differences in $VTEC$ lie between ~ 0.5 to ~ 1 TECU while H_{ion} is varied by 50 km at different times during the day. However, the differences in receiver DCBs are affected by an amount corresponding to the constant difference in $VTEC$ over 24 hours (minimum difference in $VTEC$ over 24 hours). The difference in the estimated receiver DCBs, for a change of 50 km in H_{ion}, are hence found to reach a maximum value of ~ 0.5 TECU (Figure 4.2(b)). Hence, selection of the value of H_{ion} plays a significant role in ionosphere modelling and has an effect on the estimated receiver DCBs.

The single layer model height can also be evaluated from the electron density profiles, and is refereed to as effective height. The effective height of the ionospheric layer is the height at which the electron density reaches its median value, and is a function of location and time. The effective height of the single layer ionosphere model, H_{eff}, is found to be different from the height of the F2 ionosphere layer ($hmF2$). Ionospheric profiles generated using IRI-Plas (extension of IRI to plasma-sphere) model show that $H_{eff} > hmF2$, refer Figure 4.3. A discussion on H_{eff} and $hmF2$ can be found in Komjathy & Langley (1996); the empirical analysis shows that they behave linearly at any given time of the day. Since the electron density varies spatially and temporally, the $hmF2$ as well as H_{eff} both vary in time and space. During the day, $hmF2$ and H_{eff} are seen to have a constant offset. However, during the night time, while the electron density in the F2 region decreases, the effective height increases significantly due to the plasmaspheric electron density. Considering the importance of the effective height in ionospheric modelling and its variation, it is useful to have a-priori knowledge of this parameter.

Ionosphere profile data can be obtained from empirical models such as the

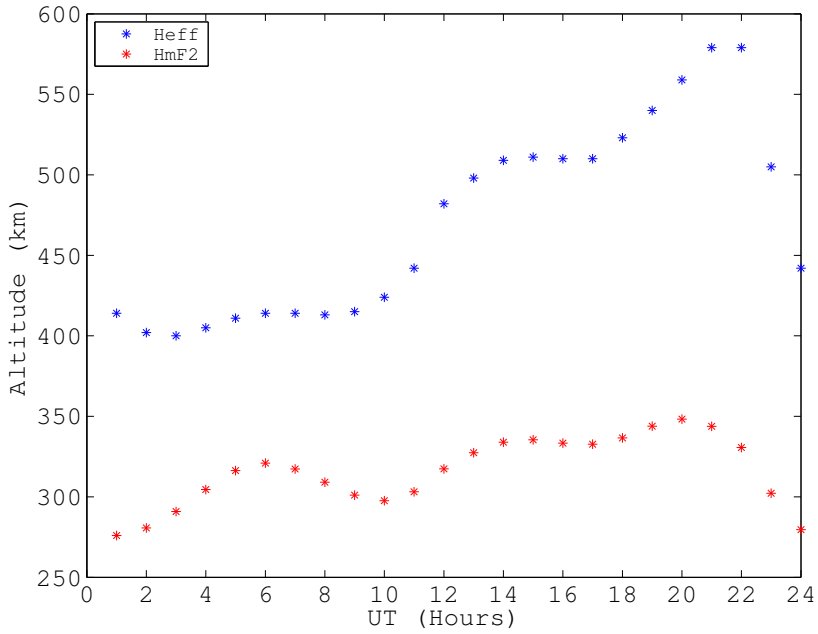

Figure 4.3: Temporal variation of $hmF2$ and H_{eff} obtained from IRI-Plas ionosphere profiles at the Taylor series expansion point.

International Reference Ionosphere (IRI) (Bilitza et al., 2014). However, the height for the ionosphere profiles from IRI are limited to 2000 km. Ionosphere-Plasmaspheric models like the Parameterised Ionosphere Model (PIM) (Daniell et al., 1995) and extension of IRI to plasma-sphere (IRI-Plas) (Gulyaeva & Bilitza, 2012; Gulyaeva et al., 2013) are able to probe the ionosphere up to plasmaspheric altitudes (above 20,000 km). Apart from the ionosphere profiles, global maps of $hmF2$ generated by IRI-Plas software (refer Figure 4.4) are available for download[1]. The temporal and spatial resolution of $hmF2$ global maps is 1 hour and $5^\circ/2.5^\circ$ in longitude and latitude, respectively.

It has already been seen that by varying the value of height for ionosphere modelling, the estimated parameters, namely, VTEC and receiver DCBs are affected. The ionosphere gradients, however, do not seem to be significantly affected when the height is varied by a constant value (H_{ion}), refer Figure 4.5. The EW gradient is not seen to have any affect by changing H_{ion}, refer Figure 4.5. Since the computation of latitude of the IPP is based on the height of the single layer, the NS gradient is seen to have slight difference for different considerations of H_{ion}, refer Figure 4.5. It is however important to incorporate the spatial variation of H_{eff} to observe any significant change in both components of the gradients.

[1]ftp://ftp.izmiran.rssi.ru/pub/izmiran/SPIM/Maps/hmF2/

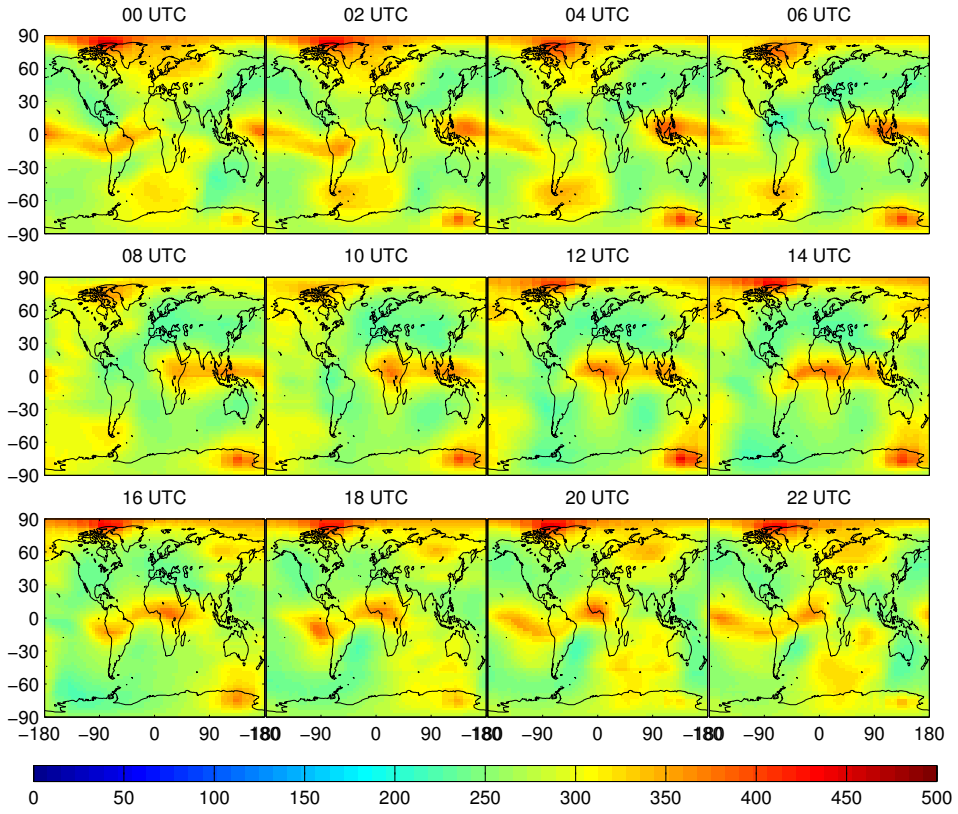

Figure 4.4: HmF2 global map from IRI-Plas model for DOY 062, 2014.

Figure 4.3 shows the temporal variation of $hmF2$ and H_{eff} at the selected Taylor series expansion point (for Taylor series expansion point, refer section 4.2.4). The difference, H_{eff} - $hmF2$, are computed using ionosphere profiles from IRI-Plas model at the expansion point. Further, H_{eff} for any satellite IPP is computed by using the $hmF2$ value from global map (Figure 4.4) and adding the difference (H_{eff} - $hmF2$) to it.

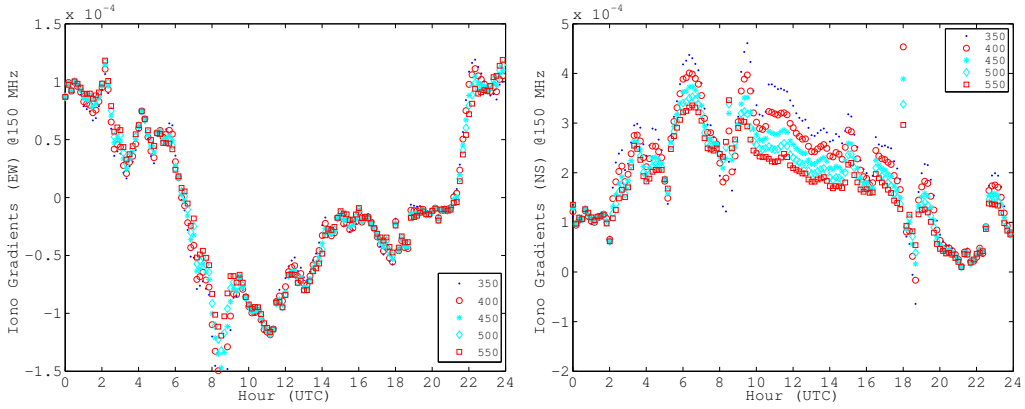

(a) EW gradient v/s HION (b) NS gradient v/s HION

Figure 4.5: Effect on estimated ionosphere gradients by the choice of H_{ion}, H_{ion} is varied between 350 to 550 km in steps of 50 km.

4.2.4 GNSS Multi-Station Modelling Using Retrieved STEC

The GA network stations in the vicinity of MRO, namely, MRO1, WILU, MTMA, YAR3, MEDO, GASC and TOMP, were selected for multi-station ionospheric modelling. Figure 4.6 presents the location of the selected GNSS stations. The details of each GNSS station are given in Table 4.1.

The retrieved $STEC$ for all the GPS and GLONASS satellites are used for regional ionospheric modelling. For a single layer model assumption, $STEC$ can be related to the $VTEC$ using a simple mapping function at a fixed height, refer Figure 4.7. The obliquity factor or the mapping function, F^s, is discussed in detail in Chapter 3, equations (3.2), the geometry of the obliquity factor is illustrated in Chapter 3, Figure 3.1. We present the Figure 4.7 again here for ease of reference. We also briefly summarise the mapping function equation as follows

Table 4.1: Description of the selected GA GPS/GNSS stations and the MWA. Data were available for all the four observing sessions, DOY 062, 063, 065, and 075, year 2014. The acronyms given under GNSS, G and GR stand for GPS only and GPS+GLONASS, respectively.

Station	Receiver type	Antenna type	GNSS	Observables used	Location (degrees)
MRO1	TRIMBLE NETR9	TRM59800.00	G	$L1$, $L2$, $C1$, $P2$	26.70° S 116.37° E
MTMA	LEICA GRX1200+GNSS	LEIAR25.R3	GR	$L1$, $L2$, $C1$, $P2$	28.11° S 117.84° E
YAR3[a]	LEICA GRX1200GGPRO	LEIAR25	GR	$L1$, $L2$, $C1$, $P2$	29.04° S 115.34° E
WILU	LEICA GRX1200+GNSS	LEIAR25.R3	GR	$L1$, $L2$, $C1$, $P2$	26.62° S 120.21° E
MEDO	LEICA GRX1200+GNSS	LEIAR25.R3	GR	$L1$, $L2$, $C1$, $P2$	26.76° S 114.61° E
GASC	LEICA GRX1200+GNSS	LEIAR25.R3	GR	$L1$, $L2$, $C1$, $P2$	24.63° S 115.34° E
TOMP	LEICA GRX1200+GNSS	LEIAR25.R3	GR	$L1$, $L2$, $C1$, $P2$	22.85° S 117.40° E
MWA	-	-	-	-	26.70° S 116.67° E

[a] Partial data available, from 00:00:00 UTC to 18:07:00 UTC on DOY 062, year 2014

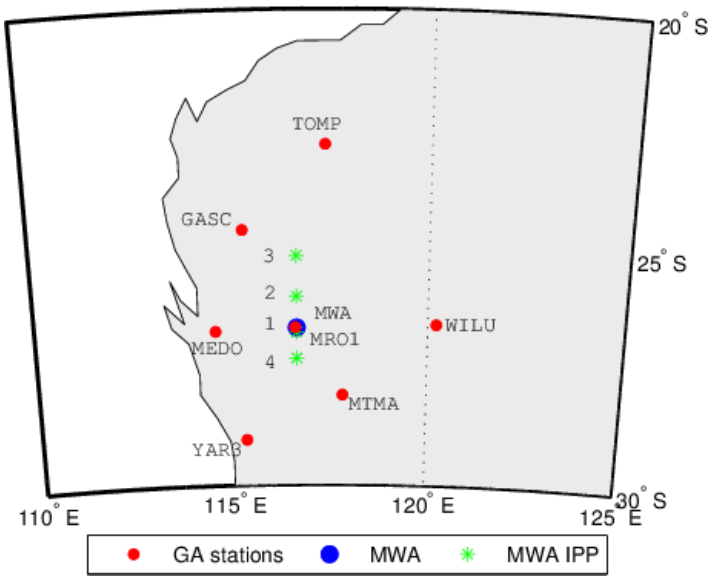

Figure 4.6: Selected GNSS station locations from Geoscience Australia's network (red), MWA location (blue) and MWA IPP (green) for the four MWA observation nights (DOY 062, 063, 065 and 075 marked by 1 to 4, respectively)

$$
\begin{aligned}
STEC &= VTEC \cdot F^s \\
F^s &= \frac{1}{\cos(z')} = \frac{1}{\sqrt{1-\sin^2 z'}} \\
\sin z' &= \frac{R_e}{R_e + H_{ion}} \sin(z)
\end{aligned}
$$

where z' is the zenith angle at the IPP, R_e is the mean radius of the Earth, considered to be 6371 km and assuming a spherical Earth, H_{ion} is the height at the sub-ionospheric point, and z is the zenith angle of the satellite as seen by the receiver.

Two approaches are considered for the height of the single layer model; firstly, the height is assumed to be fixed at 450 km, as before (will be referred to as H_{ion}), and secondly, the spatial and temporal variations are incorporated in the height from IRI-Plas model (will be referred to as H_{eff}).

The $VTEC$ is further modelled using a Taylor series polynomial expansion, the expansion point being the MWA IPP, as discussed in Chapter 3, equation (3.5). We summarise the second order polynomial function to model the $VTEC$

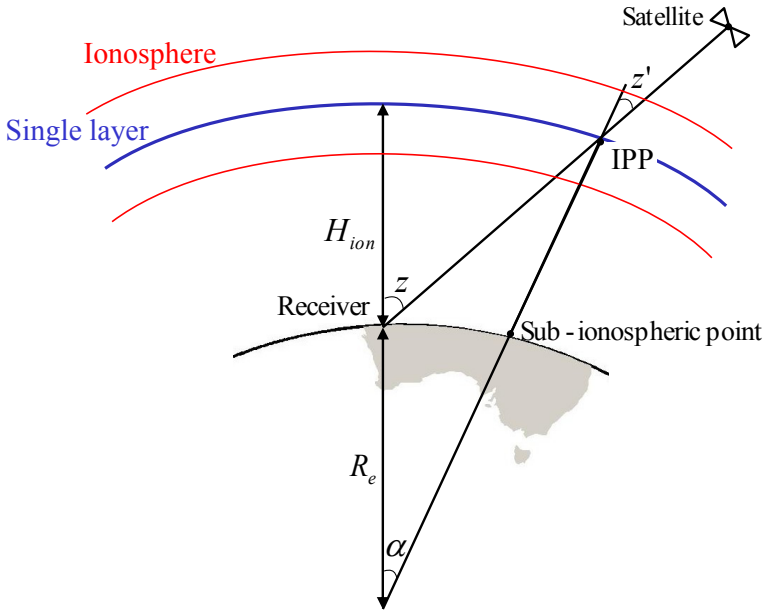

Figure 4.7: Ionosphere single layer model representation, earlier presented in Chapter 3 as Figure 3.1.

as follows

$$\begin{aligned} VTEC(\varphi_g, s) &= VTEC_0 + (\varphi_g - \varphi_{g_0})f'\varphi + (s - s_0)f's + \\ &+(\varphi_g - \varphi_{g_0})^2 f''\varphi_g\varphi_g + (s - s_0)^2 f''ss \\ &+(\varphi_g - \varphi_{g_0})(s - s_0)f''\varphi_g s. \end{aligned}$$

The Sun fixed longitude, s, is related to the local solar time (LT) as $s = \lambda_g + LT - \pi$, where λ_g is the geomagnetic longitude at IPP, LT is in radians, $VTEC_0$ is the $VTEC$ at the central location in the network and $f's$, $f'\varphi_g$, $f''ss$, $f''\varphi_m\varphi_g$, $f''\varphi_g s$ are the first and second order derivatives of $VTEC$ along the Sun fixed longitude and latitude, respectively.

Figure 4.8 presents a snapshot of the satellite IPPs for all the GA GNSS stations and MWA IPP locations.

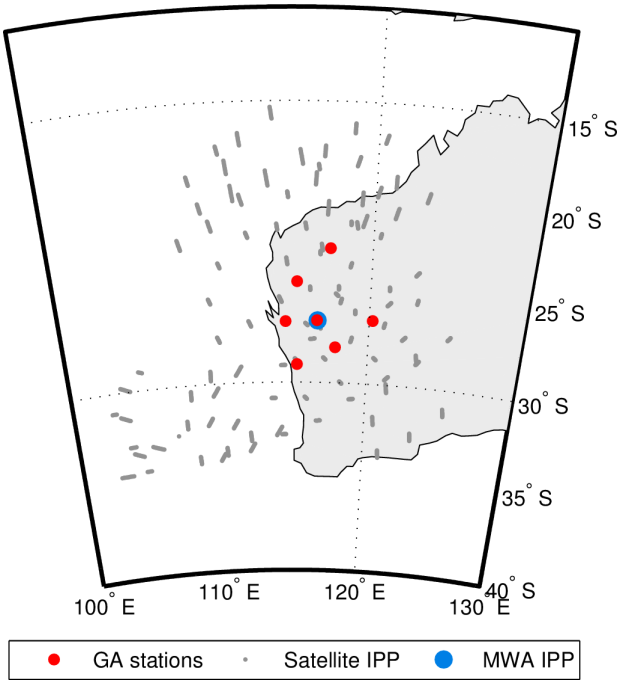

Figure 4.8: A snapshot of MWA IPP (blue), GA GNSS stations (red), and satellite IPPs for 1 hour during MWA observations (gray) in Earth-fixed reference frame, on DOY 062, 2014. The MWA IPP is considered for the Taylor series expansion point.

4.3 MWA Ionosphere

In order to validate our modelled ionosphere against radio astronomy data, precisely the same data were used as in our previous work. Please see Wayth et al. (2015) for a full description of the GLEAM survey and Chapter 3, Section 3.4 for a detailed description of how these MWA data may be compared with GPS data.

As before, the data consist of a time-series of ionosphere gradients, in both north-south and east-west directions, averaged over all sources within the MWA field of view. The centre of this field of view is taken to be the MWA pierce point.

4.4 Results and Discussion

4.4.1 Comparisons of Ionosphere Gradients - Single-Station v/s Multi-Station Approach

The gradients obtained from MWA observations in Right Ascension (East-West or EW direction) and Declination (North-South or NS direction), were computed from the ionosphere first and second order coefficients given in equation (3.5), and are plotted (in green) along GNSS observed gradients. The ionospheric gradients, in EW and NS directions, were estimated for 03-03-2014 (DOY 062), 04-03-2014 (DOY 063), 06-03-2014 (DOY 065), and 16-03-2014 (DOY 075) using both single-station (Arora et al., 2015) and multi-station approaches (refer to Figures 4.9 and 4.10). The EW gradients are presented in Figure 4.9 using a single-station approach, for DOY 062, 063, 065 and 075 (refer to 4.9(a), 4.9(c), 4.9(e) and 4.9(g), respectively). The EW gradients using the multi-station approach are presented in Figures 4.9(b), 4.9(d), 4.9(f) and 4.9(h) for DOY 062, 063, 065 and 075, respectively. Similarly the NS gradients using single-station and multi-station approach are presented in Figures 4.10(a), 4.10(c), 4.10(e), 4.10(g) and 4.10(b), 4.10(d), 4.10(f), 4.10(h) for DOY 062, 063, 065 and 075, respectively. In each of the Figures 4.9 and 4.10, two different ionosphere gradients are estimated, firstly while considering the height of the ionospheric layer, H_{ion}, at 450 km, plotted as blue line. Secondly, the height is assumed to vary in time and space, obtained from IRI-Plas model (H_{eff}), it is indicated by red curve in the plots.

Table 4.2 presents the EW (r_{EW}) and NS (r_{NS}) gradient correlation between the GNSS and MWA observed gradients for the single-station and multi-station approach for all the days of observations.

The correlation between the GPS and MWA EW gradients were seen to be identical within the errors between the single-station and multi-station approaches for two days, refer Table 4.2. For the remaining two days the EW gradient correlation was found to be significantly better using the multi-station approach. The NS gradient correlation was found to be significantly better for three of the four days using the multi-station approach. The general trend showed that the EW and NS gradients show better correlations with the MWA observed gradients when estimated using a multi-station approach rather than single-station approach.

The single-station approach is limited by the number of observations to constrain the gradients, hence the gradients appear to be noisy. This is less the case for the multi-station approach.

The IPP coordinates (ϕ, λ, h) were computed using a fixed height assumption (H_{ion}) and a variable effective height from the model IRI-Plas (H_{eff}), and the difference in the height component (h) is presented. Figures 4.11 (a) and 4.11 (b) show the difference in the height component (h) of the IPPs, computed using fixed (H_{ion}) and variable height (H_{eff}), w.r.t the center MWA, at 12 noon and 12 midnight LT, respectively. Since the fixed height does not provide any variation to the height component of the IPP coordinates, the variation seen in Figures 4.11 (a) and 4.11 (b) is due to the effective height (H_{eff}). It can be noted that, by using the IRI-Plas model values for ionospheric layer height, (H_{eff}), a curvature is defined for the ionospheric layer. Hence the gradients appear to have a steeper slope while H_{eff} is used (Figures 4.9 and 4.10), as compared to fixed ionospheric shell height (H_{ion}).

4.5 Summary

In this work, we have explored several incremental improvements on our previous work presented in Chapter 3 (Arora et al., 2015), including: 1) the addition of GLONASS data to augment GPS data; 2) the development of a multi-station ionospheric solution rather than a single-station solution; and 3) the sensitivity of our analysis to varying height for a single layer ionospheric model. This work is designed to explore the most effective future directions for the development of ionospheric modelling to support calibration of the MWA.

The height of the single layer model is seen to play a significant role in the

Table 4.2: Correlation between the GNSS and MWA observed gradients in EW (r_{EW}) and NS (r_{NS}) components, its standard error (σ_r) using single-station approach and multi-station approach.

DOY	r_{EW} ($\sigma_{r_{EW}}$)			
	Single-station approach		Multi-station approach	
	H_{ion}	H_{eff}	H_{ion}	H_{eff}
062	0.78(0.05)	0.76(0.06)	0.81(0.05)	0.83(0.04)
063	0.79(0.05)	0.77(0.05)	0.90(0.03)	0.89(0.03)
065	0.75(0.06)	0.65(0.08)	0.91(0.02)	0.92(0.02)
075	0.95(0.01)	0.95(0.01)	0.95(0.01)	0.94(0.02)
	r_{NS} ($\sigma_{r_{NS}}$)			
	Single-station approach		Multi-station approach	
	H_{ion}	H_{eff}	H_{ion}	H_{eff}
062	0.84(0.04)	0.85(0.04)	0.93(0.02)	0.92(0.02)
063	0.82(0.05)	0.81(0.05)	0.87(0.03)	0.87(0.03)
065	0.87(0.03)	0.89(0.03)	0.98(0.01)	0.98(0.01)
075	0.67(0.07)	0.72(0.07)	0.87(0.03)	0.87(0.03)

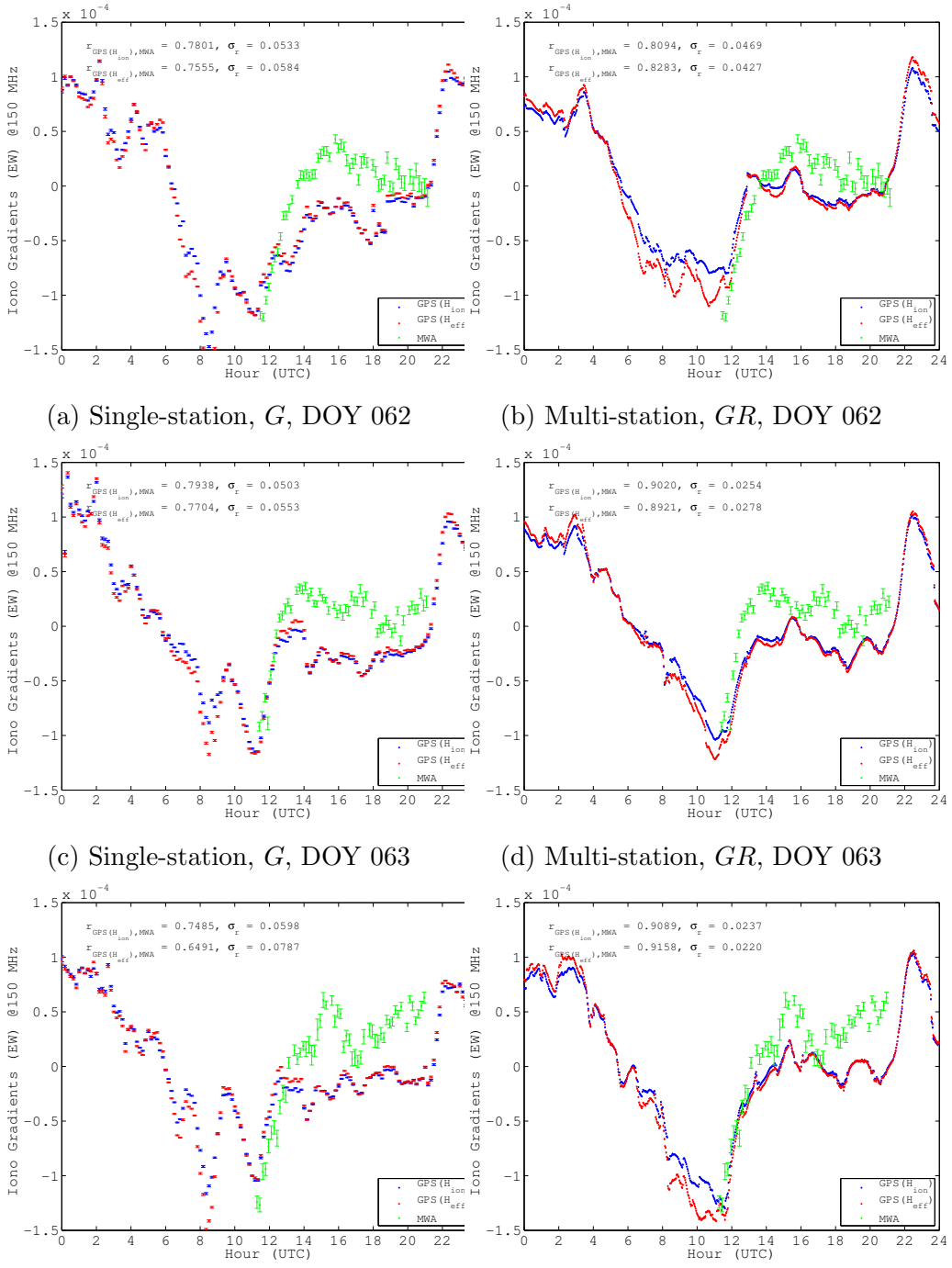

(a) Single-station, G, DOY 062 (b) Multi-station, GR, DOY 062

(c) Single-station, G, DOY 063 (d) Multi-station, GR, DOY 063

(e) Single-station, G, DOY 065 (f) Multi-station, GR, DOY 065

Figure 4.9: EW ionosphere gradients observed from GNSS data [blue(H_{ion}) and red(H_{eff})] and the MWA (green) using single-station approach, GPS only (G, left column) and multi-station approach, GPS+GLONASS (GR, right column) on DOY 062, 063, 065 and 075, year 2014.

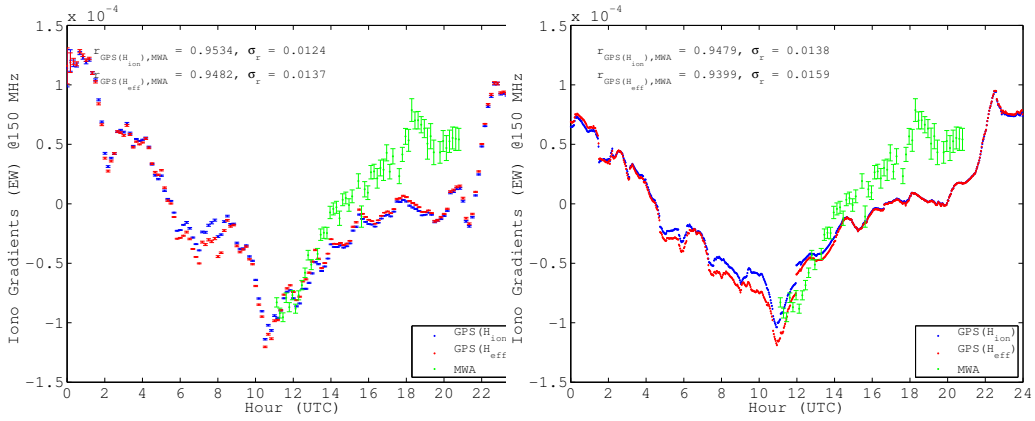

(g) Single-station, G, DOY 075 (h) Multi-station, GR, DOY 075

Figure 4.9: EW ionosphere gradients observed from GNSS data [blue(H_{ion}) and red(H_{eff})] and the MWA (green) using single-station approach, GPS only (G, left column) and multi-station approach, GPS+GLONASS (GR, right column) on DOY 062, 063, 065 and 075, year 2014.

estimated ionosphere coefficients. The estimated ionosphere coefficients and receiver DCBs were seen to have a common minimum offset while the height of the single layer (H_{ion}) was varied. While a variable height of the single layer was incorporated using IRI-Plas model, the gradients were seen to have a steeper slope. The increased steepness in the slope of the gradients could be due to curvature incorporated in the height of the single layer model (H_{eff}) by considering spatial and temporal variation.

For a single layer model, the height of the ionospheric layer is therefore an important parameter which influences the estimated coefficients. Also, the modelled $VTEC$ is limited by the obliquity factor used to map the $STEC$ to $VTEC$. To overcome the above limitations, it is important to model the ionosphere using a three-dimensional spatial model. We conclude that this indicates that future work should focus on the construction of a three-dimensional (or multi-layer) model for the ionosphere.

We have also found that the addition of GLONASS data to GPS data, and the use of a multi-station solution rather than a single-station solution, gives better results than our original work. Thus, any future modelling effort should continue in this direction.

The gradients estimated using the multi-station approach are estimated at a higher time resolution (2 minutes) than single-station estimates. Also, due to

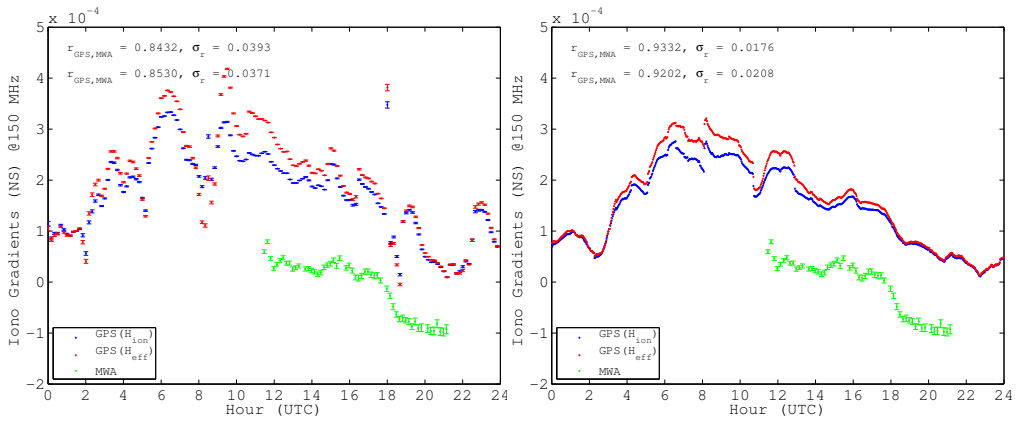

(a) Single-station, G, DOY 062

(b) Multi-station, GR, DOY 062

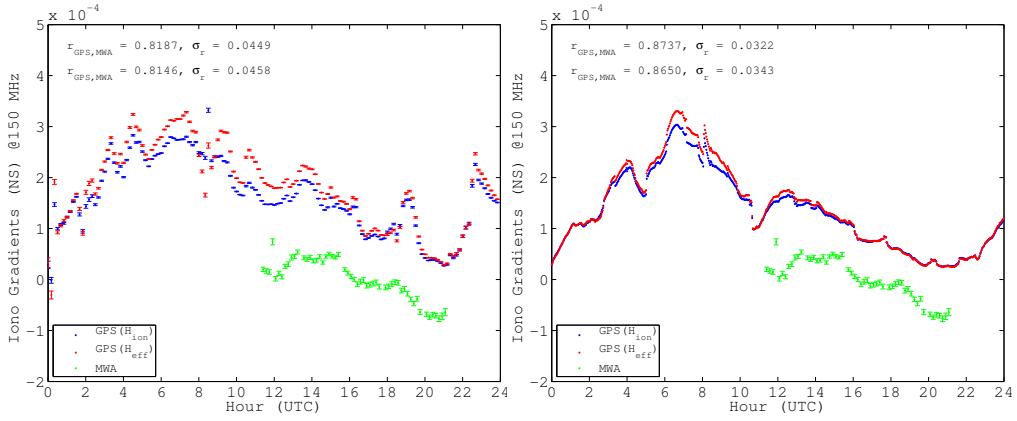

(c) Single-station, G, DOY 063

(d) Multi-station, GR, DOY 063

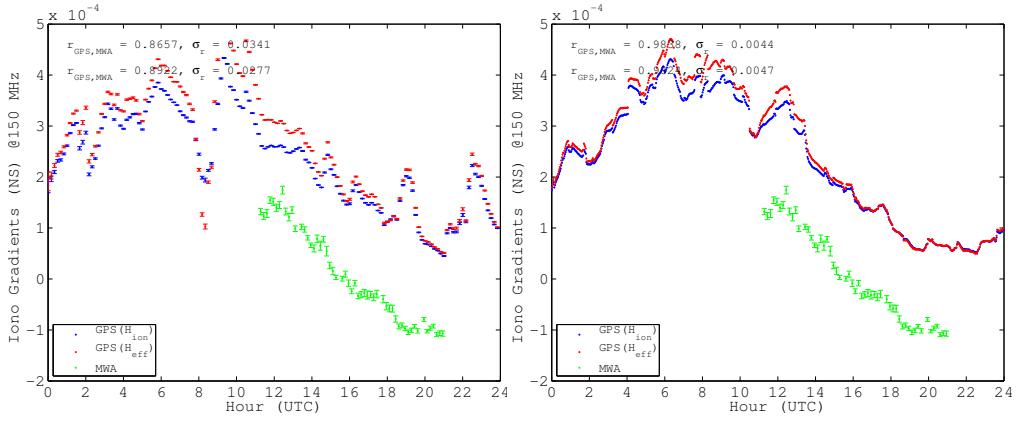

(e) Single-station, G, DOY 065

(f) Multi-station, GR, DOY 065

Figure 4.10: NS ionosphere gradients observed from GNSS data [blue(H_{ion}) and red(H_{eff})] and the MWA (green) using single-station approach, GPS only (G, left column) and multi-station approach, GPS+GLONASS (GR, right column) on DOY 062, 063, 065 and 075, year 2014.

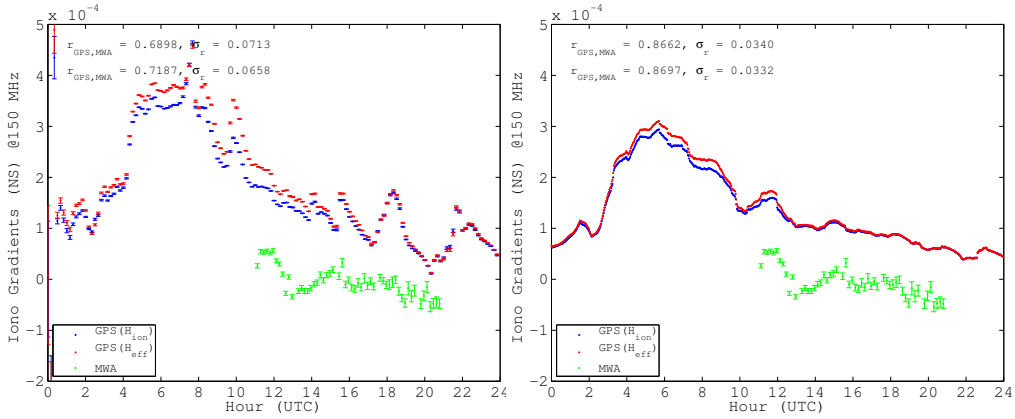

(g) Single-station, G, DOY 075 (h) Multi-station, GR, DOY 075

Figure 4.10: NS ionosphere gradients observed from GNSS data [blue(H_{ion}) and red(H_{eff})] and the MWA (green) using single-station approach, GPS only (G, left column) and multi-station approach, GPS+GLONASS (GR, right column) on DOY 062, 063, 065 and 075, year 2014.

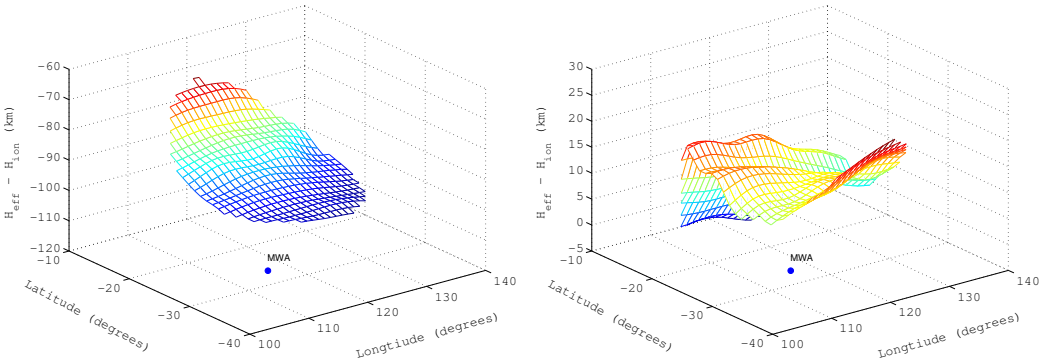

(a) H_{eff}-H_{ion}, 12 noon LT (b) H_{eff}-H_{ion}, 12 midnight LT

Figure 4.11: Difference in the height component of the IPP coordinates (centred at MWA), computed using a fixed height (H_{ion}=450 km), and variable height (H_{eff}, as defined in Section 4.2.3) from IRI-Plas model, at 12 noon LT (left column) and 12 midnight LT (right column)

the large number of observations used to estimate gradients in a multi-station approach, the gradients seem to have a smoother temporal variation. For all the selected days of MWA observations, the correlation between MWA and GNSS estimated gradients was found to be identical within errors or higher with multi-station approach as compared to single-station approach.

The NS gradients, estimated using the multi-station approach, agreed with the MWA observed gradients. The EW gradients had a better correlation than single-station approach, however did not seem to correlate as well as the NS gradients. The current distribution of GNSS receiving stations, while demonstrated to be successful in characterising large-scale ionospheric features and validating our technical approach, is inadequate for advanced modelling.

5 Conclusions

5.1 Thesis Summary

In this thesis, we aim to generate ionospheric corrections using the data from the Global Positioning System (GPS) and GLONASS (Russian global positioning system) from the existing Geoscience Australia GNSS (Global Navigation Satellite System) network near Murchison Radio-astronomy Observatory (MRO). The work presented in thesis explores the possibilities to model the ionosphere using the current available GNSS infrastructure, highlights the problems that limit the current approach, and proposes a solution in view of generating usable ionospheric corrections for calibration of the future low frequency interferometers. The results of this thesis are briefly summarised as follows.

5.1.1 Ionospheric Modelling Using GPS and GLONASS

The refractive bending due to the ionosphere causes an error in the source positions. Due to the dispersive nature of the ionosphere and the inverse relation of change in phase to the observing frequency, makes the effect greater at lower frequencies. With the current developments in the low frequency radio astronomy, the need to characterise the ionosphere in order to calibrate the future low frequency radio interferometers has rightfully gained the attention. In this research work, we aim to generate the ionospheric corrections using GNSS data, and improve upon the methodology by comparing them with the ionospheric effects derived from the MWA. The ionospheric effects on the interferometers, which cause displacement in the position of the sources were studied. The ionospheric corrections were generated by modelling the ionosphere using a single

layer approximation, by utilising the local GNSS data around MRO.

In Chapter 3, the ionospheric corrections were generated using a single-station approach. The ionosphere was modelled using a second order Taylor series polynomial expansion, while the ionosphere was assumed to be concentrated at a fixed height. The ionospheric trends obtained from GPS observations and the MWA were compared. The ionospheric trends obtained from GPS and the MWA showed good comparisons, and motivated further exploration.

Since the single-station approach made use of a limited number of observations for ionospheric modelling, the original approach to model the ionosphere was improved by increasing the number of observations and presented in Chapter 4. GPS observations were incorporated from multiple stations simultaneously for ionospheric modelling. Further, to increase the density of the IPPs, GLONASS observations were included for modelling the ionosphere. The single layer model height was now varied spatially and temporally, in contrast to the earlier fixed height approach, using the electron density profiles from the IRI-Plas model. A variable height model for the ionosphere single layer was used to include the spatial variations in height. The estimated ionospheric corrections using GPS and GLONASS showed a significant improvement, and the comparisons with the MWA derived ionospheric effects was seen to have an overall better correlation.

The spatial variations in the height were seen to be significant for modelling the ionosphere, the ionosphere gradients exhibited better replicating trends seen in the MWA data with the variable height model. The results obtained with the variable height model are encouraging, the future work would incorporate the variation of electron density with height for ionospheric modelling, by making use of models like the 3D ionospheric tomography.

5.2 Scope for Future Work

5.2.1 The Future Low Frequency Radio Astronomy

The MWA with its wide FoV imaging capability, sees a position offset due to the ionosphere for each of the sources in its FoV. This capability of the MWA has been exploited to detect small-scale structures in the ionosphere, the spatial scales of the ionosphere structures were found to be ∼10-100 km Loi et al. (2015c,d,b). Even though the ionospheric effects can currently be derived from the MWA, however, the future upgrades to the MWA and the upcoming interferometer the

SKA-low would pose a challenge to derive such ionospheric corrections. The MWA, 128 tile configuration, has maximum baseline lengths of ∼3km, has the ionosphere correlated for both the interferometer antenna elements. With the wide Field of View (FoV) capability of MWA, the direction-dependent effects are significant, that is, the ionospheric is different for different sources within the FoV. The degrees of freedom for a mathematical model, which is the number of observations minus the number of unknowns, are higher with the current MWA, 128 tile, hence ionosphere effects can be derive from the observations. With the upgrades to the MWA, the MWA, 256 tile, would have the maximum baseline length of ∼6 km, and hence higher angular resolution. While the sources are being resolved better, the higher order effects in the ionosphere would become increasingly dominant within the FoV. The future SKA-low, with extremely large baseline lengths and wide FoV imaging capability, would have the direction-dependent ionospheric effects, as well the ionosphere would be no longer correlated across the interferometer elements. In such a scenario, the degrees of freedom would reduce massively, and deriving ionospheric effects from the observations may not be possible much of the time. Hence an independent source of ionospheric corrections are required to support and complement the current information of the ionosphere that is derived from the MWA.

5.2.2 Future Prospects for GNSS

The GPS satellites are capable of providing ionospheric information, however the density of the pierce points is far too low to probe these small scales for the data sets currently available for the MRO. For the current installed GPS receiver near the MRO, only 8-10 satellites are visible above horizon at any given time. The number of measurements can be increased to 15-20 satellites by including data from GLONASS satellites. Future Global Navigation Satellite Systems (GNSS), namely, BeiDou (China) and Galileo (European Union) are expected to be operational around the year 2020 (UN, 2010). Regional satellite systems such as the Quasi-Zenith Satellite System (QZSS, Japan) (UN, 2010), currently under development, will have 4 satellites, all of which pass over the MRO. In this scenario 30-40 satellites would be above the horizon at the MRO at any given time, with an average separation of 200 km on the ionosphere. In addition to getting information directly from GPS/GNSS satellites, additionally by using the data from the low Earth orbiting satellites (LEO), 3 dimensional ionospheric structure can be generated. The LEO's satellites have a GNSS receiver onboard, after re-

ceiving they transmit the GNSS data from low Earth orbits,. This information can be used to generate a 3 dimensional structure of the ionosphere using Abel transformation (Jin et al., 2014).

5.2.3 Proposed GNSS Station Installations

The research presented in this thesis establishes a methodology to successfully generate the ionospheric effects using the observations from local GNSS stations near the MRO. However, in order to generate the ionospheric corrections at the scales of the current and future low frequency interferometers, we propose to increase the current GNSS infrastructure around MRO.

To measure the ionosphere on scales of <10 km, a dense cluster of GNSS receivers (5-10 receivers), with baselines as small as ∼5 km would need to be installed. This would allow small structures to be resolved towards each satellite. However, it is not guaranteed that a GNSS satellite would be in the MWA field of view at all times. Hence another small cluster of GNSS stations would need to be deployed strategically. Deploying the further cluster at a distance of ∼100 km would fill in the gaps between existing satellites. We call this approach the "cluster of clusters" approach. For further densification, a cluster of GNSS stations at the median of existing clusters (∼50 km) could be deployed.

The sparse population around the MRO and the lack of remote power and communication infrastructure constrains the possible locations for such a cluster. Locations indicated in Figure 5.1 are plausible cluster locations given that they are existing communities and homesteads likely to have the necessary infrastructure.

Future work will evaluate the expansion of GNSS stations around MRO, in view of generating a three-dimensional ionospheric model, to meet the ionosphere calibration requirements for the MWA.

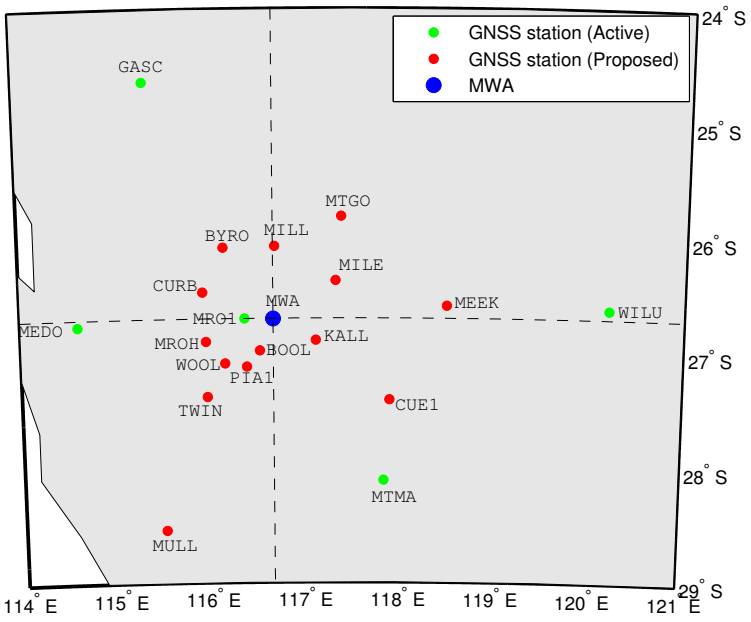

Figure 5.1: Current (green) and proposed (red) GNSS station locations in vicinity of MRO. The MWA location is marked in blue.

Bibliography

Appleton, E. V. 1932, Wireless Section, Institution of Electrical Engineers-Proceedings of the, 7, 257

Arikan, F., Nayir, H., Sezen, U., & Arikan, O. 2008, Radio Science, 43, RS4004

Arora, B. S., Morgan, J., Ord, S. M., Tingay, S. J., Bell, M., Callingham, J. R., Dwarakanath, K. S., For, B.-Q., Hancock, P., Hindson, L., et al. 2016, PASA - Publications of the Astronomical Society of Australia, 33

Arora, B. S., Morgan, J., Ord, S. M., Tingay, S. J., Hurley-Walker, N., Bell, M., Bernardi, G., Bhat, N. D. R., Briggs, F., Callingham, J. R., et al. 2015, PASA - Publications of the Astronomical Society of Australia, 32

Bassiri, S. & Hajj, G. 1992, Telecommunications and Data Acquisition (TDA) Progress Report, 42

Beach, T. L. 1998, Doctors of Philosphy Thesis, Cornell University, Ithaca, New York

Beutler, G., Rothacher, M., Schaer, S., Springer, T., Kouba, J., & Neilan, R. 1999, Advances in Space Research, 23, 631

Bilitza, D., Altadill, D., Zhang, Y., Mertens, C., Truhlik, V., Richards, P., McKinnell, L.-A., & Reinisch, B. 2014, Journal of Space Weather and Space Climate, 4, A07

Bolton, J. 1948, Nature, 162, 141

Chevalier, J. M., Bergeot, N., Bruyninx, C., Legrand, J., Baire, Q., Defrainge, P., & Aerts, W. 2013, in The International Beacon Satellite Symposium BSS2013, Bath, 2013

Coster, A. J., Gaposchkin, E. M., & Thornton, L. E. 1992, Journal of the Institute of Navigation, 39, 191

Coster, A. J., Pratt, M. M., Burke, B. P., & Misra, P. N. 1999, in Ionospheric Effects Symposium, Alexandria, VA, 476–483

Cotton, W. 2005, in From Clark Lake to the Long Wavelength Array: Bill Erickson's Radio Science, Vol. 345, 337

Cotton, W., Condon, J., Perley, R., Kassim, N., Lazio, J., Cohen, A., Lane, W., & Erickson, W. 2004, in Astronomical Telescopes and Instrumentation, International Society for Optics and Photonics, 180–189

Dach, R. and others. 2007, Astronomical Institute, University of Bern, 640, 612

Daniell, R. E., Brown, L., Anderson, D., Fox, M., Doherty, P. H., Decker, D., Sojka, J. J., & Schunk, R. W. 1995, Radio Science, 30, 1499

Davies, K. 1990, Ionospheric Radio, Electromagnetic Waves (Institution of Engineering and Technology)

Dymond, K., Watts, C., Coker, C., Budzien, S., Bernhardt, P., Kassim, N., Lazio, T., Weiler, K., Crane, P., Ray, P., et al. 2011, Radio Science, 46

Eckersley, T. 1938, Nature, 141, 369

El-Rabbany, A. 2006, Introduction to GPS: the global positioning system, 2nd edn. (Artech house)

Ellingson, S. W., Clarke, T. E., Cohen, A., Craig, J., Kassim, N. E., Pihlström, Y., Rickard, L. J., & Taylor, G. B. 2009, Proceedings of the IEEE, 97, 1421

Erickson, W. 1999, in Synthesis Imaging in Radio Astronomy II, Vol. 180, 601

Erickson, W., Perley, R., Flatters, C., & Kassim, N. 2001, Ionospheric corrections for VLA observations using Local GPS data, Tech. rep., DTIC Document

Ewen, H. I. & Purcell, E. 1951, Nature, 168, 356

Fisher, R. A. 1936, Statistical methods for research workers No. 5 (Oliver and Boyd Edinburgh)

Francis, S. H. 1975, Journal of Atmospheric and terrestrial Physics, 37, 1011

FRP. 2001, U.S. Federal Radionavigation Plan

Gaposchkin, E. & Coster, A. 1992, in International Beacon Satellite Symposium July 6-10, 1992, Cambridge, MA USA, 138–143

Grewal, M. S. & Andrews, A. P. 2011, Kalman filtering: theory and practice using MATLAB (John Wiley & Sons)

Gulyaeva, T., Arikan, F., Hernandez-Pajares, M., & Stanislawska, I. 2013, Journal of Atmospheric and Solar-Terrestrial Physics, 102, 329

Gulyaeva, T. & Bilitza, D. 2012, New Developments in the Standard Model, 1

Gurtner, W. 1994, GPS World, 5, 48, format specifications available at ftp://igscb.jpl.nasa.gov/pub/data/format/rinex2.txt

Hall, P. 2005, in The Square Kilometre Array: An Engineering Perspective (Springer Netherlands), 5–16

Hartree, D. 1931, in Mathematical Proceedings of the Cambridge Philosophical Society, Vol. 27, Cambridge Univ Press, 143–162

Hatanaka, Y. 2008, Bulletin of the Geographical Survey Institute, 55

Herne, D., Kennewell, J., Lynch, M., & Carrano, C. 2013, in 13th Australian Space Science Conference, Sydney, NSW, Australia, National Space Society of Australia Ltd, ed. A. S. S. Conference, 129–139

Hey, J. & Stewart, G. 1946, Nature, 158, 481

Hobiger, T., Kondo, T., & Schuh, H. 2006, Radio Science, 41, n/a, rS1006

Hofmann, B., Lichtenegger, H., & Wasle, E. 2008, GNSS–Global Navigation Satellite Systems (Springer-Verlag)

Hofmann-Wellenhof, B., Lichtenegger, H., & Collins, J. 1993, Global Positioning System. Theory and practice., by Hofmann-Wellenhof, B.; Lichtenegger, H.; Collins, J.. Springer, Wien (Austria), 1993, 347 p., ISBN 3-211-82477-4, Price DM 79.00. ISBN 0-387-82477-4 (USA)., 1

Hong, C.-K., Grejner-Brzezinska, D. A., & Kwon, J. H. 2008, Earth Planets Space, 60, e25

Hurley-Walker, N., Callingham, J. R., Hancock, P. J., Franzen, T. M. O., Hindson, L., Kapińska, A. D., Morgan, J., et al. 2017, Monthly Notices of the Royal Astronomical Society, 464, 1146

Jansky, K. G. 1932, Radio Engineers, Proceedings of the Institute of, 20, 1920

—. 1933, Radio Engineers, Proceedings of the Institute of, 21, 1387

—. 1937, Radio Engineers, Proceedings of the Institute of, 25, 1517

Jin, S., Cardellach, E., & Xie, F. 2014, in GNSS Remote Sensing (Springer), 93–120

Kailath, T. 1981, Lectures on Wiener and Kalman filtering (Springer Vienna)

Kalman, R. E. 1960, Journal of Fluids Engineering, 82, 35

Kassim, N. E., Lazio, T. J. W., Erickson, W. C., Perley, R. A., Cotton, W. D., Greisen, E. W., Cohen, A. S., Hicks, B., Schmitt, H. R., & Katz, D. 2007, The Astrophysical Journal Supplement Series, 172, 686

Kennewell, J., Caruana, J., Terkildsen, M., Wu, J., Wilkinson, P., & Cole, D. 2005, The Australian Ionosphere, Tech. rep., IPS Radio and Space Services

Komjathy, A. & Langley, R. 1996, in Proceedings of the 1996 IGS Workshop International GPS Service for Geodynamics (IGS), Vol. 203

Komjathy, A., Sparks, L., Wilson, B. D., & Mannucci, A. J. 2005, Radio Science, 40, RS6006

Langley, R. 1993, GPS world, 4, 52

Leick, A. 2004, GPS satellite surveying, 3rd edn. (John Wiley & Sons)

Lichtenegger, H. & Hofmann-Wellenhof, B. 1990, in International Association of Geodesy Symposia, Vol. 102, Global Positioning System: An Overview, ed. Y. Bock & N. Leppard (Springer New York), 57–68

Loi, S. T., Cairns, I. H., Murphy, T., Erickson, P. J., Bell, M. E., Rowlinson, A., Arora, B. S., Morgan, J., Ekers, R. D., Hurley-Walker, N., & Kaplan, D. L. 2016a, Journal of Geophysical Research: Space Physics, n/a, 2015JA022052

Loi, S. T., Murphy, T., Bell, M. E., Kaplan, D. L., Lenc, E., Offringa, A. R., Hurley-Walker, N., Bernardi, G., Bowman, J., Briggs, F., et al. 2015a, Monthly Notices of the Royal Astronomical Society, 453, 2731

—. 2015b, Monthly Notices of the Royal Astronomical Society, 453, 2731

Loi, S. T., Murphy, T., Cairns, I. H., Menk, F. W., Waters, C. L., Erickson, P. J., Trott, C. M., Hurley-Walker, N., Morgan, J., Lenc, E., et al. 2015c, Geophysical Research Letters

Loi, S. T., Murphy, T., Cairns, I. H., Trott, C. M., Hurley-Walker, N., Feng, L., Hancock, P. J., & Kaplan, D. L. 2016b, Radio Science, 51, 659

Loi, S. T., Trott, C. M., Murphy, T., Cairns, I. H., Bell, M., Hurley-Walker, N., Morgan, J., Lenc, E., Offringa, A., Feng, L., et al. 2015d, Radio Science, 50, 574

Lonsdale, C. J., Cappallo, R. J., Morales, M. F., Briggs, F. H., Benkevitch, L., Bowman, J. D., Bunton, J. D., Burns, S., Corey, B. E., deSouza, L., et al. 2009, Proceedings of the IEEE, 97, 1497

Mannucci, A., Wilson, B., Yuan, D., Ho, C., Lindqwister, U., & Runge, T. 1998, Radio science, 33, 565

Melbourne, W. G. 1985, in Proceedings of the first international symposium on precise positioning with the Global Positioning System, Vol. 1519

Memarzadeh, Y. 2009, Ionospheric modeling for precise GNSS applications (TU Delft, Delft University of Technology)

Moore, R. & Morton, Y. 2011, Radio Science, 46

Parsons, A. R., Backer, D. C., Foster, G. S., Wright, M. C., Bradley, R. F., Gugliucci, N. E., Parashare, C. R., Benoit, E. E., Aguirre, J. E., Jacobs, D. C., et al. 2010, The Astronomical Journal, 139, 1468

Pawsey, J. 1946, Nature, 158, 633

Pawsey, J., McCready, L., & Gardner, F. 1951, Journal of Atmospheric and Terrestrial Physics, 1, 261

Petrie, E. J., Hernández-Pajares, M., Spalla, P., Moore, P., & King, M. A. 2011, Surveys in Geophysics, 32, 197

Remondi, B. W. 1985, Navigation, 32, 386

Richmond, A. 1978, Journal of Geophysical Research: Space Physics (1978–2012), 83, 4131

Rideout, W. & Coster, A. 2006, GPS Solutions, 10, 219

Rieger, M. & Leitinger, R. 2002, Acta Geodaetica et Geophysica Hungarica, 37, 327

Ros, E., Marcaide, J. M., Guirado, J. C., Sardón, E., & Shapiro, I. I. 2000, Astronomy and Astrophysics, 356, 357

Rothacher, M., Springer, T., Schaer, S., Beutler, G., Ineichen, D., Wild, U., Wiget, A., Boucher, C., Botton, S., & Seeger, H. 1997, in IGS 1998 Annual Report, 77–91

Sardon, E., Rius, A., & Zarraoa, N. 1994, Radio Science, 29, 577

Schaer, S. 1999, Geod.-Geophys. Arb. Schweiz, Vol. 59,, 59

Schaer, S., Beutler, G., Rothacher, M., & Springer, T. A. 1996, in Proceedings of the IGS AC Workshop, Silver Spring, MD, USA, 181–192

Schaer, S., Gurtner, W., & Feltens, J. 1998, in Proceedings of the IGS AC workshop, February 9-11, Darmstadt, Germany, Vol. 9, 11, 233–247

Seeber, G. 2003, Satellite Geodesy, 2nd completely revised and extended edition, 2nd edn. (Walter de Gruyter Berlin New York)

Sotomayor-Beltran, C., Sobey, C., Hessels, J., de Bruyn, G., Noutsos, A., Alexov, A., Anderson, J., Asgekar, A., Avruch, I., Beck, R., et al. 2013, Astronomy & astrophysics, 552, 1

Spoelstra, T. T. & Kelder, H. 1984, Radio science, 19, 779

Spoelstra, T. T. & Yi-Pei, Y. 1995, Journal of Atmospheric and Terrestrial Physics, 57, 85

Sullivan, W. 1982, in Studies in the History of Modern Science, Vol. 10, Classics in Radio Astronomy (Springer Netherlands), 302–316

Sullivan, W. T. 2005, The early years of radio astronomy: reflections fifty years after Jansky's discovery (Cambridge University Press Cambridge), 432

Sullivan, III, W. T. 1991, in Astronomical Society of the Pacific Conference Series, Vol. 19, IAU Colloq. 131: Radio Interferometry. Theory, Techniques, and Applications, ed. T. J. Cornwell & R. A. Perley, 132

Teunissen, P. 1984, Lecture notes International School of Geodesy, Erice, Italy, April

Teunissen, P. & Kleusberg, A. 1998, GPS for Geodesy, Vol. 2 (Springer Berlin)

Thompson, A., Moran, J., & Swenson, G. 2004, Interferometry and synthesis in radio astronomy, 2nd edn., ed. W.-I. New York (Wiley-VCH Verlag GmbH and Co. KGaA)

Tingay, S., Goeke, R., Hewitt, J., Morgan, E., Remillard, R., Williams, C., Bowman, J., Emrich, D., Ord, S., Booler, T., et al. 2012, arXiv preprint arXiv:1212.1327

Tingay, S. J., Goeke, R., Bowman, J. D., Emrich, D., Ord, S. M., Mitchell, D. A., Morales, M. F., Booler, T., Crosse, B., Wayth, R. B., et al. 2013, PASA - Publications of the Astronomical Society of Australia, 30, 7

UN. 2010, in Proc. of the International Committee on Global Navigation Satellite Systems Provider's Forum, United Nations, 15–40, http://www.unoosa.org/pdf/publications/icg_ebook.pdf

Vaclavovic, P. & Dousa, J. 2015, International Association of Geodesy Symposia

van de Hulst, H. 1945, Nederlands Tijdschrift voor Natuurkunde, 11, 210

van Haarlem, M., Wise, M., Gunst, A., Heald, G., McKean, J., Hessels, J., de Bruyn, A., Nijboer, R., Swinbank, J., Fallows, R., et al. 2013, Astronomy & Astrophysics [P], 556, 1

van Velthoven, P. F. J. 1990, Research supported by NWO. Eindhoven, Netherlands, Eindhoven University of Technology, 1990, 252 p., 1

Wang, C., Wang, J., & Morton, Y. 2014, in Lecture Notes in Electrical Engineering, Vol. 304, China Satellite Navigation Conference (CSNC) 2014 Proceedings: Volume II, ed. J. Sun, W. Jiao, H. Wu, & M. Lu (Springer Berlin Heidelberg), 363–373

Wayth, R., Lenc, E., Bell, M., Callingham, J., Dwarakanath, K., Franzen, T., For, B.-Q., Gaensler, B., Hancock, P., Hindson, L., et al. 2015, Publications of the Astronomical Society of Australia

Wijnholds, S., Van Der Tol, S., Nijboer, R., & van der Veen, A. 2010, Signal Processing Magazine, IEEE, 27, 30

Wübbena, G. 1985, in Proceedings of the first international symposium on precise positioning with the Global Positioning System, Positioning with GPS-1985, Vol. 19, U.S. Department of Commerce, Rockville, Md., 403–412

Yeh, K. C. & Liu, C. H. 1974, Reviews of Geophysics, 12, 193

Zolesi, B. & Cander, L. R. 2014, Ionospheric prediction and forecasting (Springer-Verlag Berlin Heidelberg)

A

Publications

Publications directly resulting from work done in this thesis:

- **B. S. Arora**, J. Morgan, S. M. Ord, S. J. Tingay, N. Hurley-Walker et. al., (2015), Ionospheric modelling using GPS to calibrate the MWA. 1: Comparison of first order ionospheric effects between GPS models and MWA observations Publications of the Astronomical Society of Australia, Volume , 32, e029 doi:10.1017/pasa.2015.29.

- **B. S. Arora**, J. Morgan, S. M. Ord, S. J. Tingay et. al., (2016), Ionospheric Modelling using GPS to Calibrate the MWA. II: Regional ionospheric modelling using GPS and GLONASS to estimate ionospheric gradients, Publications of the Astronomical Society of Australia, Volume 33, doi:10.1017/pasa.2016.22

Other publications that, while not associated with this thesis, were instrumental in providing the necessary preparations that were required for the research presented in this document:

- Loi, S. T.; Cairns, I. H.; Murphy, T.; Erickson, P. J.; Bell, Martin E.; Rowlinson, A.; **Arora, B. S.**; Morgan, J.; Ekers, R. D.; Hurley-Walker, N.; Kaplan, D. L., (2016), "Density duct formation triggered by a travelling ionospheric disturbance: MWA observations", Journal of Geophysical Research, Space Physics, 121, doi:10.1002/2015JA022052.

- Willis, A. G.; Mevius, M.; Anderson, J. M.; Sullivan, S. O.; Lenc, E.; **Arora, B. S.**; Gaensler B.; and T. L. Landecker. "Derivation of Corrections for Ionospheric Faraday Rotation Part1: Determination of Ionospheric Total

Electron Content using Public Domain GPS Data Sets", in Proceedings of CALIM-2014, Kiama, Sydney, Australia (2016, under review).

- Bernardi, G.; Greenhill, L. J.; Mitchell, D. A.; Ord, S. M.; Hazelton, B. J.; Gaensler, B. M.; de Oliveira-Costa, A.; Morales, M. F.; Udaya Shankar, N.; Subrahmanyan, R.; Wayth, R. B.; Lenc, E.; Williams, C. L.; Arcus, W.; **Arora, B. S.**; et. al., (2013), "A 189 MHz, 2400 deg2 Polarization Survey with the Murchison Widefield Array 32-element Prototype." The Astrophysical Journal 771.2 (2013): 105.

Every reasonable effort has been made to acknowledge the owners of copyright material. I would be pleased to hear from any copyright owner who has been omitted or incorrectly acknowledged.